A High-Throughput Method for *In Vitro* Generation and Studies of Oxygen Microgradients

by

Mikhail Pinelis

A dissertation submitted in partial fulfillment
of the requirements for the degree of
Doctor of Philosophy
(Electrical Engineering)
in The University of Michigan
2010

Doctoral Committee:

Professor Michel M. Maharbiz, Co-Chair
Professor Kensall D. Wise, Co-Chair
Professor Katsuo Kurabayashi
Professor Khalil Najafi

This work is dedicated to my family.

"I look to the diffusion of light and education as the resource to be relied on for ameliorating the condition, promoting the virtue, and advancing the happiness of man."

Thomas Jefferson

ACKNOWLEDGEMENTS

I would first like to thank my co-advisors Professor Michel Maharbiz and Professor Kensall D. Wise for their continual guidance, encouragement, funding and support throughout my graduate studies at The University of Michigan. I have deeply appreciated their commitment to academic excellence and enjoyed the opportunity to study a variety of MEMS and microfluidic structures and applications. I consider it a privilege to have been a part of their groups and I look forward to working with them in the future. I also wish to thank Professor Khalil Najafi and Professor Katsuo Kurabayashi for serving on my dissertation committee and for their thoughtful feedback. A special thank-you goes to Professor Euisik Yoon who generously allowed me to use his lab during the last year of my graduate work to culture cells and conduct oxygen measurement experiments. Additionally, I would like to thank all of the WIMS and EECS faculty for their success in establishing and developing the University of Michigan as one of the leading MEMS and microsystems institutions. Recognition is also due to the Lurie Nanofabrication Facility, Solid State Electronics Laboratory and department staff for their help and support. Beth Stalnaker, Karen Liska, Bonnie Grigg, Trasa Burkhardt, Laura Jarels, Deb Swartz, Robert Gordenker, Gregory Allion, Phil Collica, Dennis Grimard, Sandrine Martin, Dennis Schweiger, Ed Tang, Brian Vanderelzen and Terre Briggs deserve a particular thank-you note. I am also very grateful for the generous financial support I have received from a number of different sources. In particular, I thank the NSF IGERT and NIH CBTP

programs for excellent opportunities and funding over the years. I am also thankful to Professor Shuichi Takayama for introducing me to the field of microfluidics and lab-on-a-chip technologies during my first year of graduate studies. My colleagues and friends from the campus community have been an invaluable part of my life in Ann Arbor. I am particularly grateful to Jaehyun Park, Meng-Ping Chang, Tushar Bansal, Leonid Shamban, Patrick Ingram, Yuriy Goykhman, Ruba Borno, Hirotaka Sato, Onnop Srivannavit and Andreja Jovic. Finally and most importantly, I would like to express my deepest gratitude to my family: my parents, Iosif and Marina Pinelis, my wife, Susanna, and my brother, Lev. Their constant encouragement, unfailing support and boundless love have always been the true sources of strength and inspiration throughout my life. Thank you with all my heart.

TABLE OF CONTENTS

LIST OF FIGURES

LIST OF TABLES

LIST OF APPENDICES

ABSTRACT

A high-throughput method for *in vitro* generation of oxygen and mass transfer microgradients was developed. This method not only overcomes many limitations of the previous approaches, but also provides a comprehensive experimental and modeling framework for future studies. To demonstrate this method, microfluidic devices and associated fabrication processes were developed. The microfluidic devices consisted of capillary channels with sizes ranging from 30-300 μm in height to 0.3-3 mm in width, loading reservoirs and microfluidic interconnects. The overall device size was $38\times18\times1.3$ mm^3. The fabrication process was based on SU-8 photolithography and glass to SU-8 bonding. Because of the sizes of the capillaries, diffusion, and not convection, dominated mass transfer and oxygen microgradients were generated, by diffusion limitations and cellular respiration, within 0.5–3 mm of the capillary edges. The method is based on diffusion and, therefore, more closely mimics the *in vivo* microenvironments within multicellular tissues. Measurements of cell viability, pH, differentiation and oxygen were performed for C2C12 and HeLa cells cultured in the mass transfer gradients. Oxygen was measured using the fluorescence lifetime imaging method (FLIM) with spatial resolution of 1 mm and measurement resolution of 0.1 parts per million of dissolved oxygen. This method lends itself to high-throughput experimentation; as many as 30 capillary experiments were run in a 24-hour period including cell loading, gradient formation and imaging. Observable differences in cell

morphology became apparent 12-24 hours after seeding. The developed finite element model (FEM) accommodates a wide range of device geometries and metabolic parameters and couples cellular metabolism with diffusion effects. The model predictions for dissolved oxygen levels and live cell densities were within 5-15% of measured data.

CHAPTER 1

INTRODUCTION AND BACKGROUND

1.1 Introduction

How does a human embryo know how to develop specific organs and body parts from a homogeneous mass of cells? How do wound healing cells such as polymorphonuclear neutrophils and macrophages know where their assistance is needed? What makes certain tumors malignant? The exchange of chemical messages between cells is crucial to much of development and disease. Due to convection and diffusion processes at work in tissue, the exchange of chemical information occurs in (and can generate) heterogeneous or graded chemical environments [28,29,30]. These microgradients are present throughout the human body and other complex organisms; they drive the processes of cell development, differentiation, growth, aging and death [14,17,28,30].

While chemical microgradients are continually occurring *in vivo*, it has been challenging to reproduce and study them *in vitro*. The micro and nano technological advances during the past 10 years have opened up opportunities for an increasingly complex set of experiments which are enabling the scientific community to make unprecedented discoveries about how organisms develop, keep themselves healthy, and fight disease. In particular, micro and nano technologies have enabled a new generation of devices to study microgradients in mammalian cells.

While basic techniques for studying cell culture microgradients *in vitro* have existed for at least 100 years, it is the relatively recent advent of MEMS and microfluidic

technologies that have enabled the research community to conduct sophisticated experiments and study cellular chemotaxis, differentiation, hypoxia and other biological phenomena.

1.2 Significance of oxygen microgradients

In mammalian tissue, gradients of diffusible molecules, among them dissolved gases, have been implicated in various processes including morphogenesis, cell growth and death, and development of cancer [14,15,15,17,28]. These gradients have historically been difficult to reproduce experimentally, but over the last decade a number of microfluidic devices have been developed to reproduce diffusible chemical gradients in cell culture [14,17,20,24,27,28]. Despite these advances, gradients of dissolved gases – among them O_2, CO_2 and NO – have remained challenging to reproduce *in vitro*; this is mostly due to the molecules' small size and, therefore, relatively fast diffusion rates through the materials used in most microfluidic research. For example, elastomers, traditionally very popular with microfluidic applications, have high diffusion constants for gases (e.g., 10^{-3} mm^2 s^{-1} for O_2) [14,28].

Cell culture studies of oxygen microgradients are important because oxygen tensions on some mammalian cells dictate how they will develop [14,24,28]. For example, hypoxia-inducible factors (HIFs) are vital to organism development. Some examples include:

- HIFs often regulate cell differentiation including such processes as embryo development, the formation of blood vessels and wound healing [31]

- HIFs and HIF inhibitors have recently been used as therapeutic targets in treatment of such diseases as anemia [32]

Thus, it is crucial to have methods for establishing and studying the effects of oxygen microgradients *in vitro*. There are a few available methods but all of them have limitations. Also, most non-microfluidic gas gradient techniques, including sandwich culture and capillary methods, have not previously lent themselves well to integration with microfluidics.

1.3 Oxygen Microgradient Generation Methods: The State of the Art

The purpose of this section is to provide a comprehensive overview of the state-of-the-art *in vitro* microgradient oxygen generation devices and techniques.

Existing devices for generating dissolved gas gradients across cell and tissue culture fall into four broad categories: mass transfer-limited methods such as capillaries and sandwich cultures, mixer-perfusion fluidic devices, three-dimensional cell spheroids, and microdevices which electrochemically generate gases into culture. The following table summarizes the limitations for each of the existing methods:

Method	Benefits	Limitations	Ref.
Capillaries and "Sandwich" Cultures	-- simple setup -- well established method	-- limited to monolayer cell culture -- no precise control of the gradient profile -- low throughput, slow	[35]
Fluidic Perfusion	-- allows for separating oxygen mass transfer from other effects	-- requires continual flow -- usually cannot microfabricate with PDMS; oxygen diffuses through it -- low throughput, slow	[14, 33, 34, 36]
Cell Spheroids and 3D Constructs	-- closely mimics real 3D tissue	-- only works for self adherent cells -- spheroid size hard to control -- cumbersome to grow spheroids and image -- low throughput, slow	[24]
Electrolytic Generation	-- precise control of oxygen profiles in time and space	-- complicated setup; inaccessible to most researchers -- long fabrication times -- low throughput, slow	[28]

Table 1.1: Comparison of oxygen microgradient generation methods.

The following section describes each of the above state-of-the-art methods in more detail.

Capillaries and Sandwich Culture

The classic way to limit mass transfer of diffusible gases (and, thus, generate gradients) was the cylindrical gas capillary tube, first used over a hundred years ago [1,2,3]. In the more modern sandwich culture techniques [4], a monolayer of cells was "sandwiched" between two gas impermeable cover slips; this limited mass transfer between the center of the cell mass and the edges. This mass transfer limitation, coupled with cell metabolism, generated gradients of O_2 and CO_2 molecules between the center and the edges of the plates. For example, Figure 1.1 shows a picture of a *capillary assay* for bacterial aerotaxis that was performed with *Bacillus subtilis*, an obligate aerobe.

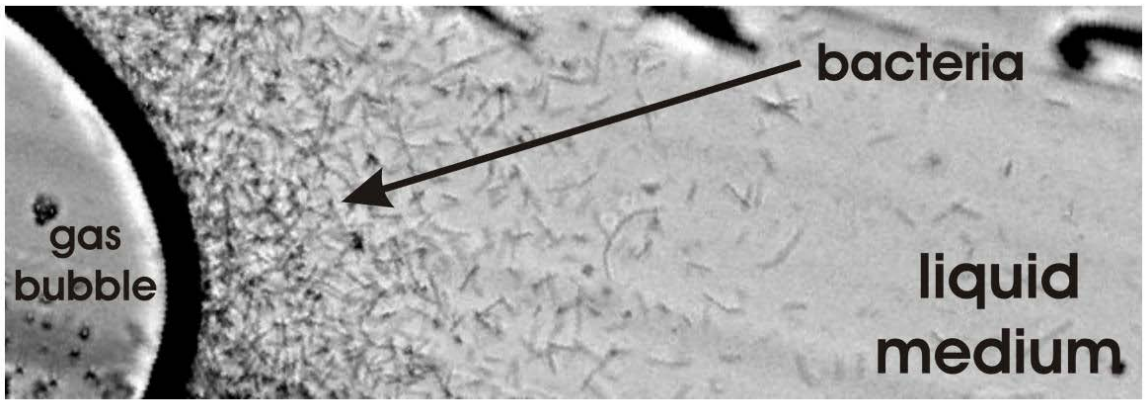

Figure 1.1: Aerotaxis assays based on gas-liquid interfaces are the current state-of-the-art. In this experiment, B. subtilis forms a clear band directly around the interface. Bacteria with lower oxygen requirements will form bands farther away from the interface (at their preferred oxygen concentration) [27].

Here, a bacterial suspension of known density was loaded into a square cross-section capillary. If, as in this case, the bacteria under analysis have a preference for a specific

oxygen concentration, they will assemble into a band at a certain distance from the gas-liquid interface; this can be seen clearly in Figure 1.1 The width and location of the band is dependent on the oxygen concentration in the gas phase, the oxygen consumption rate of the bacteria, and motility-specific parameters [6,7,12]. Note that the oxygen gradient from the interfaces is not easily altered, nor is is trivial to have the bacteria assemble in different configurations. Moreover, dynamic alterations in either the spatial or temporal characteristics of the oxygen microgradients are very difficult [5,8,12,13].

Certain modifications to this basic procedure are possible; these include: 1) trapping gas bubbles between two glass coverslips and 2) changing the composition of the gas headspace rapidly (~10 sec) to observe bulk changes in tumbling frequency [5,8]. These all suffer from similar limitations to those discussed above. The specifics of oxygen and the related 'energy' taxis mechanisms are discussed in detail in several excellent reviews [9,10,11].

Another well established oxygen generation method, an especially for mammalian cell experiments, is sandwich culture. As shown in Figure 1.1a below, in this method, a monolayer of mammalian cells are "sandwiched" between two plates of transparent material, usually glass, and the diffusion of oxygen is limited to mass transfer through the narrow slit between the top and bottom plates. For example, Cochran *et al* used this method to characterize and model glucose consumption in mammalian cells [35].

This method is limited to monolayer cell culture for mammalian cells and, in general, offers no precise control of the gradient profile and has low throughput.

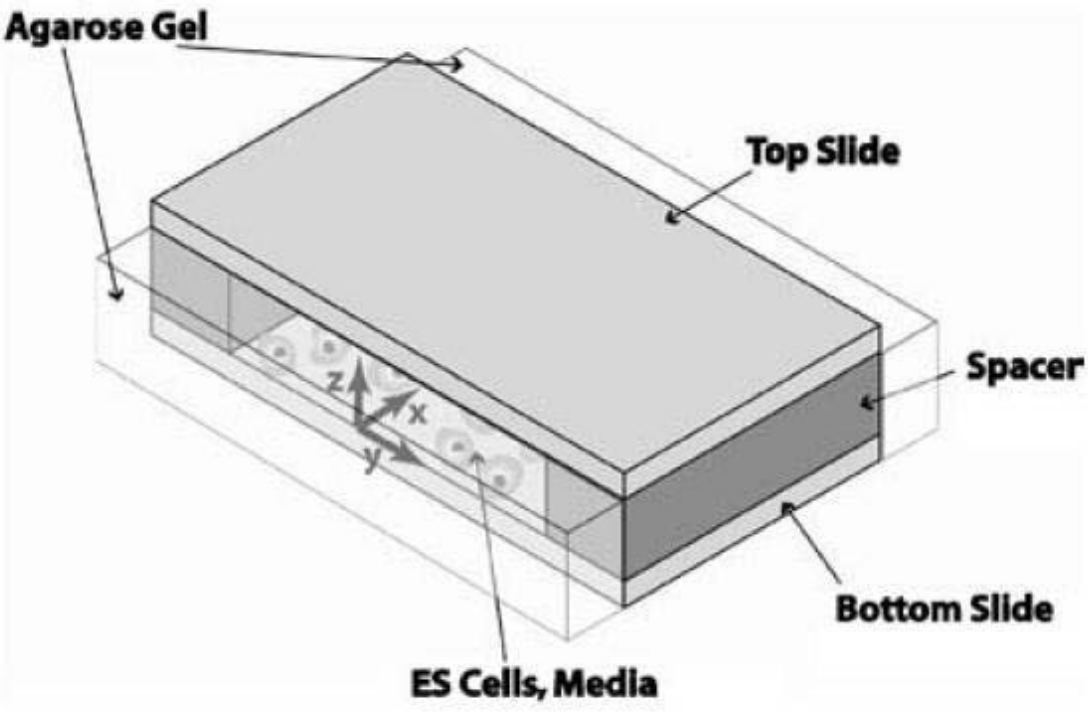

Figure 1.1a: Example of a sandwich culture device. Principal diffusion of oxygen, glucose, other nutrients and waste is along the x-axis [35].

Fluidic Perfusion

A small number of fluidic mixer-perfusion devices [14,15,16] generated gradients by flowing a gas-rich medium along long channels of cultured cells; cells nearest the entry port received more gas than those nearer the ends of the channel [17,33,34].

A typical set up is shown in Figure 1.2 below. Oxygen-rich media enters from the left and flows over a monolayer of cells on the bottom of the dish. As media flows over the cells, they consume the oxygen dissolved in the media and thus a gradient of oxygen is established across the dish.

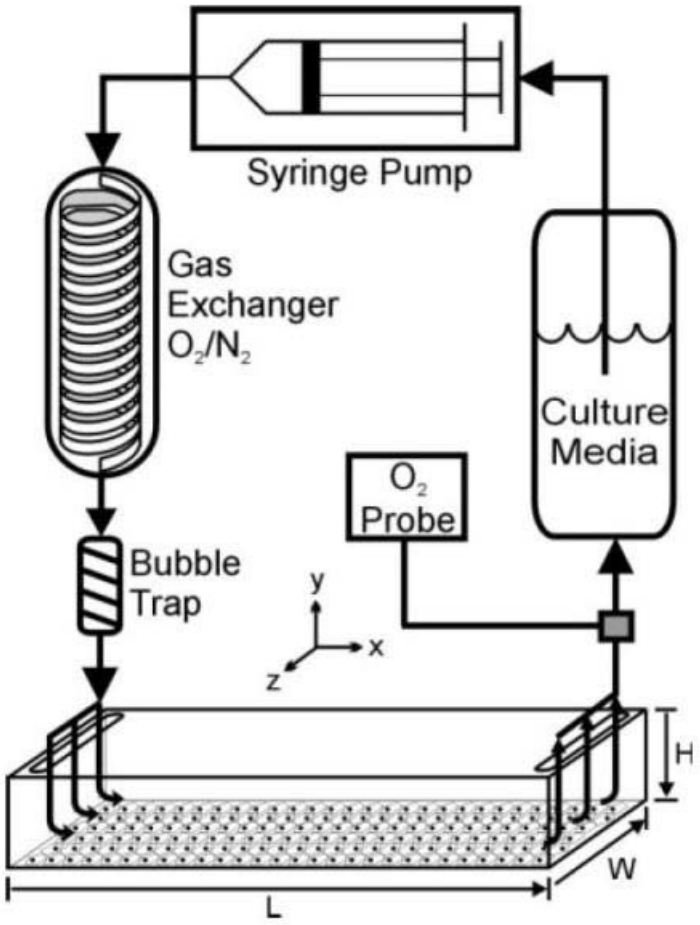

Figure 1.2: The fluidic perfusion oxygen gradient generation method. Oxygenated media enters from the left and travels along the monolayer of cells that are on the bottom of the dish. As the media flows over the cells, the dissolved oxygen is consumed and a gradient is established [14].

This method is limited to schemes that require oxygenated media flow; this, in turn, significantly complicates experimental set up. Another problem with this method is that the media flow produces shear stress on the cells; this limitation, however, has been resolved somewhat with recently presented work that separates cell culture chambers and flow channels. An example of this work is described in Figure 1.2a below.

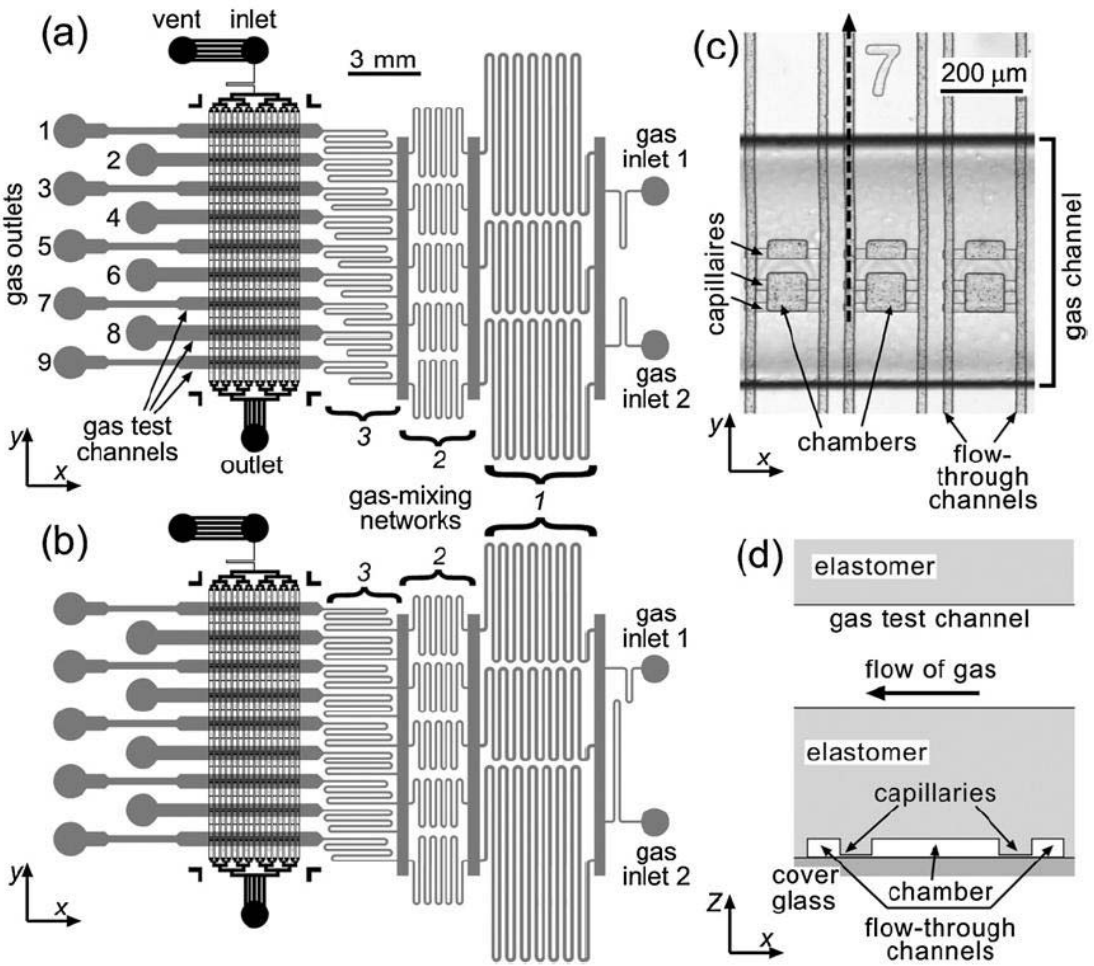

Figure 1.2a: Example of a fluidic perfusion device where cell culture chambers and gas flow channels are separated. In this recently reported device, gases with varying levels of oxygen are mixed in stages to produce graded amount of oxygen in channels that are then flowed orthogonally to capillaries connected to cell culture chambers. Notably, this device requires a complicated setup and has so far been only demonstrated with bacteria [33].

Cell Spheroids and 3D Constructs

Some cell types, particularly those which are tumor-forming, can be coaxed into forming spheroidal clumps when cultured in suspension. These "clumped" three-dimensional clusters limit mass transfer and generate oxygen gradients between the center and edges [18]. An example of such a spheroid is shown in Figure 1.3 below.

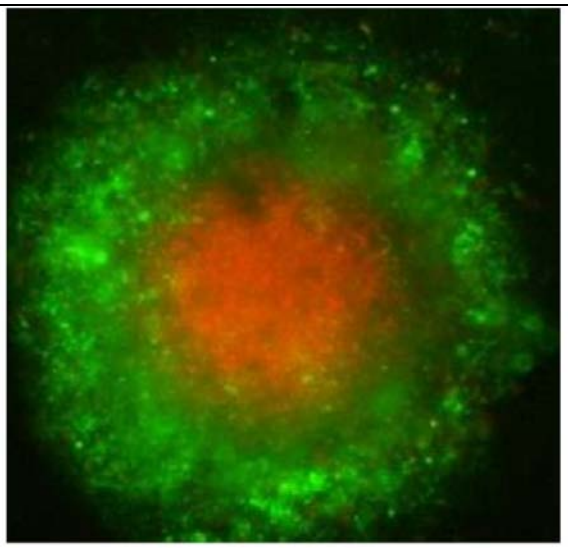

Figure 1.3: A tumor spheroid constructed from cancer cells. Here, live cells fluoresce in green; dead cells in red. The oxygen gradient is established by the cells due to their consumption of oxygen and its time-limited diffusion. Cells on the periphery consume most of the diffusing oxygen before it has a chance to penetrate into the center of the spheroid [24].

In general, three-dimensional multi-cellular constructs play an increasingly important role in studies of tissue engineering, cancer and drug delivery [19,20,21,24,25]. Unlike two-dimensional monolayer culture, 3D constructs capture some of the complexity of solid tissue [19] and both mechanical and chemical cell-to-cell interactions play a role in the development of both normal and diseased states of tissue [22]. In cancer biology, multi-cellular tumor spheroids are currently being used as *in vitro* models for studying the development of tumor malignancy and drug response assays [19,23,25]. In particular, previously reported work resulted in measurements of cell viability and pH in non-vascularized tumor spheroids [23].

For example, as shown in Figure 1.4 a new class of device was developed to study the micro-environmental niches created within three dimensional tissue constructs as a result of diffusion limitations [24]. These include, for example, the lack of oxygen (hypoxia) and the pH change at the center of multi-cellular masses.

Figure 1.4 illustrates the device concept and geometry. To assemble the multi-cellular constructs, individual cells in suspension were flowed into microchannels containing

arrays of embedded posts ranging in size and spacing from 10-30μm; these posts are arranged so as to form "baskets" of desired shapes and sizes. As cells flowed by, some fraction became trapped in these 'baskets' and assemble into cylindroids and cubes (Figure 1.4).

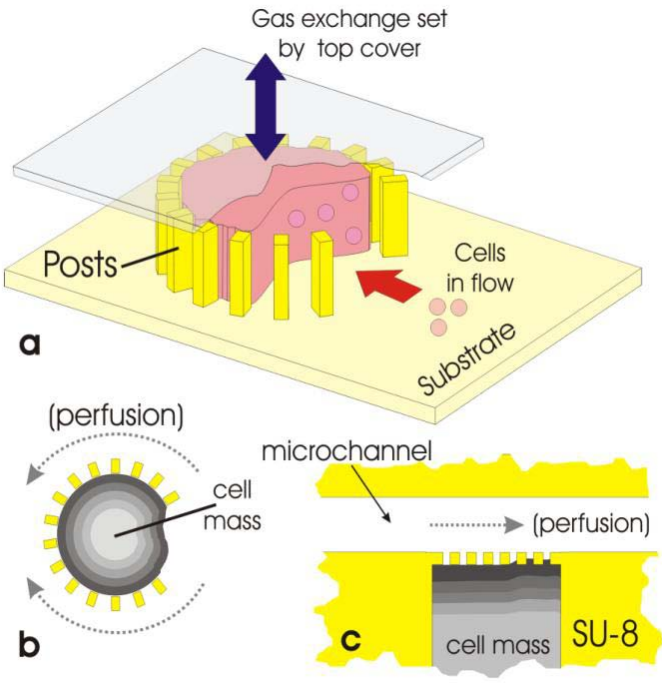

Figure 1.4: a) Schematic view of device operation, b – c) different "basket" geometries generate different diffusion gradients in 3D cellular constructs (shown schematically in gray-scale) [24].

This method and device offered improvement over traditional macroscopic culture techniques for assembling three-dimensional isotropic constructs, which have a number of drawbacks: large size and shape variability during culture, imaging and microscopy difficulties inherent in spheroidal cell masses, and the practical difficulties of maintenance and passaging of cultured constructs [23].

This microfluidic device and method for the assembly and continuous culture of three-dimensional multi-cellular constructs is particularly useful for generating micro-environmental niches (such as hypoxia and acidosis) in non-vascularized tissue. The

technique: 1) allows the rapid, parallel assembly of dozens of three-dimensional constructs with controlled shapes, sizes and interfacial gas transfer rates, 2) can be extended to adherent cells (which are normally grown in single monolayers) using functionalized glass beads, and 3) permits long-term continuous culture and perfusion of the constructs. Fabrication is shown in Figures 1.5.

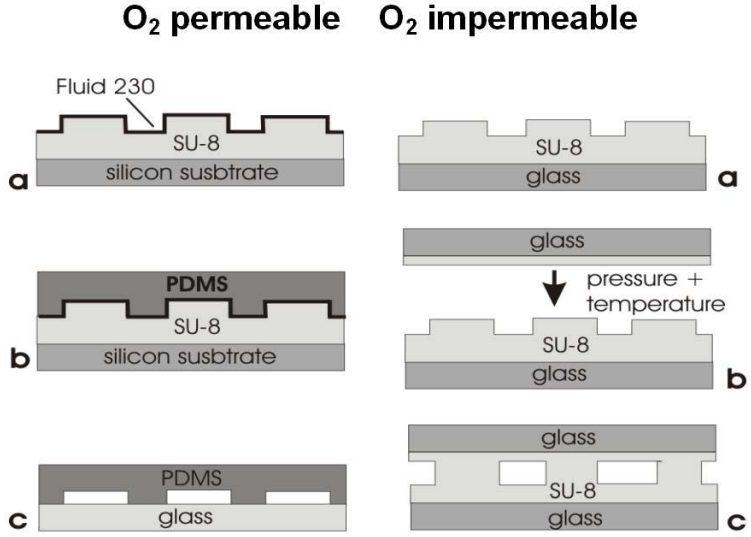

Figure 1.5: Fabrication flow. Two similar processes are used to yield either oxygen permeable or oxygen impermeable 'baskets'. *(left)* Lithographically-patterned SU-8 is used to mold spun PDMS. The PDMS is then bonded to a glass wafer. *(right)* Lithographically-patterned SU-8 is bonded to a glass substrate using Microform film (Microchem, Newton, MA) [24].

Figure 1.6 below shows the structures formed in SU-8. High aspect ratios of 1:10 to 1:20 were achieved.

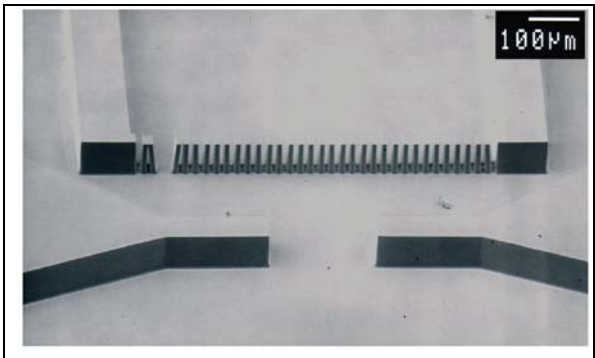

Figure 1.6: Scanning electron micrograph of devices before assembly. Due to the high aspect ratios (1:10 to 1:20), the posts are fragile and can break off or stick to each other during handling [24].

This device was used to: 1) assemble 200µm thick *Zinnia* plant cell cylindroids with patterned diameters ranging from 200-800µm and culture them for 24 hours, 2) demonstrate the feasibility of quantifying diffusional limitations of a dense tissue mass with a fluorescent oxygen-sensitive Tris(2,2'-bipyridyl)dichlororuthenium(II) hexahydrate fluorophore, 3) assemble three-dimensional constructs with 50µm diameter glass beads (G.Kisker, Germany) intercalated with adherent C2C12 myoblast cells, 4) assemble three-dimensional constructs with 50µm diameter glass beads (G.Kisker, Germany) intercalated with adherent HeLa cancer cells, cultured them for 72 hours and imaged them with LIVE/DEAD™ cell viability assays, and 5) culture clusters of colon carcinoma cancer cells for 1 week.

In addition, C2C12 myoblasts (which have a known sensitivity to oxygen during differentiation) and colon carcinoma cells (which are a common non-vascularized tumor model [7] and aggregate without the need for beads) were assembled, cultured and the resulting constructs monitored for 7 up to days and analyzed with LIVE/DEAD assays [26].

This method is limited to only self-adhering cells or cell-bead suspensions.

Electrolytic Generation

Another microfluidic technique introduced oxygen or nitric oxide into culture by generating it electrochemically from a water reservoir below the cell culture chamber [28]. This method of generating oxygen gradients with microscale resolution can be used to perform: 1) dynamic response assays of mammalian cell culture and bacterial suspensions not possible with existing methods, and 2) studies on oxygen responses of

single mammalian cells or bacterium (Figure 1.7). The basic premise only functions in a microscale environment. This method can be also used to self-assemble large-density and small numbers of bacteria into pre-determined patterns using aerotaxis.

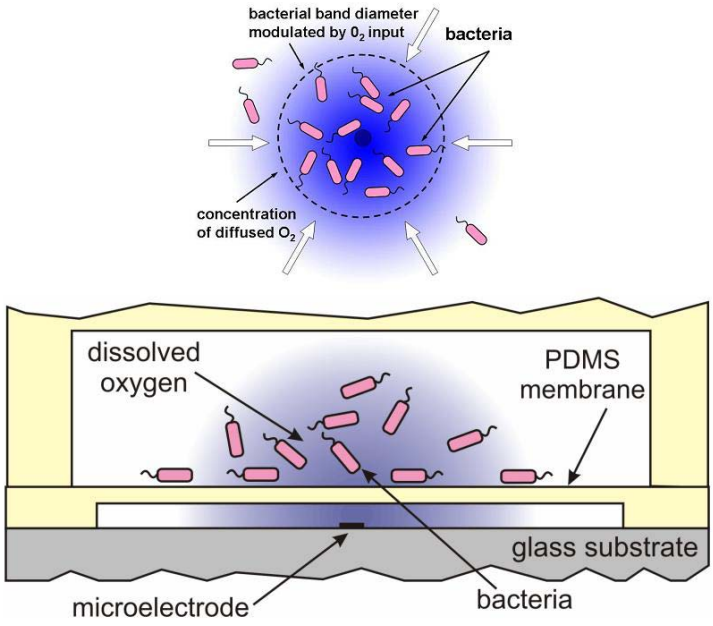

Figure 1.7: Schematic of bacterial aerotaxis assay. The oxygen is generated by running a known current through the electrodes in the electrolyte chamber. The oxygen then flows to the upper chamber which holds the cell culture. *B.subtilis* bacteria are attracted to areas with higher O_2 concentrations and bacterial bands aggregate around O_2 sources [27].

This method uses electrolysis at many microelectrodes to generate controlled doses of dissolved oxygen; these doses can be superimposed to pattern microscale gradients with precise spatial and temporal resolution.

Figure 1.7a illustrates the basic concept of this method. In brief, a glass substrate is patterned with Ti/Pt electrodes; on this, photoresist is spun and patterned into molds for microfluidic channels. The photoresist is removed using acetone, leaving buried microchannels. A second PDMS layer with pre-molded microchannels is then bonded above the first PDMS microchannel using an O_2 plasma.

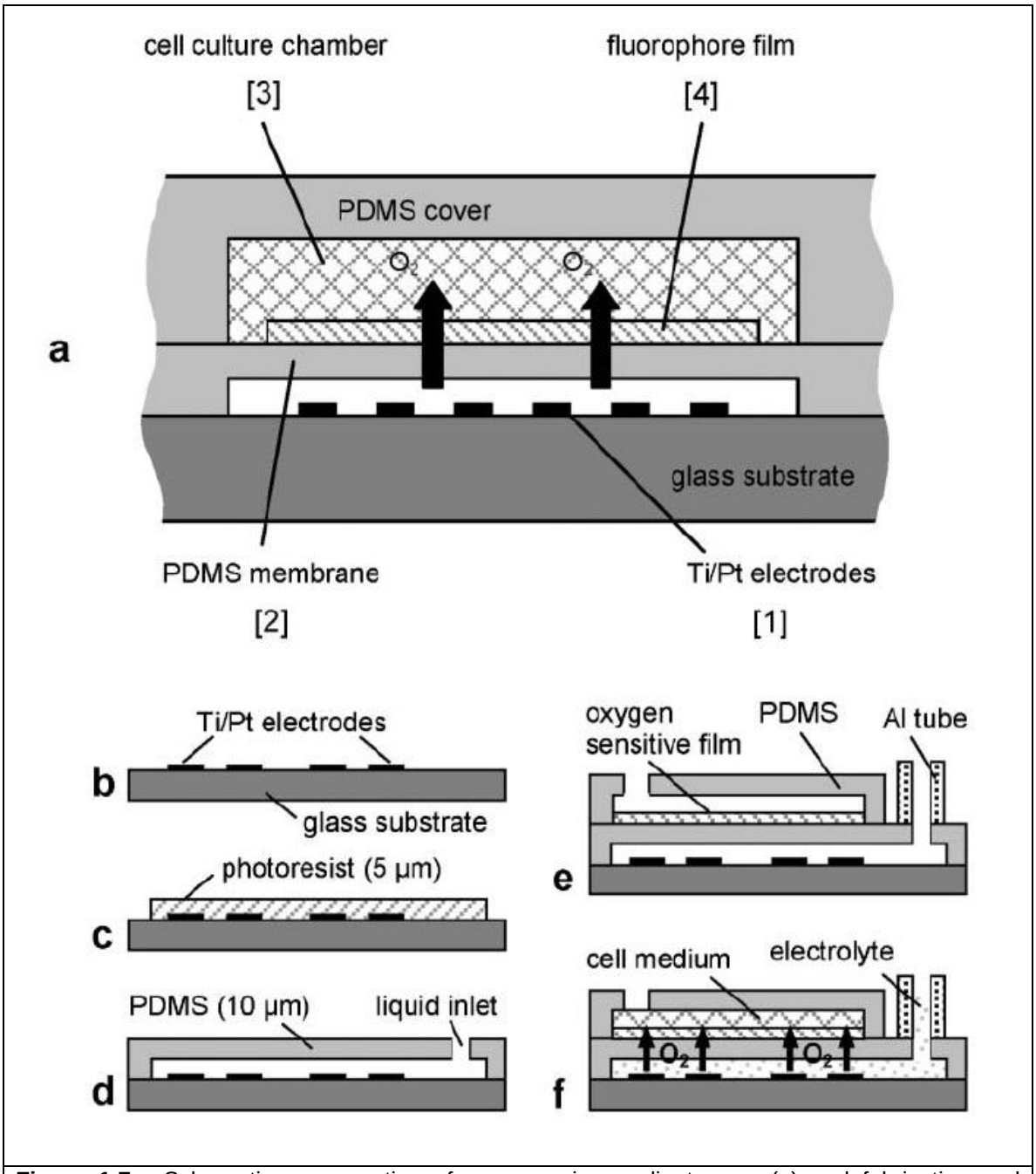

Figure 1.7a: Schematic cross-section of oxygen microgradient array (a) and fabrication and assembly process (b–f) [28].

During operation, the bottom microchannel layer is filled with DI water and the upper microchannel layer is filled with the bacterial suspension under test. In a variant of the device, the PDMS cell culture chamber was replaced with a commercial macroscale cell culture plate whose floor was removed and replaced with the fabricated device (glass

substrate + electrodes + PDMS microchannels filled with DI water). Note that a gas-permable membrane effectively separates the DI water from the bacterial suspension. Dissolved oxygen (no bubbles) is generated in the DI water at a Ti/Pt microelectrode when biased as an anode and current is run between it and a microelectrode Ti/Pt cathode (not shown and positioned distant from the anode and area under test [5,28]). This generated oxygen is then free to diffuse through the PDMS membrane and into the cells above; in this way, microelectrodes can be used to generate oxygenated areas in cell culture. By superimposing the oxygen generated by different, adjacent microelectrodes and/or patterning microelectrodes with specific shapes, the user can essentially "draw" oxygen profiles into the culture.

For example, in an experiment with the aerotaxis of *B.subtilis*, with no oxygen input from the microelectrodes, bacteria in suspension tumble about performing random walks across the cell culture chamber [27]. Given an oxygen input, the bacteria taxed, or migrated, towards the oxygen source while consuming oxygen. Within minutes, bacteria self-assembled out of the initially homogenous suspension and formed a shape that was similar to the pattern of the electrodes. The size of the band or aggregate depended on the oxygen input from the electrode, the bacterial consumption rate and the initial density of bacteria. After a few minutes, the bacterial density gradient reached a steady-state with bacteria concentrated on the electrode (as in Figure 1.8).

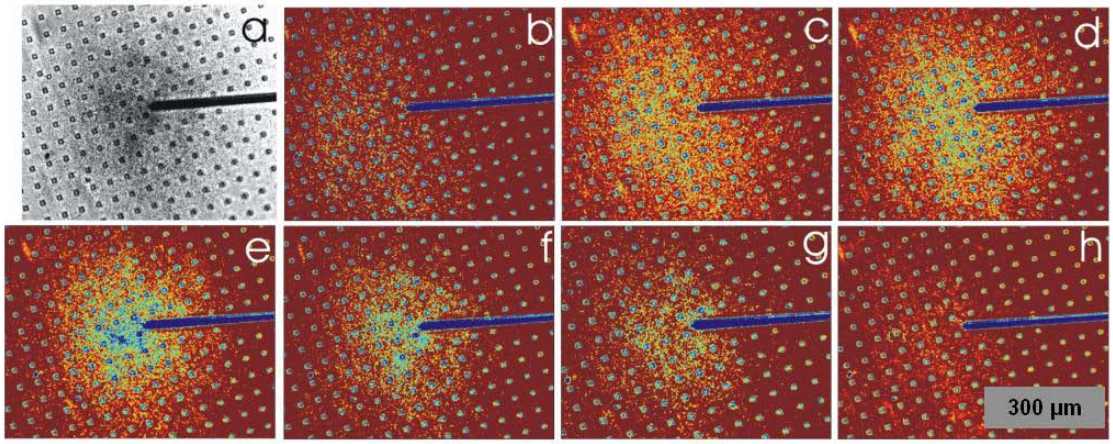

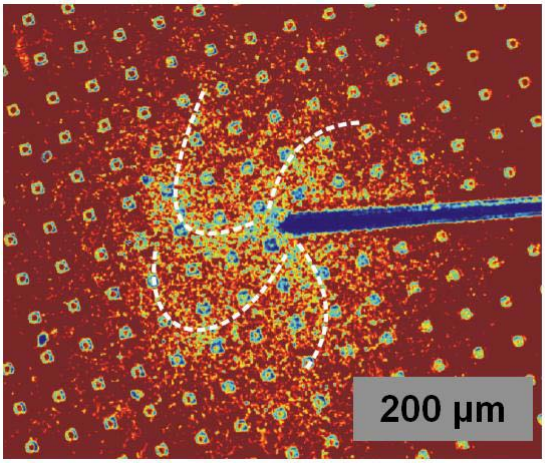

Figure 1.8: Oxygen supply were dynamically lowered by reducing the current through the point source electrode from 0.5mA to 0.1mA in steps of 0.1mA over 10 minutes; pictures are approximately 90 seconds apart. Pseudo color micrographs of a bacterial band around a single point source; a) and f) are identical. As the bacterial "cloud" collapsed onto the point-source electrode the band formed "windmill" patterns (left) [27].

Beyond sensitive assays of bacterial pattern formation at high-densities, this method allowed the performance of assays of motility and oxygen response of single bacterium as well as studies of mammalian cells.

For example, as shown in Figure 1.9 below, hyperoxia-induced apoptosis of C2C12 cells was demonstrated with this method.

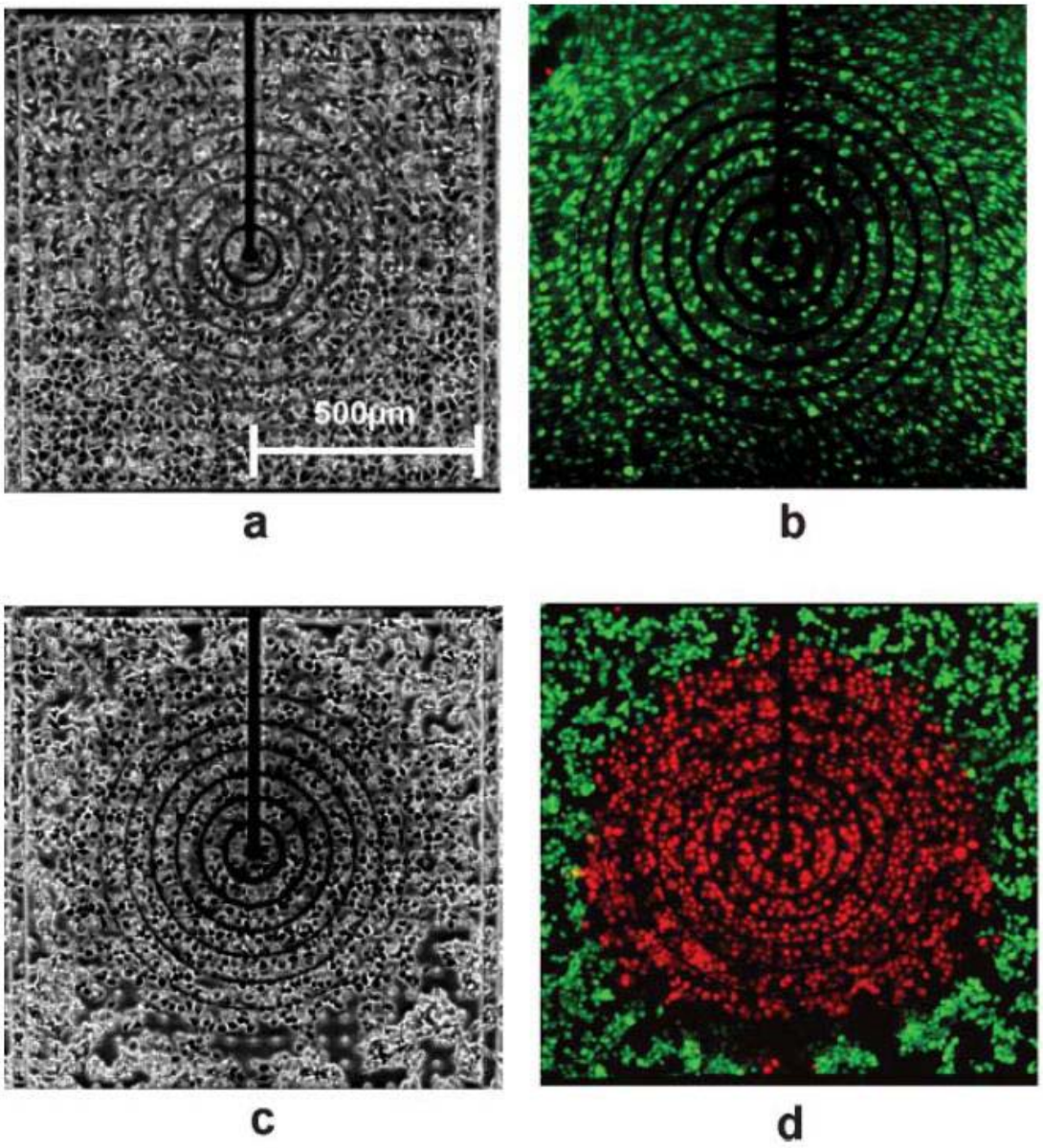

Figure 1.9: Hyperoxia-induced apoptosis in C2C12 myoblasts. a) 2 h after seeding (without oxygen input from OMA) b) LIVE/DEAD image of myoblasts after 72 h in anaerobic chamber (95% N2 : 5% CO2), with constant oxygen delivery via a concentric circle electrode. c) 2 h after applying current density of 10 mA mm22. e) Fluorescent image of d) with LIVE/DEAD stain [27].

Although this method offers lots of flexibility with oxygen microgradient temporal and spatial parameters, it is limited by its complicated setup, inaccessibility to most researchers, long fabrication times, and low throughput.

1.4 State-of-the-art summary and research goals

As presented in the sections above, all of the existing methods for generating oxygen microgradients *in vitro* have limitations. Thus, it is desirable to develop a well-characterized method that overcomes these limitations as described in Table 1.1 above while being accessible to the biological research community.

Such a method was developed and is described in the next chapter. The method is applicable to forming microgradients of oxygen and other small molecules that are metabolized by mammalian cells, offers simple preparation and fabrication, and results in controllable and predictable gradient profiles. The method lends itself to many oxygen-related experiments such as those with angiogenesis, cell invasion, and self-adhering cells such as those used by tumor spheroid community.

As described in the next chapter, this method has been demonstrated and characterized with two types of cell culture, HeLa cancer cells and C2C12 muscle precursor cells.

Specifically, contributions include:

- Establishment of a simple and useful method for generating, maintaining and monitoring oxygen microgradients
- Demonstration of oxygen gradient formation with HeLa cancer cells with measurements of cell viability and pH
- Demonstration of gradient formation and possible differentiation of C2C12 cells

Further contributions are described in Chapter 3 and include:

- Demonstration of gradient formation with direct oxygen measurements
- Development of a metabolic and mass transfer model
- Development of an integrated prototype device

Chapter 1 References

1. Y. Okon, L. Cakmakci, I. Nur & I. Chet, "Aerotaxis and chemotaxis of Azospirillum brasilense: A note," *Microbial Ecology* 6, 277-280, 1980.
2. S.I. Bibikov, R. Biran, K.E. Rudd & J.S. Parkinson, "A signal transducer for aerotaxis in Escherichia coli," *J.Bacteriology* 179, 4075-4079, 1997.
3. S.I. Bibikov, L.A. Barnes, Y. Gitin & J.S. Parkinson, "Domain organization and flavin adenine dinucleotide-binding determinants in the aerotaxis signal transducer Aer of Escherichiacoli," *Proc. Natl. Acad. Sci.* 97, 5830-5835, 2000.
4. D.M. Cochran *et al*., "Evolution of oxygen and glucose concentration profiles in a tissue-mimetic culture system of embryonic stem cells," *Annals of Biomedical Engineering* 34, 1247-1258, 2006.
5. J.H. Park, T. Bansal, B.H. Chueh, S. Takayama & M.M. Maharbiz, "Electrolytic Patterning of Dissolved Oxygen Microgradients During Cell Culture", *The 18th IEEE International Conference on Micro Electro Mechanical Systems,* Miami, 2005.
6. J.S. Parkinson & D.F. Blair, "Does *E. coli* have a nose?" *Science* 259, pp. 1701-1702, 1993.
7. J.S. Parkinson, "Signal transduction schemes of bacteria," *Cel,* 73, 857-871, 1993.
8. A. Eschemann, M. Kuhl & H. Cypionka, "Aerotaxis in *Desulfovibrio*", *Environ. Microbiol.*, vol. 1, 489-494, 1999.
9. T.W. Grebe& J. Stock, "Bacterial chemotaxis: The five sensors of a bacterium," *Curr. Biol.*, vol. 8, R154-157, 1998.
10. B.L. Taylor, I.B. Zhulin & M.S. Johnson, "Aerotaxis and Other Energy-Sensing Behavior in Bacteria," *Annu. Rev. Microbiol*., vol. 53, 103-128, 1999.
11. B.C. Mazzag, I.B. Zhulin & A. Mogilner, "Model of Bacterial Band Formation in Aerotaxis," *Biophys. Jour*., vol. 85, 3558-3574, 2003.
12. L.S. Wong, M.S. Johnson, I.B. Zhulin and B.L. Taylor, "Role of Methylation in aerotaxis in *Bacillus subtilis*," *J. Bacteriol*., vol. 177, 3985-3991, 1995.
13. D. Emerson, R.M. Worden & J.A. Breznak, "A Diffusion Gradient Chamber for Studying Microbial Behavior and Separating Microorganisms." *App. and Environ. Microbiol*., vol. 60, 1269-1278, 1994.
14. J.W. Allen & S.N. Bhatia, "Formation of steady-state oxygen gradients in vitro: Application to liver zonation," *Biotechnology and Bioengineering* 82, 253-262, 2003.
15. J.P. Sullivan & A.F. Palmer, "Targeted oxygen delivery within hepatic hollow fiber bioreactors via supplementation of hemoglobin," *Biotechnology Progress* 22, 1374-1387, 2006.
16. J.P. Sullivan, J.E. Gordon & A.F. Palmer, "Simulation of oxygen carrier mediated oxygen transport to C3A hepatoma cells housed within a hollow fiber bioreactor," *Biotechnology and Bioengineering* 93, 306-317, 2006.
17. S. Takayama *et al*., "Patterning cells and their environments using multiple laminar fluid flows in capillary networks," *PNAS* 96, 5545-5548, 1999.
18. R. Venkatasubramanian, M.A. Henson & N.S. Forbes, "Incorporating energy metabolism into a growth model of multicellular tumor spheroids," *Journal of Theoretical Biology* 242, 440-453, 2006.

19. J.M. Kelm, N.E. Timmins, C. J. Brown, M. Fussenegger & L. K. Nielsen, “A method for the generation of homogeneous multicellular tumor spheroids applicable to a wide variety of cell types,” Biotechnol Bioeng 83, pp. 173-180, 2003.
20. R.M. Sutherland, “Cell and environment interactions in tumor microregions: the multicell spheroid model,” *Science* 240, pp. 177-184, 1988.
21. P.J. Hung, P. J. Lee, P. Sabounchi, N. Aghdam, R. Lin & L.P. Lee, “A novel high aspect ratio microfluidic design to provide a stable and uniform microenvironment for cell growth in a high throughput mammalian cell culture array,” *Lab Chip* 5, pp. 44-48, 2005.
22. G. Hamilton, “Multicellular spheroids as an in vitro tumor model,” *Cancer Letters* 131, pp. 29-34, 1998.
23. N.S. Forbes, L.L. Munn, D. Fukumura & R.K. Jain, “Sparse Initial Entrapment of Systemically Injected Salmonella typhimurium Leads to Heterogeneous Accumulation within Tumors,” *Cancer Research* 63, pp. 5188-5193, 2003.
24. M. Pinelis, R.W. Kasinskas, R.T. Borno, J. Park, E. Chu, N.S. Forbes, M.M. Maharbiz, "Microfluidics devices for the assembly and culture of three-dimensional multi-cellular constructs with diffusion-limited microenvironments," *Tenth International Conference on Miniaturized Systems for Chemistry and Life Sciences (MicroTAS)*, Tokyo, Japan, November 2006.
25. C.J. Flaim, S. Chen & S.N. Bhatia, “An extracellular matrix microarray for probing cellular differentiation,” *Nature Methods* 2, 119-125, 2005.
26. R.W. Kasinskas & N.S. Forbes, “Salmonella typhimurium specifically chemotax and proliferate in heterogeneous tumor tissue in vitro,” *Biotechnol Bioeng* 94, 710-721, 2006.
27. M.Pinelis, J. Park & M.M. Maharbiz, "A Micro "Flea Circus": Self Assembly of Bacteria through Spatio-Temporal Control of Aerotaxis," *IEEE/ASME International Conference on Micro Electro Mechanical Systems (MEMS 06)*, Istanbul, Turkey, January 2006.
28. J.H. Park, T. Bansal, M. Pinelis & M.M. Maharbiz, “Electrolytic patterning of dissolved oxygen microgradients during cell culture," *Lab on a Chip* 6, 611-622, 2006.
29. D.B. Weibel and G.M.Whitesides, "Applications of microfluidics in chemical biology," *Current Opinion in Chemical Biology* 10, 584-591, 2006.
30. N. Le Brisa, M. Zbindenb & F. Gaill, “Processes controlling the physico-chemical micro-environments associated with Pompeii worms,” *Deep Sea Research Part I: Oceanographic Research Papers* 52, 1071-1083, 2005.
31. C. Murdoch, M. Muthana & C.E. Lewis, “Hypoxia Regulates Macrophage Functions in Inflammation,” *The Journal of Immunology* 175, 6257-6263, 2005.
32. C.Peyssonnaux et al, “Regulation of iron homeostasis by the hypoxia-inducible transcription factors (HIFs),” *The Journal of Clinical Investigation* 117, 1926-1932, 2007.
33. M. Polinkovsky, E. Gutierrez, A. Levchenko & Alex Groisman, “Fine temporal control of the medium gas content and acidity and on-chip generation of series of oxygen concentrations for cell culture,” *Lab on a Chip* 9, 1073–1084, 2009.
34. G. Mehta et al, “Quantitative measurement and control of oxygen levels in microfluidic poly(dimethylsiloxane) bioreactors during cell culture,” *Biomedical*

Microdevices 9, 123-134, 2007.
35. D. M. Cochran et al, “Evolution of Oxygen and Glucose Concentration Profiles in a Tissue-Mimetic Culture System of Embryonic Stem Cells,” *Annals of Biomedical Engineering* 34, 1247–1258, 2006.
36. A. P. Vollmer et al, “Development of an integrated microfluidic platform for dynamic oxygen sensing and delivery in a flowing medium,” *Lab Chip* 5, 1059–1066, 2005.

CHAPTER 2

A HIGH-THROUGHPUT METHOD FOR *IN VITRO* GENERATION AND STUDIES OF OXYGEN MICROGRADIENTS

As described in Chapter 1, current methods of oxygen microgradient generation have important limitations as summarized in Table 1.1. The oxygen gradient device presented in this chapter overcomes many of these problems. It is assembled inside cell culture plates by bonding a molded PDMS microfluidic network to silica-glass optical fibers of various sizes having hollow rectangular cross-sections (Figure 2.1).

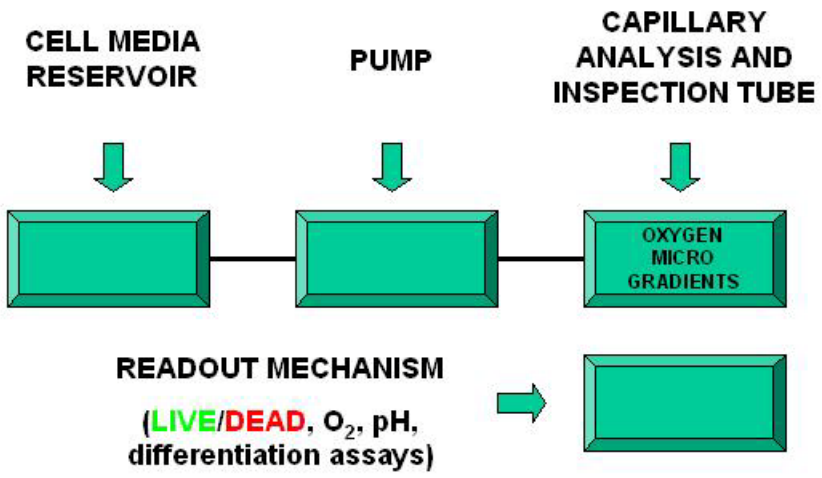

Figure 2.1: The functional structure for the proposed method.

Basic elements of the device include a reservoir, a pump, and a capillary analysis and inspection tube that contains the cells and oxygen-controlled medium. The pump can be connected to multiple capillary tubes to increase experimental throughput as reported in the results presented in this chapter.

The device fabricated for use with this method overcomes most of the limitations encountered with state-of-the-art methods described in Chapter 1. Specifically, the method:

- **is high-throughput**
- **offers precise control of oxygen microgradient profiles**
- **works with self-adherent and non-self adherent cells**
- **is compatible and can be integrated with microfluidics**

By varying capillary sizes, a wide range of oxygen micro gradient profiles can be generated. In addition, since multiple runs of the same experiment can be conducted in parallel in the same Petri dish, the method is readily suited to deliver results that are more statistically significant than results obtained with other methods.

2.1 Device Overview and Methods

This section briefly presents the fabrication and operation of the initial prototype device (Figure 2.2). The subsequent sections of this chapter describe device fabrication and operation in more detail. Results are presented in conjunction with device operation descriptions to better illustrate how this device was used for the described method.

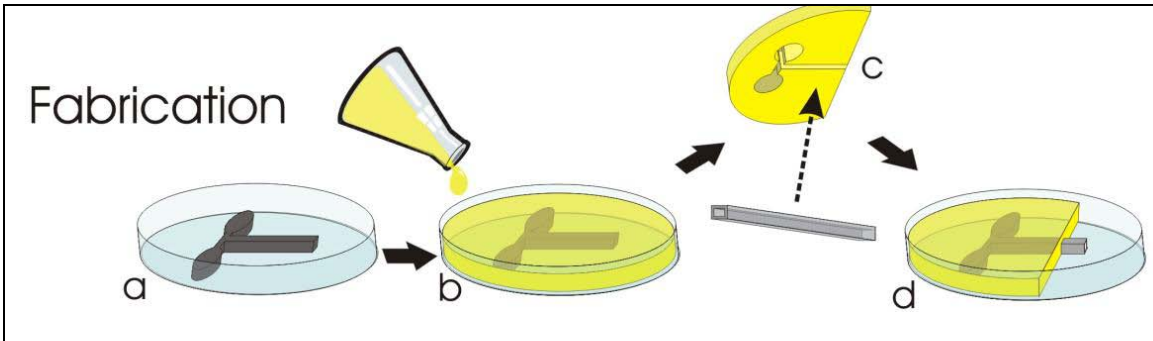

Figure 2.2: Illustration of device fabrication, cell culture, assaying and microfluidic integration. For fabrication, a mold was formed in a culture dish (a) and PDMS was poured over the mold and cured on a hotplate overnight (b). Glass capillaries were then inserted into the PDMS piece and bonded to a fresh culture plate (c,d) [2].

For fabrication, the oxygen gradient device presented in this chapter is assembled inside a Petri dish by bonding a molded PDMS microfluidic network with hollow rectangular cross section silica glass optical fibers of various sizes (Figure 2.2 a,b,c,d).

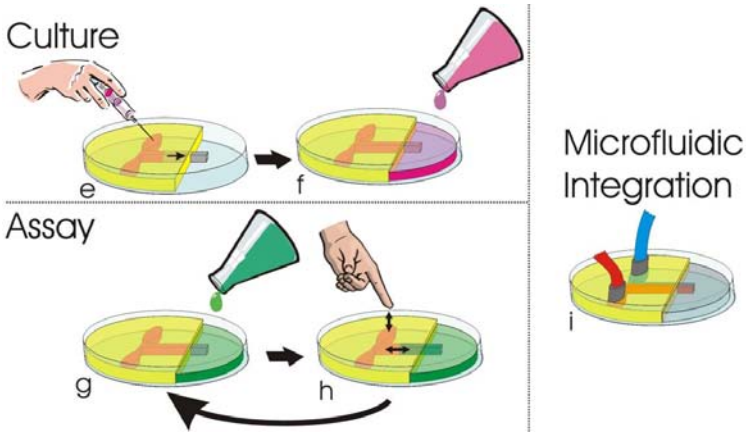

Figure 2.2 (continued): For culture, cell suspension was loaded with a needle into the PDMS reservoir, where it wicked into the glass fiber via capillary forces (e); once the capillary was filled, the plate was filled with medium (f). Once the cell viability gradient was formed, cells were assayed by pouring reagents into the culture dish and then finger-pumping the reservoir to load the reagents (g,h). This device can also be integrated with traditional microfluidics to generate laminar flow gradients within the capillary (i) [2].

For operation, cells in suspension were loaded into a reservoir in the PDMS network and initially filled the silica glass channels by capillary action. Cell culture plates were then filled, as in normal culture, with medium (Figure 2.2 e,f). Cells were loaded into the reservoir via manual syringe dispensing. The reservoir was also used as a pump to deliver chemical reagents and indicators such as the LIVE/DEAD cell viability and pH fluorescent indicators into the capillaries.

2.1.1 Device Fabrication

To fabricate gas-impermeable chambers, commercially available optically flat glass capillaries (Fiber Optic Center, Inc., New Bedford, MA) with inner cavity dimensions varying from 30-100μm in height and 300-1000μm in width were used (Figure 2.3).

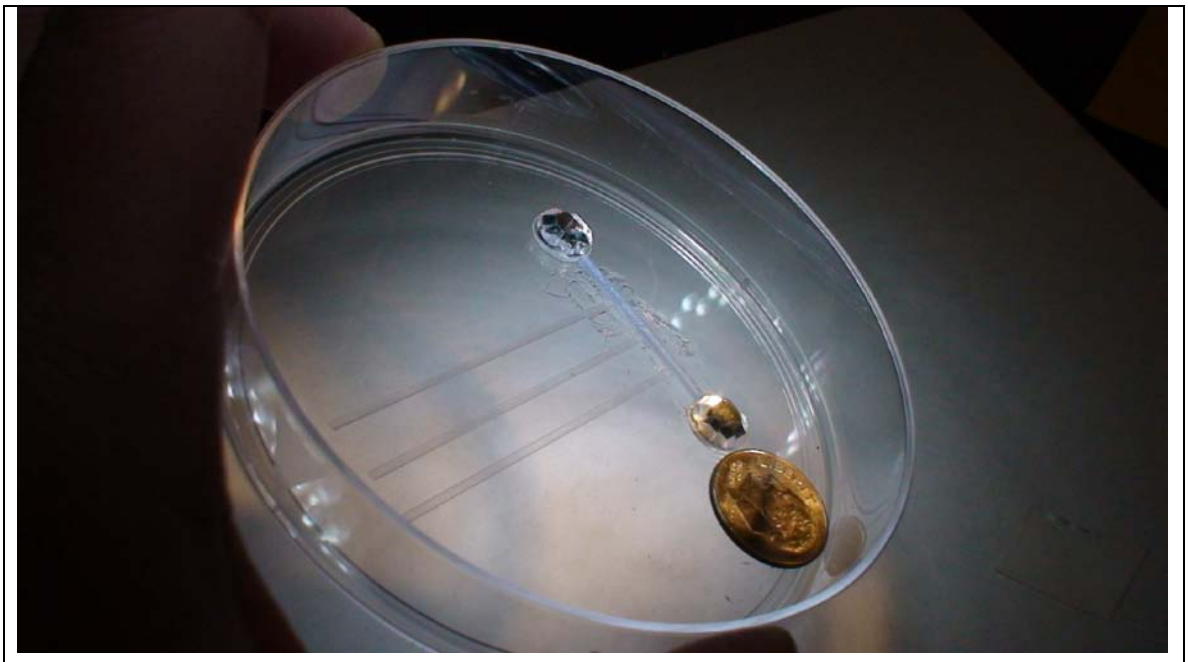

Figure 2.3: An example of a mold used for devices which require microfluidic integration. Here, three capillaries and two inlet ports are connected via a common T-junction [2].

Molds were made using solid plastic buttons that were 3-8mm in diameter (Michael's, Irving, TX) and rectangular capillaries of appropriate sizes (Figure 2.3). The capillaries used for the mold were replaced with new capillaries of the same size in the final assembly of the device.

To form the device manifold, PDMS (Dow Corning, Midland, MI) was mixed with its curing agent in 10:1 ratio and poured over the mold; it was then allowed to sit for 30 minutes so that air bubbles could escape and then baked on a hotplate overnight at 50^0C. Sterile capillaries were then embedded into these custom-made PDMS manifolds which included reservoirs for cell loading. Manifolds were then bonded to cell culture dishes using silicone sealant (Figures 2.4, 2.5).

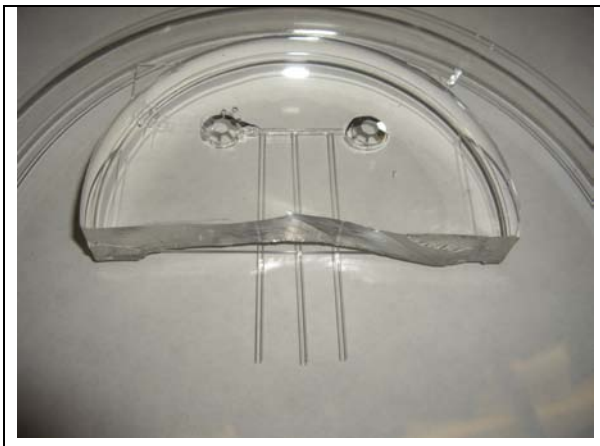

Figure 2.4: The complete assembly using the mold from Figure 2.3. The channel between the two reservoirs does not contain a glass capillary [2].

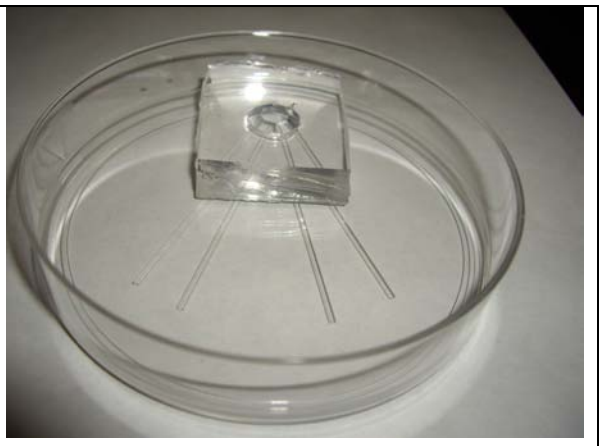

Figure 2.5: An example of a fully assembled device where a single inlet port fed four capillaries [2].

The following sections describe further specifics about the fluorescent indicators, types of cell culture and cell scoring techniques used to demonstrate this method. This chapter is then concluded with a summary of results.

2.1.2 Fluorescent indicators

The pumping action of the loading reservoir was used to load LIVE/DEAD fluorescent cell viability indicator and BCECF fluorescent intracellular pH indicator into the capillaries. LIVE/DEAD® BacLight™ (L13152, Invitrogen) was used to stain the HeLa cells. All preparations followed the standard procedure in the product manual. A pH-sensitive ratiometric fluorescent indicator (BCECF AM, Invirogen) was used to visualize the pH gradient resulting from oxygen diffusion limitations. A BCECF solution was prepared according to the manufacturer's instructions for adherent cells and then loaded via Hank's Buffered Salt Solution (HBSS) into the capillaries after general cell growth media (GM) was removed. After a loading period of 30 minutes, cells were

imaged using an inverted fluorescent microscope (Nikon Eclipse E600FN microscope with a Media Cybernetics Evolution MP 5.1 Mega-pixel Digital CCD Color Camera). Fluorescent intensity ratios from BCECF were calibrated according to previously published results [11].

2.1.3 HeLa cell culture

HeLa cells (ATCC, Manassas, VA) were maintained in culture dishes in growth medium (GM: 90% DMEM, 10% FBS) in an incubator with atmosphere of 21% O_2 and 5% CO_2 at 36.6 ^{0}C. To take cells from plates, 1.5mL of trypsin was added for 60 seconds and then aspirated from the plate; this process detached cells from the plate surface and allowed for collection. The detached cells were centrifuged for 5 minutes at 3000 RPM, followed by removal of supernatant and re-suspension in 0.25 to 0.5 mL of fresh GM. Capillaries were loaded with this highly concentrated cell suspension.

2.1.4 C2C12 cell culture

C2C12 cells were handled and maintained in exactly the same conditions as HeLa cells with the exception of growth medium (C2C12 GM: 80% DMEM, 20% FBS) and differentiation medium (C2C12 DM: 92.5% DMEM, 7.5% FBS). C2C12 cells were loaded in C2C12 GM into the capillaries; C2C12 GM was replaced with C2C12 DM approximately 24 hours after seeding when cell viability gradients could be observed via cell morphology.

2.1.5 Cell Scoring and Data Processing

HeLa cells were scored as live and attached if they exhibited green fluorescence and appeared to be spread out on the capillary surface. In total, the results from ten 100μm by 1000μm, nine 50μm by 500μm and four 30μm by 300μm capillaries were analyzed (more experiments were performed but the results were similar and scoring was labor intensive). To count the attached cells, a micrograph of each capillary was overlaid with a rectangular grid in digital format. The cells from each rectangle were then scored and counted from a computer screen. Capillary data was normalized by shifting the point of the highest rate of attached cell increase so that the initial front of cells lined up.

2.1.6 3D Experiments

HeLa cells were also loaded and cultured in Matrigel (Becton Dickinson, Franklin Lakes, NJ) and 3D Collagen Culture Kit (Millipore, Billerica, MA). Cells were loaded in the appropriate suspension (as above) and the gel-cell suspension was allowed to solidify inside the 5% CO2, 37°C incubator (as per manufacturer's instructions). All other steps were carried out as above.

2.2 Device Operation and Results

Because of the capillaries' sizes, diffusion and not convection dominates mass transfer into the capillaries (Figure 2.2 e,f). During culture, mass transfer oxygen microgradients were generated within 0.5–3mm of the capillary edge. With HeLa cells, observable cell morphological gradients formed 12-24 hours after seeding. This method lent itself to high-throughput experimentation; as many as 30 capillary experiments were run in a 24-hour period including cell loading, gradient formation and imaging. The

method resulted in an approximately 50% yield (out of approximately 100 samples run) from the cell loading to imaging stage; most failures (approximately 40 out of 100 experiments) were due to incomplete loading of cell suspension (Figure 2.6).

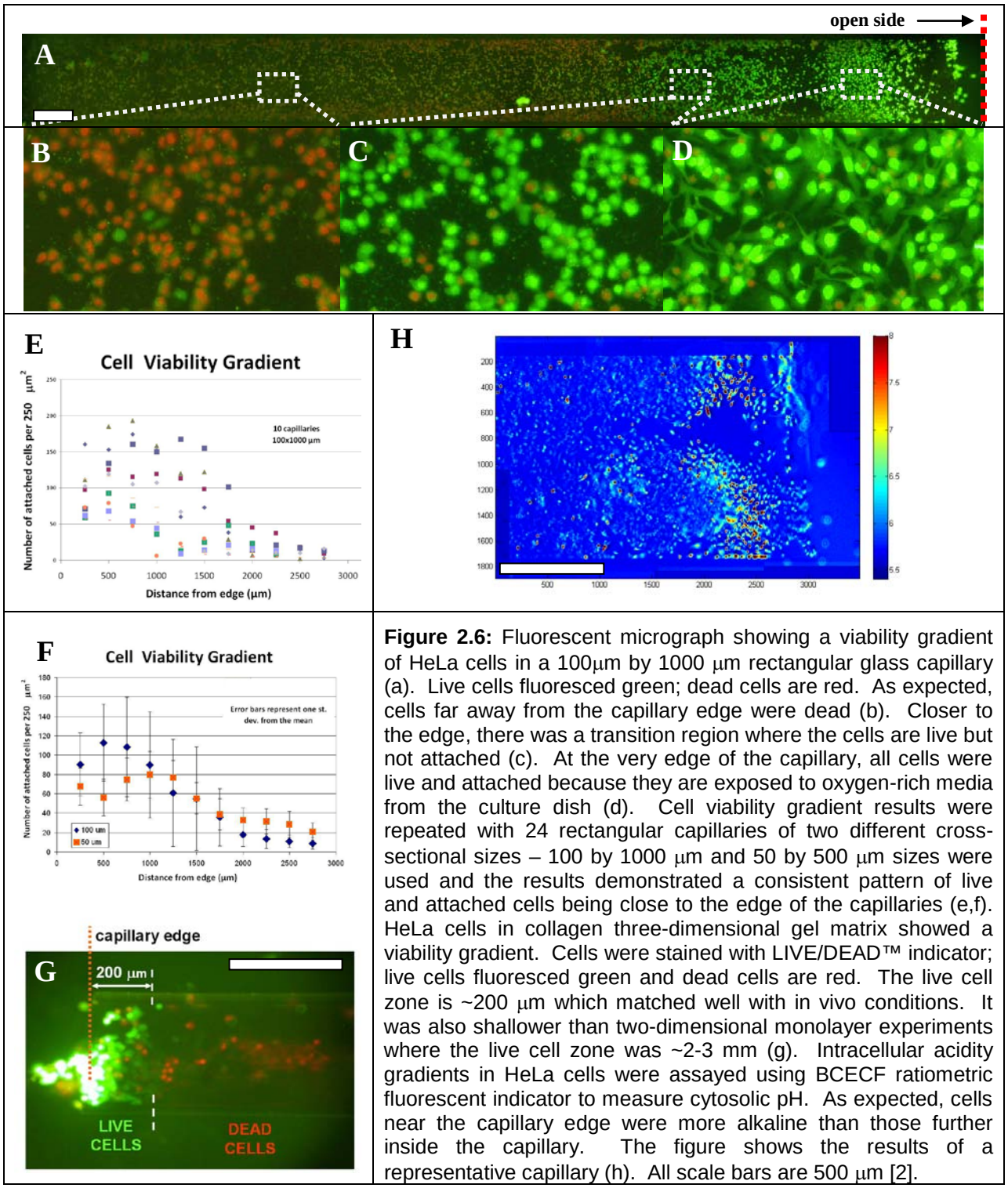

Figure 2.6: Fluorescent micrograph showing a viability gradient of HeLa cells in a 100μm by 1000 μm rectangular glass capillary (a). Live cells fluoresced green; dead cells are red. As expected, cells far away from the capillary edge were dead (b). Closer to the edge, there was a transition region where the cells are live but not attached (c). At the very edge of the capillary, all cells were live and attached because they are exposed to oxygen-rich media from the culture dish (d). Cell viability gradient results were repeated with 24 rectangular capillaries of two different cross-sectional sizes – 100 by 1000 μm and 50 by 500 μm sizes were used and the results demonstrated a consistent pattern of live and attached cells being close to the edge of the capillaries (e,f). HeLa cells in collagen three-dimensional gel matrix showed a viability gradient. Cells were stained with LIVE/DEAD™ indicator; live cells fluoresced green and dead cells are red. The live cell zone is ~200 μm which matched well with in vivo conditions. It was also shallower than two-dimensional monolayer experiments where the live cell zone was ~2-3 mm (g). Intracellular acidity gradients in HeLa cells were assayed using BCECF ratiometric fluorescent indicator to measure cytosolic pH. As expected, cells near the capillary edge were more alkaline than those further inside the capillary. The figure shows the results of a representative capillary (h). All scale bars are 500 μm [2].

Once cells were loaded into this system, simple finger pumping (Figure 2.2 g,h) allowed for rapid introduction of reagents with low shear without resorting to diffusion [1], pumping devices [5] or membrane-driven loading [12]; cells stayed attached to the capllary walls and did not move during pumping. In this work, cell viability was assayed with a LIVE/DEAD™ kit (Invitrogen, Carlsbad, California) loaded via the finger pump once cell morphological gradients were observed in the capillaries (Figure 2.6). This assay is composed of two nucleic acid-binding stains – SYTO 9™ and propidium iodide. SYTO 9™ penetrated all cellular membranes and stained the cells green, while propidium iodide only penetrated cells with damaged membranes. The combination of the two stains resulted in red fluorescence of the dead cells; live cells fluoresced green. Three zones of viability were observed in a graded fashion from the capillaries' open end: live, attached, cells were closest to the open end, followed by live, unattached cells, followed by dead, apoptotic, unattached cells filling the remaining length of the capillary (Figure 2.6 a,b,c,d). By employing different diameter capillaries, the depth of the cell viability gradient could be controlled (Figure 2.6 e,f). This method also worked well for three-dimensional matrix cultures loaded into the capillary; viability gradients developed in 50µm (inside height dimension) capillaries loaded with HeLa cells in a collagen gel matrix (Figure 2.6 g). However, after initial attachment within either collagen or Matrigel™ loaded capillaries, cells did not divide and became apoptotic after 72 hours.

Experiments were conducted with capillaries of three different sizes with the following cross-sectional dimensions of inside cavity: 30µm by 300µm, 50µm by 500µm, and 100µm by 1000µm (Figure 2.6b).

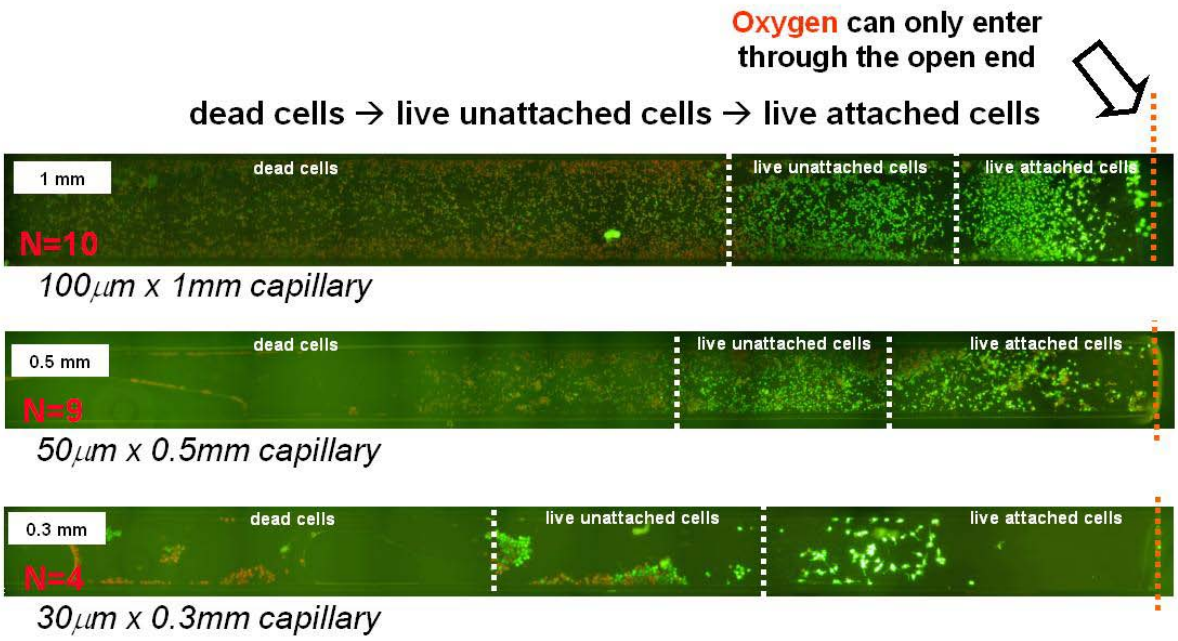

Figure 2.6b: Experiments were conducted in capillary channels of various cross-sectional dimensions of inside cavity: 30µm by 300µm (bottom), 50µm by 500µm (middle), and 100µm by 1000µm (top). Notably, most of the capillary channels exhibited an "edge effect" where there seemed to be more dead cells near the capillary edges; this could be caused by the buildup of chemicals during fabrication in the channel corners and cellular waste products due to diffusion limitations during experiments. The "edge effect" is especially well seen in 100µm by 1000µm capillaries (top).

Smaller sized capillaries suffered from poor yields due to cell clumping as well as lower control during filling and pumping. Capillaries with cross-sectional areas of 100µm by 1000µm were found to be the most optimal and yield efficient in the experiments that were conducted (Figure 2.6b).

It was expected that the low oxygen environment within the capillary would promote anaerobic respiration and lead to acidification, and therefore generate a pH gradient along the axis of the capillary. To test this hypothesis, BCECF, a ratiometric pH indicator (Invitrogen, Carlsbad, California), was used. Using the assay loading technique, cells were loaded with BCECF and a ratiometric intensity gradient was subsequently observed (Figure 2.6 h).

This gradient generation and loading method was also used to induce differentiation

in C2C12 muscle precursor cells. This cell line has been shown to have a differentiation dependence on oxygen conditions and normally requires a change in cell medium components to trigger differentiation in culture [8, 9, 10]. To test if differentiation was affected by the gradient, C2C12 cells were seeded into the capillaries using our method, and then allowed to proliferate in growth medium for 24 hours. Differentiation medium was then added using our loading technique and cells were observed for 7 days. Myotube formation was observed in oxygen rich zones near the capillary edge and lack of myotube formation further in the capillary (Figure 2.7). As differentiation progressed, strongly differentiating areas delaminated from the capillary into spherical clumps.

The presented method is particularly useful for quickly and reliably generating many replicates of mass transfer gradients in adherent cell cultures. It is readily interfaced with the PDMS-based microfluidic systems in widespread use for downstream analysis and reagent delivery. It is particularly attractive for experiments where an exogenous chemical gradient is to be superimposed along an axis perpendicular to the mass transfer gradient (Figures 2.2 i). Additionally, the system can be used to load time-sensitive reagents (such as LIVE/DEAD™ or BCECF) without any other microfluidics using the finger pumping technique. This method can be extended to studies of gradients in three dimensional cell/gel suspensions. Finally, the method can be used to study self-adherent cell constructs such as those used in tumor spheroid models.

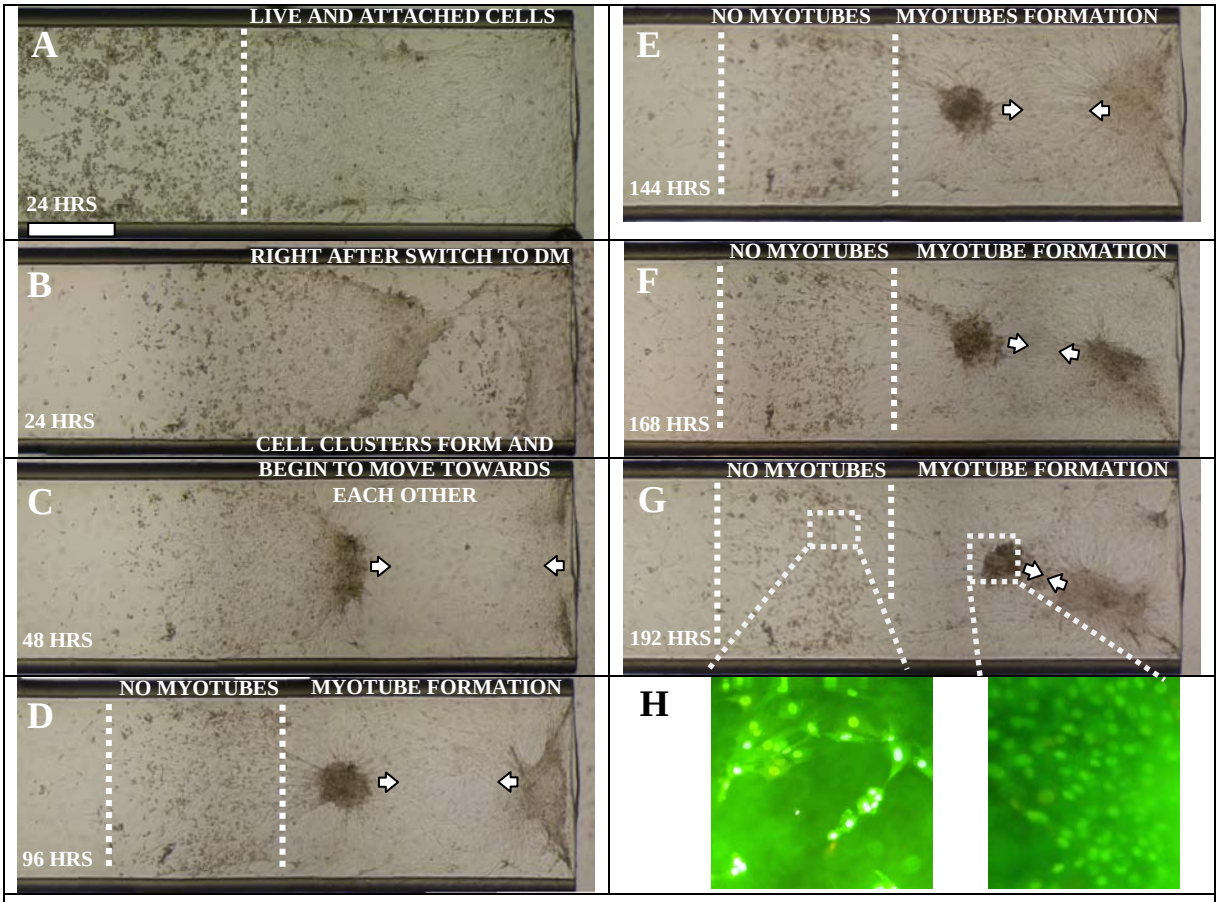

Figure 2.7: Time course of C2C12 myoblasts; a C2C12 viability gradient was first formed during a 24 hour period with live attaching near the capillary edge **(a)**. GM was then replaced with DM **(b)** and the cells were incubated for an additional 168 hours for an overall total of 192 hours after seeding **(c, d, e, f, g)**. Myotubes became visible at 72 hours **(d)**; they never formed in the hypoxic region away from the edge. Fibers formed three dimensional "clumps" which migrated towards each other after 24 hours in DM **(c, d, e, f, g)**. LIVE/DEAD assay also indicated the formation of the myotubes in the normoxic region near the capillary edge **(h)**. Indicated times were measured from the time of cell loading into the capillary. All scale bars are 500 μm; capillary is 1000 μm wide. Experiment was conducted in three separate capillaries with similar results [2].

This chapter described a new method that overcomes most of the limitations encountered with state-of-the-art oxygen microgradient generation techniques as described in Table 1.1. However, more work was needed to fully characterize this method. In particular, measuring oxygen directly is very important and is the only way to link the results presented in this chapter with a predictive model of cell survival and

gradient generation based on mass transfer and cellular metabolism. Thus, it was necessary to expand the method to be able to take direct oxygen measurements and this is the topic of the next chapter.

Chapter 2 References

1. R. Venkatasubramanian, M.A. Henson & N.S. Forbes, “Incorporating Energy Metabolism into a Growth Model of Multicellular Tumor Spheriods,” Journal *of Theoretical Biology* 242, 440-453, 2006.
2. M. Pinelis, L. Shamban, A. Jovic & M.M. Maharbiz, "A high-yield method for generating mass-transfer gradients in elastomer microfluidics using impermeable capillaries," *Biomedical Microdevices* 10(6), 807-11, 2008.
3. T. Bansal, M.P. Chang & M.M. Maharbiz, "A class of low voltage, PDMS-gold 'wet' actuators for use in high-density microfluidics," *Lab Chip* 7, 164-166, 2007.
4. M. Pinelis, R.W. Kasinskas, R.T. Borno, J. Park, E. Chu, N.S. Forbes & M.M. Maharbiz, "Microfluidics devices for the assembly and culture of three-dimensional multi-cellular constructs with diffusion-limited microenvironments," *Tenth International Conference on Miniaturized Systems for Chemistry and Life Sciences (MicroTAS)*, Tokyo, Japan, November 2006.
5. S. Takayama *et al*., “Patterning cells and their environments using multiple laminar fluid flows in capillary networks,” *PNAS* 96, 5545-5548, 1999.
6. J.H. Park, T. Bansal, B.H. Chueh, S. Takayama & M.M. Maharbiz, “Electrolytic Patterning of Dissolved Oxygen Microgradients During Cell Culture”, *The 18th IEEE International Conference on Micro Electro Mechanical Systems,* Miami, 2005.
7. G. Helmlinger, A. Schell, M. Dellian, N.S. Forbes & R.K. Jain, “Acid Production in Glycolysis-Impaired Tumors Provides New Insights into Tumor Metabolism,” *Clinical Cancer Research* 8, 1284-1291, 2002.
8. M. Csete, *Anesth Clin N Am* 16, 201-10, 1998.
9. X. Li, L.L. Zhu, X.P. Chen & M. Fan, “Effects of hypoxia on proliferation and differentiation of myoblasts,” *Medical Hypotheses* 69, 629-636, 2007.
10. Z. Yun, Q. Lin, & A.J. Giaccia, “Adaptive Myogenesis under Hypoxia,” *Molecular and Cellular Biology* 25, 3040-3055, 2005.
11. I.D. Weiner & L.L. Hamm, “Use of fluorescent dye BCECF to measure intracellular pH in cortical collecting tubule,” *Renal Physiology* 256, 957-964, 1989.
12. B.H. Chueh *et al*., “Leakage-free bonding of porous membranes into layered microfluidic array systems,” *Analytical Chemistry* 79, 3504-3508, 2007.

CHAPTER 3

OXYGEN MEASUREMENTS

As described in Chapter 2, the method was successfully demonstrated with oxygen micro gradients producing cell viability, pH and differentiation gradients, and further work was needed to more completely characterize this method. In particular, it was necessary to:

- Directly measure oxygen in the capillaries (described in this chapter)
- Develop a mathematical model to relate the measurements of oxygen, pH and cell viability (described in Chapter 4)

This chapter outlines the available techniques for measuring oxygen and the experimental work that was done.

3.1 Direct Oxygen Measurements

Oxygen in aqueous media can be measured electrochemically (EC) or optically. The table below compares the main methods that currently exist:

Method	Type	Pros	Cons
Clark sensor	EC	* well established method [9,11,12] * can measure *in vivo* within tissues [12] * no need for fluorescent chemicals in cell media [9,11]	* invasive [9,12] * consumes oxygen [9,10,11,12] * biofouling [12] * requires specific electrolyte solutions [11,12] * temperature dependent [10,12] * difficult to miniaturize [10,11]
ISFET	EC	* based on MOSFETs [13,14,17] * can measure *in vivo* within tissues [13,16] * no need for fluorescent chemicals in cell media [13,14]	* invasive [13,16,17] * biofouling [14,15,16] * requires specific electrolyte solutions [13,14,15] * temperature dependent [13,17] * drift and calibration [14] * not biocompatible [13,15,16] * difficult to miniaturize [16,17]
Fluorescence quenching	Optical	* minimally invasive [18,19,21] * does not consume oxygen [18,19,20,21] * biocompatible [18,19,20]	* complicated measurements [18,21] * not suitable for portable applications [18,21]

Table 3.1: Comparison of direct oxygen measurement methods.

As described in the table above, there are two main types of methods to measure dissolved oxygen – electrochemical, such as the Clark sensor and ISFETs, and optical, such as fluorescence quenching. Although further details are provided below for how the electrochemical methods work, miniaturization of devices that utilize these methods has been difficult; decreasing dimensions in sensor electrodes inevitably result in lowered signal-to-noise ratios as the amount of measured signal is generally directly proportional to the surface area of the working electrodes [1,9,11,12,17,22].

In the next few sections, the methods presented in Table 3.1 above are described in detail.

3.2 Clark Sensor

The Clark sensor was first developed by Leland C. Clark in the 1950s. The sensor is based on two electrodes immersed in an appropriate electrolyte solution. One electrode,

usually made from metals such as platinum or gold, is coated with an organic thin film through which dissolved oxygen can diffuse at a rate that is significantly higher than other chemicals present in the electrolyte solution. Once dissolved oxygen reaches the electrode it is reduced via the following chemical reaction:

$$O_2 + H_2O + 4e^- \rightarrow 4OH^-$$

The other electrode, usually Ag/AgCl, absorbs electrons from ions in the electrolyte solution as follows:

$$Ag + Cl^- \rightarrow AgCl + e^-$$

The electrodes are connected together and biased with an appropriate voltage – usually ~0.7 volts; this voltage has been shown to be high enough to drive the reduction of oxygen at the cathode, while not being so large as to cause other reactions at the electrodes. The resulting current then corresponds to the amount of dissolved oxygen (Figure 3.1).

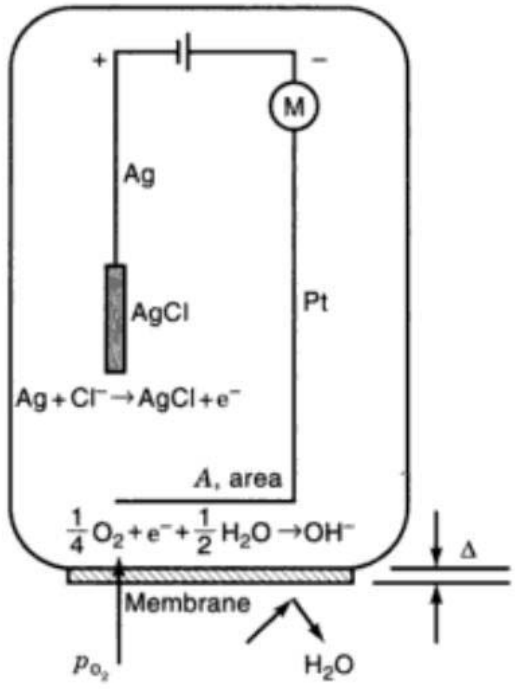

Figure 3.1: Clark sensor structure and operation [3].

This method has a number of limitations because:

1) it is invasive; in other words, at least one of the electrodes needs to be in the same chamber as the live cell culture and, thus, could interfere with the effects of the oxygen micro gradient during experiments [9,10]
2) it consumes oxygen; since oxygen is reduced at the cathode, it is actually consumed and, therefore, especially with the minute volumes used in this method would directly affect the shape of the oxygen micro gradient [9,10,11,12]
3) it is prone to be affected by biofouling, since the measurements are dependent on oxygen passively diffusing through the membrane; thus, the stability of the sensor is affected [12]
4) it requires specific electrolyte solution which is compatible with the well-characterized electrodes such as a platinum cathode and Ag/AgCl anode [9,10]
5) it is temperature dependent, because the rate of oxygen diffusion will vary with temperature [9,10]

In addition to the limitations outlined above, this method also presents additional challenges with its integration into a micron-scale resolution architecture that is compatible with MEMS processes [22]. Other concerns would include placing the sensors and readout circuitry into the capillaries.

3.3 ISFET

ISFETs suffer from similar disadvantages of the Clark sensors and are also are limited by drift and calibration problems [13,14]. ISFETs are based on the MOSFET structure as shown in Figure 3.2 below.

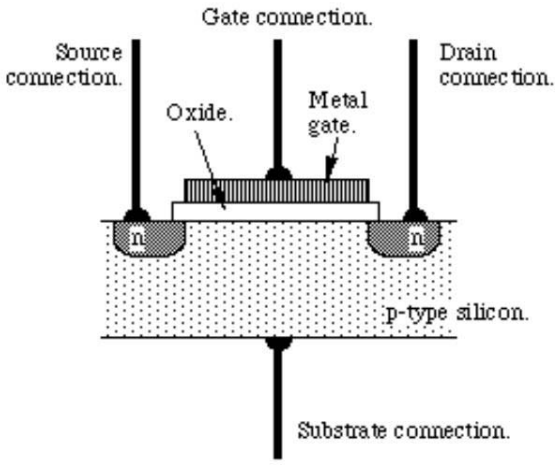

Figure 3.2 MOSFET structure and operation [2].

In a MOSFET, the gate is biased with an appropriate voltage that attracts charges to the substrate surface and therefore creates a channel for the electric current to flow between the source and the drain (Figure 3.2).

An ion selective field effect transistor, or ISFET, operates similarly to the traditional MOSFET. However, in an ISFET, the MOSFET's gate electrode is replaced with a detached "reference" electrode. Here, when voltage is applied between the reference electrode and the substrate, reactive species in the solution, such as dissolved oxygen, interact with the ion selective membrane and produce ions that then cause a voltage drop between the substrate and the gate insulator surface (Figure 3.3; the gate insulator is oxide in this case).

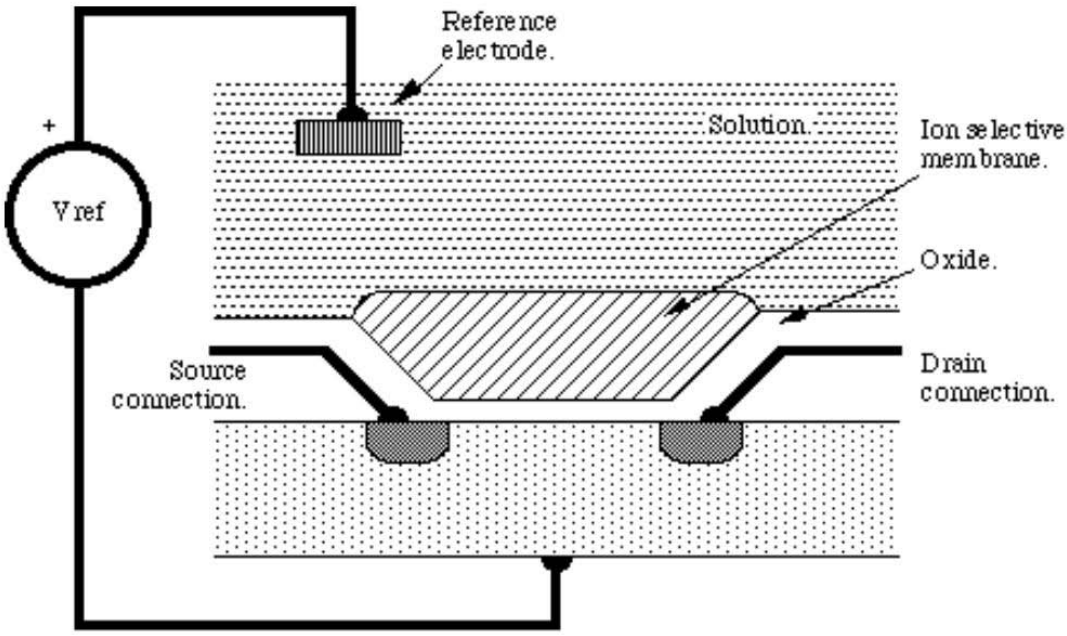

Figure 3.3 ISFET structure and operation [2].

The reference electrode is usually adjusted to maintain the current between the source and the drain stable. The concentration of the charged particles in the solution then determines the amount of ions that penetrate into the ion selective membrane which, in turn, drives the changes in the impedance between the source and the drain; the required voltage to keep the current constant is measured and then related back to the presumed ion concentration. The main problem with the ISFET approach is that there are many potential challenges with the membrane such as those related to adhesion, selectivity, sensitivity, hysteresis and others [13,15,16,17].

3.4 Fluorescence Quenching

In this method, a fluorescent indicator is dissolved in an aqueous medium and then excited with light at a specific frequency (Figure 3.4). The indicator then fluoresces at another specific frequency and this signal is detected by a photosensitive diode.

Fluorophores are also embedded in sol-gel preparations [23,24,25], membranes [26,27] as well as, increasingly, quantum dots [28,29,30].

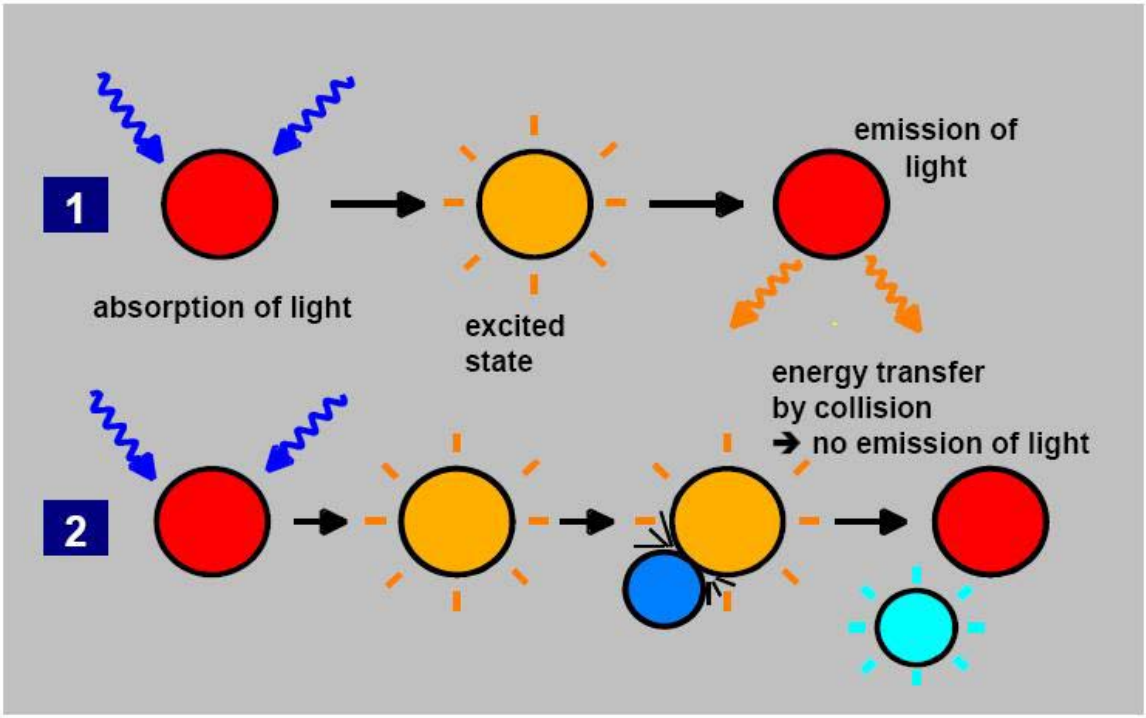

Figure 3.4 Principle of dynamic quenching of luminescence by molecular oxygen: (1) luminescence process in the absence of oxygen, (2) deactivation of the luminescent indicator molecule by molecular oxygen [7].

The principle is described by the Stern-Volmer equation:

$$I_0/I = 1 + K_{SV}[0_2] ,$$

where I and I_0 are the fluorescence intensities with and without oxygen present, K_{SV} the Stern-Volmer quenching constant and $[O_2]$ the concentration of dissolved oxygen. More accurate versions of this technique were recently demonstrated where differences in the *time decay* of the fluorescent signal were shown to be proportional to the amount of dissolved oxygen. This type of measurement is called fluorescence lifetime imaging, or FLIM, and there are two FLIM methods as described in the figure below: the time-domain method and the frequency-domain method (Figure 3.4b).

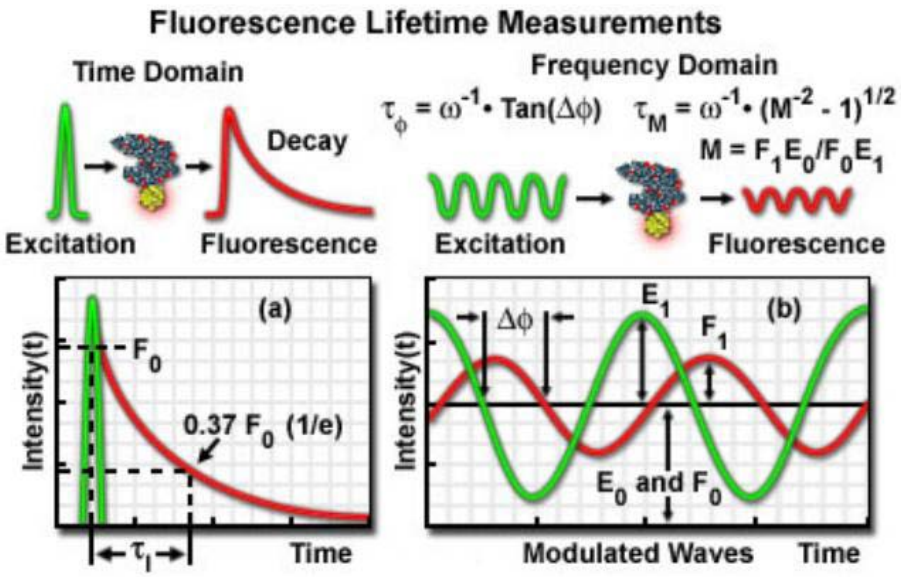

Figure 3.4b The principles of FLIM measurements in time and frequency domain [4].

Unlike the electrochemical methods, optical FLIM techniques are desirable for cell culture measurements because they are minimally invasive, suitable for small volumes and do not consume oxygen during measurements.

In particular, FLIM measurements were recently used to evaluate levels of dissolved oxygen in live cell culture microenvironments [5]. In this work, ruthenium tris(2,2'-dipyridyl) dichloride hexahydrate (RTDP) fluorescent indicator and time domain measurements were used. These measurements showed that oxygen levels could be measured with axial resolution of 1-2μm and lifetime discrimination of ~50ps.

3.5 Experimental Overview for Oxygen Measurements

As described earlier in this chapter, it was desirable to more fully characterize the method with direct oxygen measurements. Furthermore, optical methods, such as fluorescence quenching, were determined to be most suitable for cell culture applications.

Thus, a series of experiments were conducted to measure oxygen in the capillary channels in two phases:

- Phase 1: The FLIM method was evaluated to identify the most appropriate measurement technique that met the following criteria:
    - Spatial resolution of at least 1mm
    - Oxygen resolution of at least 0.1% dissolved oxygen
- Phase 2: Once the oxygen measurement technique was established, oxygen level measurements were taken in 5 separate channel capillaries. For each capillary, oxygen level was be measured from the open edge of the capillary and along the capillary's main axis in 1 mm intervals for a total of 10 such measurements per capillary. In other words, oxygen levels were measured for a total of 10 mm from a capillary's open end. Initial cell seeding density in each capillary was recorded and then used as one of the inputs to the model described in Chapter 4.

3.6 Chip Design and Fabrication

The chip layout and design closely mirrored the features of the prototype devices introduced and tested as described in Chapter 2. Specifically, this first-generation design included a central reservoir and three channels as shown in Figure 3.5 below.

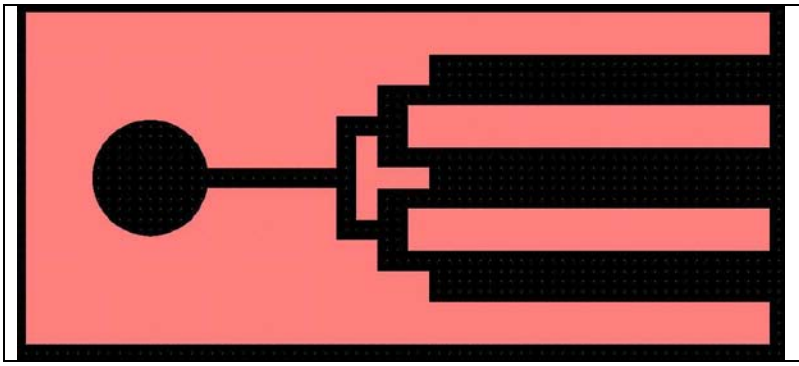

Figure 3.5: Chip design and layout. The batch-fabricated chip included a central reservoir for loading cells and reagents as well as three channels for culturing cells and making oxygen measurements. The overall chip has dimensions of 18 mm by 38 mm. Channels were 2.5 mm and 3 mm in width. The height of the channels was 300 μm.

To fabricate the chip, a series of possible processes were evaluated and, specifically, various bonding methods were considered including anodic silicon to glass bonding, direct glass to glass bonding as well as SU-8 bonding. It was determined that, given the available equipment and chip design requirements, the SU-8 bonding method was the most appropriate for the fabrication process as described in Figure 3.6 below. Other bonding alternatives were also explored including anodic and glass-to-glass fusion bonding. Anodic bonding required more processing steps than SU-8 bonding and the height of the channels would be constrained to the thickness of the silicon wafer. Additionally, this process would require a lengthy etch step for silicon. Glass-to-glass fusion bonding was a desirable alternative, but there was no appropriate equipment available for this process. Attempts were made to outsource the process to commercial foundries such as Micronit (Enschede, the Netherlands).

For the SU-8 fabrication process, a 500 μm thick glass wafer was first spin coated with 300 μm layer of SU-8, exposed and developed with a standard SU-8 process (Microchem, Newton, Massachusetts). Strips of oxygen sensitive film (PreSens, Regensburg, Germany) were then attached to the bottom of the channels with a silicone adhesive (PreSens, Regensburg, Germany). After this, a fresh glass wafer was spin coated with a thin 50 μm layer of SU-8 and the main device with channels was inverted and dipped into the this thin SU-8 layer; it was then lifted and attached to a fresh and cleaned rectangular glass slide. The overall structure was then heated to 95^0C and bonded by UV exposure for 1 minute in the SUSS MA6 Mask Aligner (SUSS Microtec, Waterbury, Vermont) with an applied pressure of ~ 5-10 psi (Figure 3.6).

One of the main problems with this fabrication process is that many of the channels would leak due to the poor bond between the SU-8 and glass. There is also an expect ratio limit of ~0.5 for the channels due to the overflow on SU-8 during the bonding process. Discussion on improving on these limitations is included in Chapter 5.

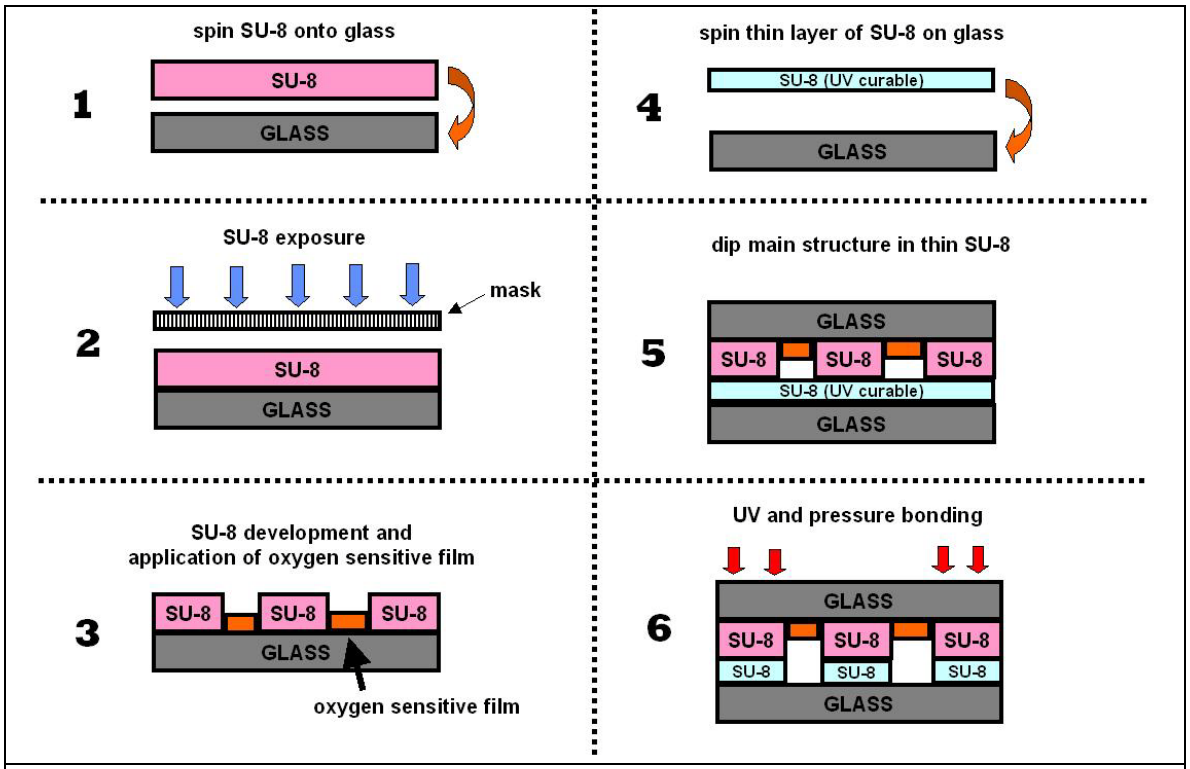

Figure 3.6: Chip fabrication process included the following steps: (1) a thick, 300 µm layer of SU-8 was spun on to a glass wafer, (2) SU-8 was exposed, (3) SU-8 was developed and oxygen sensitive film was attached to the glass substrate using silicone adhesive, (4) a thin, 50 µm layer was spun onto a glass slide, (5) the main structure with channels that was formed in step 3 was dipped into the thin layer of SU-8 and (6) resulting structure was bonded to a clean glass slide.

After the chip was fabricated a fluidic connector made from PDMS and plastic tubing was attached to the chip's central reservoir (Figure 3.7).

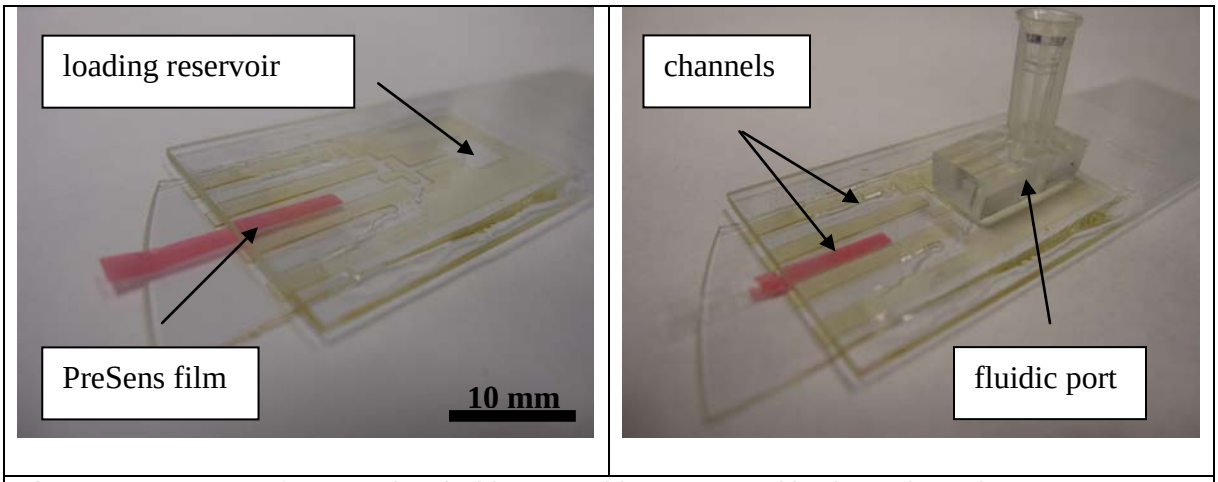

Figure 3.7 Images of a completed chip assembly. Image with channels and PreSens oxygen sensitive film (left) and the same chip with a microfluidic connector (right).

3.7 Cell Loading and Culture

C2C12 cells were used in these experiments – they are relatively robust and also have been shown to differentiate in presence of oxygen microgradients [8].

For cell culture, C2C12 cells (ATCC, Manassas, VA) were initially grown in culture dishes in growth medium (GM: 90% DMEM, 10% FBS) in an incubator with atmosphere of 21% O_2 and 5% CO_2 at 36.6^0C. To take cells from plates, 1.5 mL of trypsin was added for 60 seconds and then aspirated from the plate; this process detached cells from the plate surface and allowed for collection. The detached cells were centrifuged for 3 minutes at 3000 RPM, followed by removal of supernatant and re-suspension in 0.25 to 0.5 mL of fresh general cell growth media (GM). Chips were then loaded with this highly concentrated cell suspension as described above.

In these experiments, cells in suspension were loaded into a chip's glass channels by capillary action capillary action through the open ends of channels. Alternatively, cells can also be loaded into the channels through the central reservoir via a fluidic connection port as shown in Figure 3.9 below.

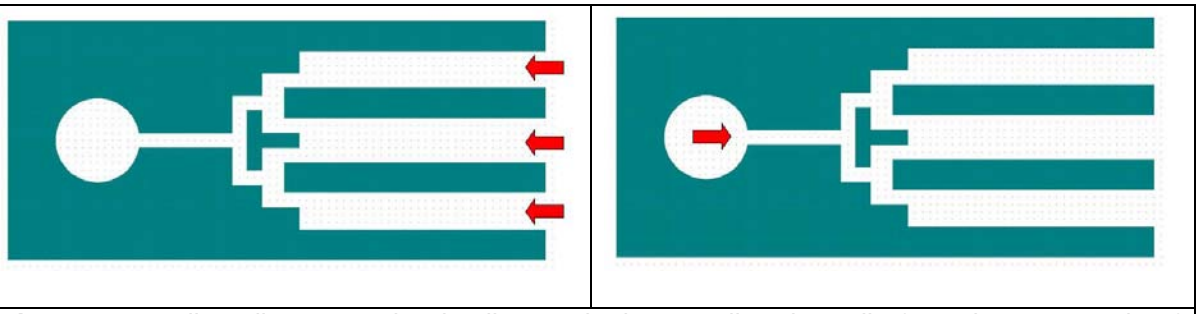

Figure 3.9: Cell-media suspension loading methods. Loading the cells from the open ends of capillary channels (left) and loading the cells from the central reservoir (right).

The reservoir can also be used as a way to deliver chemical reagents and indicators such as the LIVE/DEAD cell viability and pH fluorescent indicators into the chip similarly to what was demonstrated with the initial prototype device and as was described in Chapter 2.

3.8 Calibration Protocol

Calibration of the Fibox 3 fiber-optic oxygen meter was performed as per the manufacturer's instructions (PreSens, Regensburg, Germany) [7].

To prepare oxygen-free calibration solution, 1 g sodium sulfite (Na_2SO_3) was added to a glass bottle and dissolved 100 mL water. The water was then oxygen-free due to a chemical reaction of oxygen with Na_2SO_3. Additional oxygen that diffused from air into the water was removed by surplus of Na_2SO_3. The glass bottle was then closed with a screw top and shaken for approximately one minute to dissolve Na_2SO_3 and to ensure that the water is oxygen-free. The bottle was kept closed with the screw top after calibration to minimize oxygen contamination.

To prepare the air-saturated water calibration solution, 100 mL of DI water was added to a glass bottle, and air was blown into the water using plastic tubing and an air pump

while the bottle was stirred. After 20 minutes, the air pump was switched off and water in the bottle was stirred for a further 10 minutes to ensure that the water was not supersaturated.

After the calibration solutions were prepared, Fibox 3 fiber-optic oxygen meter was calibrated as per manufacturer's instructions (PreSens, Regensburg, Germany) as follows: Fibox 3 meter was connected via the RS232 cable to a PC computer, the Fibox 3 meter was switched on and was the fiber optic probe was placed in contact with the oxygen sensitive film. Then, the Fibox 3 software was launched and the current atmospheric pressure (1 atm) and the temperature (20^0C) were entered as the calibration. Atmospheric pressure reference is needed to convert the oxygen unit % air-saturation into partial pressure units (hPa, Torr) or concentration units (mg/L, μmol/L). The fiber optic probe and the oxygen sensitive film were then placed into air-saturated water calibration solution. To minimize the response time, the solution was slightly stirred. The calibration solution had to completely cover the sensor foil. After about 3 minutes the phase angle stabilized (as per the manufacturer's instructions, the variation of the phase angle should be smaller than ± 0.05°), the current phase angle was stored to correspond to the calibrated value for the air-saturated water calibration solution.

To record the second calibration value, the fiber optic probe and oxygen sensitive film were placed in oxygen-free calibration solution and the solution was stirred to minimize the response time. The stirring was not vigorous to avoid contamination of this calibration solution with oxygen. After about 3 minutes the phase angle stabilized (as per the manufacturer's instructions, the variation of the phase angle should be smaller than ±

0.05°), the current phase angle was stored to correspond to the calibrated value for the air-saturated water calibration solution.

3.9 Oxygen Measurements

Cells were cultured in the chip's capillary channels for a 24-hour period after which cell viability gradients were observed in a manner similar to what was demonstrated in Chapter 2. At this stage, oxygen measurements were taken using the set up shown in Figure 3.10 below. In these measurements, the fiber optic probe (PreSens, Regensburg, Germany) was scanned along the length of each channel in 1 mm steps for a total of 10 mm from the open side of each channel (Figure 3.10). Oxygen measurements were taken by the FIBOX 3 fiber-optic oxygen meter (PreSens, Regensburg, Germany) and recorded by a connected desktop computer.

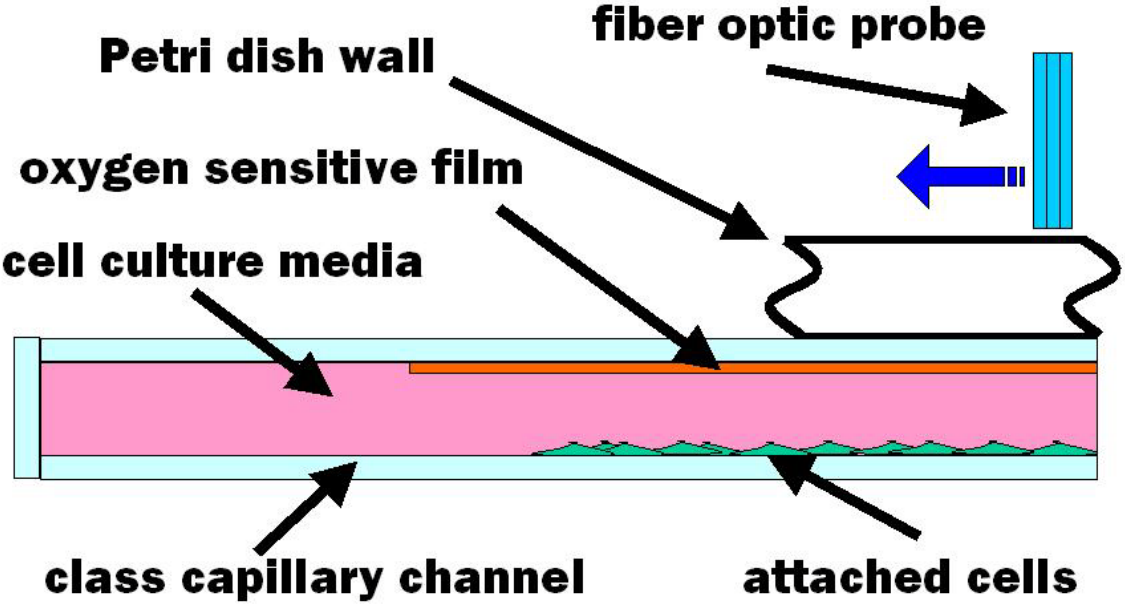

Figure 3.10: Experimental setup for taking direct oxygen measurements using the FLIM technique. Here the giber optic probed is scanned in 1 mm increments over the capillary channel in which an oxygen sensitive film resides. Shown components are not drawn to scale.

The fiber optic probe was set up to take measurements non-invasively to minimize the

risk of contamination (Figure 3.11).

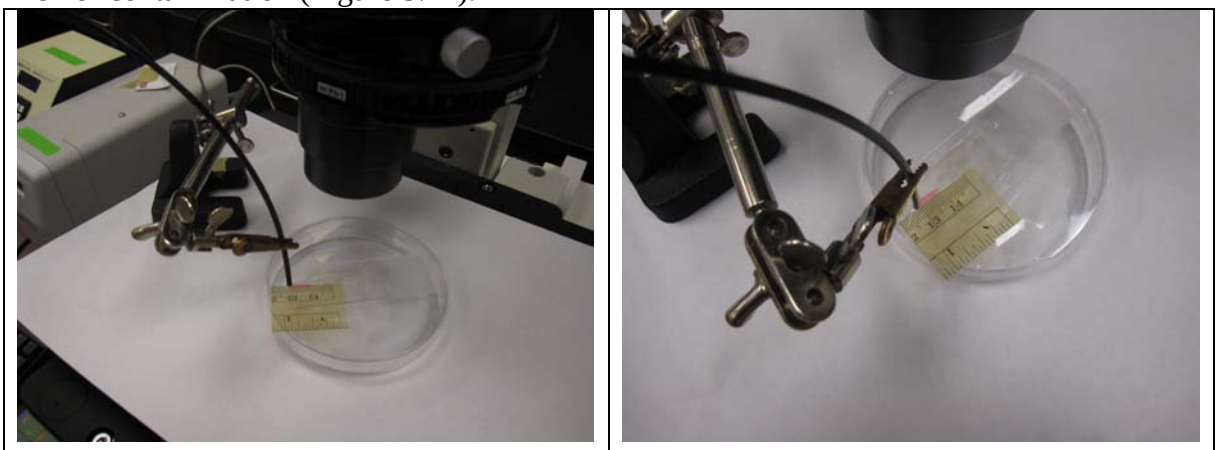

Figure 3.11 Oxygen measurement setup included the microscope and PreSens fiber optic probe (left). The chip was placed inside of a Petri dish to provide an outer shell to minimize the risk of contamination (right). A plastic ruler was used to keep track of the probe's position along the length of a channel.

C2C12 cells and the oxygen sensitive film are shown in a sample channel in Figure

3.12 below.

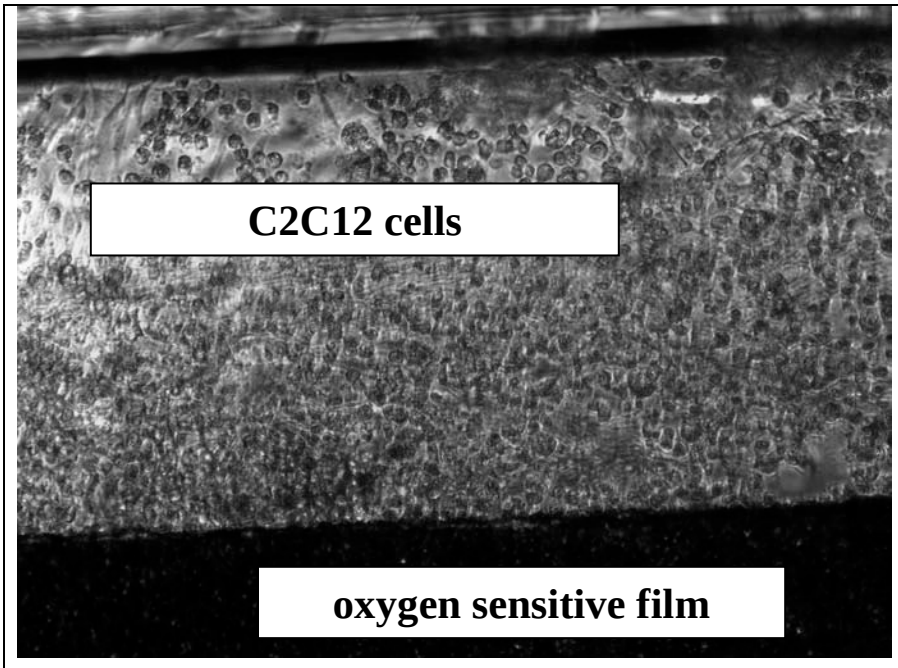

Figure 3.12: White light micrograph showing a section of a sample capillary channel with C2C12 cells growing in the same chamber as the PreSens oxygen sensitive film. Channel width was 3 mm and the width of the film was 2 mm. Channel height was 300 µm.

Images of a sample capillary channel are shown below in Figure 3.13.

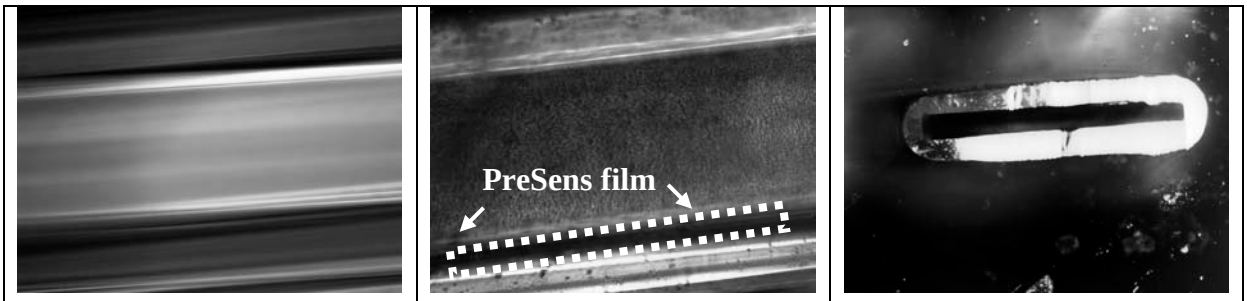

Figure 3.13: Side view of an empty capillary channel (left) and with cells and PreSens oxygen sensitive film (middle); cells cannot be seen in this channel sideview image. View from the open end of the capillary channel (right).

Raw data output is shown in Figure 3.14 below. Oxygen measurements were recorded as the probe was scanned along the length of a capillary channel. In this sample, the probe was scanned along the same channel three times (Figure 3.14).

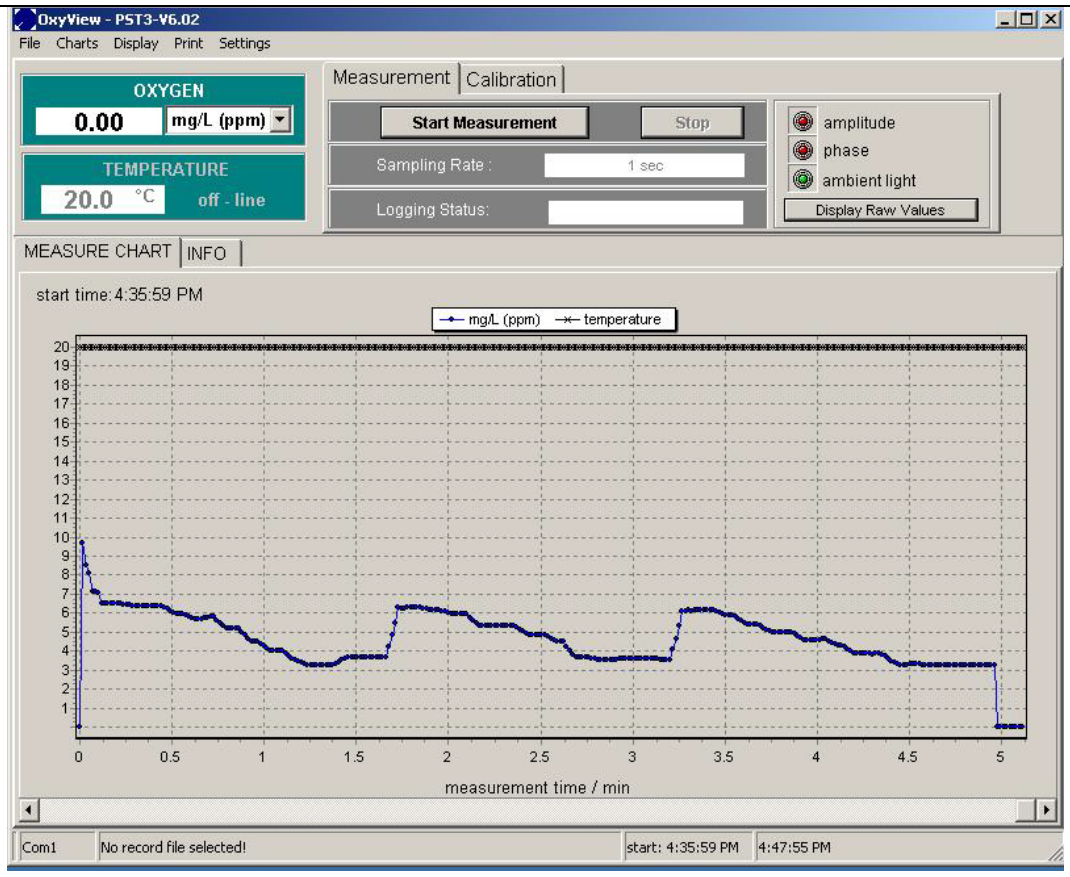

Figure 3.14: Sample oxygen measurement data. Here the measured data was taken at 1 mm intervals and recorded in mg/L or ppm (parts per million).

Using this method, direct oxygen measurements were taken in five capillary channels and this data is presented in Figure 3.15 below. Additional measured oxygen data is presented in Chapter 4. In the figure below, there is a considerable amount of variation between experiments. For example, dissolved oxygen drops faster in some capillary channels than others. The primary reason for this variation is due to the fact that cells grow in "clumps" and some capillaries are more evenly distributed than others. Thus, due to a non-homogeneous cell density, the amount of dissolved oxygen varies from one channel capillary to another. Notably, the level of dissolved oxygen in all 5 experiments is nearly identical at x=10mm; thus, even though the cells are not evenly distributed in different channels, the total number of cells in all channels is approximately the same. Also, the resolution of oxygen measurements is approximately 0.1 ppm and, therefore, the observed variations in Figure 3.15 are well below this resolution limit and the observed variation cannot be noise.

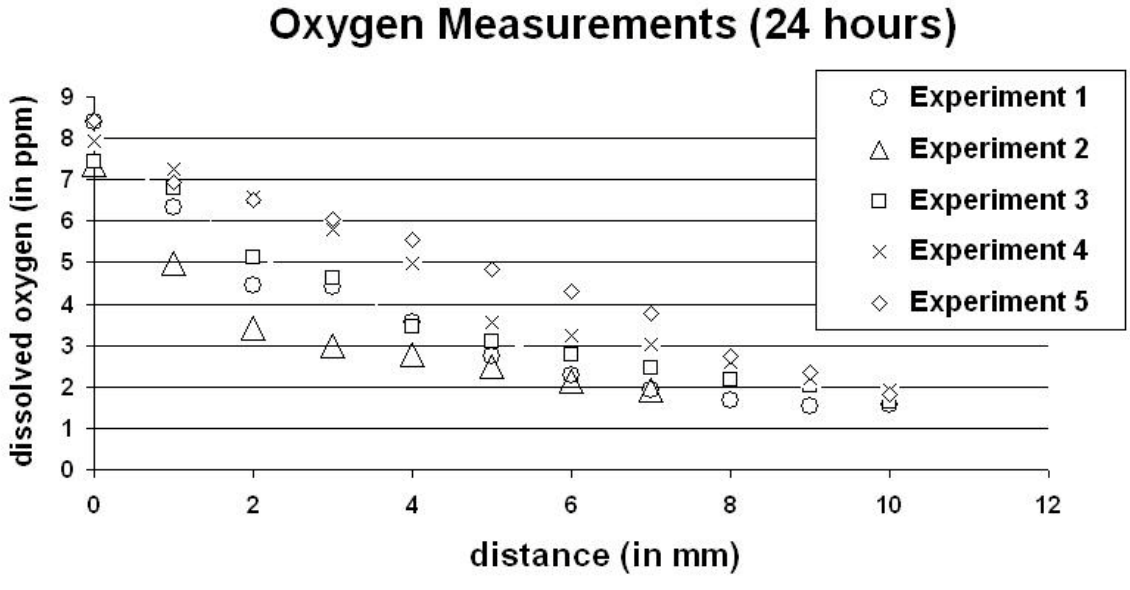

Figure 3.15: Dissolved oxygen (in ppm) vs. position (in mm) 24 hours after start of experiment. As expected, the amount of dissolved oxygen decreased as the probe was moved away from the open end of the capillary channel. Comparisons of this data to model predictions will be discussed in Chapter 4.

With the oxygen measurements completed, the dataset was used, along with cell viability and pH measurement data presented in Chapter 2 to develop a physical model that relate these data and confirm that the method in fact produces results that are consistent with the *in vivo* cell behavior. This model is presented in Chapter 4 along with comparisons to additional experimental results and measured data.

3.10 Summary

This chapter presented a comparison of viable oxygen measurement methods and outlined the considerations that make optical (vs. electrochemical) methods more suitable in this case. In addition, an experimental overview for oxygen measurements was presented.

As a result of experiments outlined in this chapter, the proposed method was more fully characterized by performing oxygen measurements. As the next step, a physical model was developed to relate the measured data on cell viability, pH, oxygen and density to confirm that the method produces results that are consistent with the *in vivo* behavior of cells under an oxygen tension. This is the subject of the next chapter.

Chapter 3 References

1. S.G. Weber, “Signal-to-noise ratio in microelectrode-array based electrochemical detectors,” *Anal. Chem.*, 61 (1989) 295-302.
2. Introduction to Microengineering: http://www.dbanks.demon.co.uk/ueng/chemsens.html
3. S.A. Dyer, Survey of Instrumentation and Measurement, Wiley-IEEE, 2001.
4. Reference: http://www.olympusfluoview.com/applications/flimintro.html
5. Mehta et al, “Quantitative measurement and control of oxygen levels in microfluidic poly(dimethylsiloxane) bioreactors during cell culture,” *Biomed Microdevices* 9:123–134, 2007.
6. T. Bansal, M.P. Chang, M. M. Maharbiz, "A class of low voltage, PDMS-gold 'wet' actuators for use in high-density microfluidics," *Lab Chip* 7, 164-166, 2007.
7. PreSens Instruction Manual, Fibox 3, Software Version 5.32, March 2006.
8. M. Pinelis, L. Shamban, A. Jovic & M.M. Maharbiz, "A high-yield method for generating mass-transfer gradients in elastomer microfluidics using impermeable capillaries," *Biomedical Microdevices* 10(6), 807-11, 2008.
9. M. Koudelka, "Performance characteristics of a planar ‘clark-type’ oxygen sensor," *Sensors and Actuators* 9, 249-258, 1986.
10. G. Jobst *et al*, "Thin-film Clark-type oxygen sensor based on novel polymer membrane systems for in vivo and biosensor applications," *Biosensors and Bioelectronics* 8, 123-128, 1993.
11. C. Wu *et al*, "Fabrication of miniature Clark oxygen sensor integrated with microstructure," *Sensors and Actuators B: Chemical* 110, 342-349, 2005.
12. M. Wittkampf *et al*, "Silicon thin film sensor for measurement of dissolved oxygen," *Sensors and Actuators B: Chemical* 43, 40-44, 1997.
13. B. Sohn *et al*, "A new pH-ISFET based dissolved oxygen sensor by employing electrolysis of oxygen," *Sensors and Actuators B: Chemical* 34, 435-440, 1996.
14. J. Hendrikse *et al*, "A method of reducing oxygen induced drift in iridium oxide pH sensors," *Sensors and Actuators B: Chemical* 53, 97-103, 1998.
15. M. Lehmann, "Simultaneous measurement of cellular respiration and acidification with a single CMOS ISFET," *Biosensors and Bioelectronics* 16, 195-203, 2001.
16. J. Hendrikse *et al*, "The EMOSFET as a potentiometric transducer in an oxygen sensor," *Sensors and Actuators B: Chemical* 47, 1-8, 1998.
17. Ph. Arquint *et al*, "Integrated blood-gas sensor for pO2, pCO2 and pH," *Sensors and Actuators B: Chemical* 13, 340-344, 1993.
18. W. Zhong *et al*, "Imaging fluorescence lifetime modulation of a ruthenium-based dye in living cells: the potential for oxygen sensing," *Journal of Physics D: Applied Physics* 36, 1689-1695, 2003.
19. P. Hartmann *et al*, "Oxygen flux fluorescence lifetime imaging," *Sensors and Actuators B: Chemical* 38, 110-115, 1997.
20. M. Stücker *et al*, "FLIM of luminescent oxygen sensors: clinical applications and results," *Sensors and Actuators B: Chemical* 51, 171-175, 1998.
21. G. Liebsch *et al*, "Luminescence lifetime imaging of oxygen, pH, and carbon dioxide distribution using optical sensors," *Applied Spectroscopy* 54, 132A-143A and 463-638, 2000.

22. R. Prien, "The future of chemical in situ sensors," Marine Chemistry 107, 422-432, 2007.
23. D.D. Dunuwila *et al*, "Sol-Gel Derived Titanium Carboxylate Thin Films for Optical Detection of Analytes," *Analytical Chemistry* 66, 2739–2744, 1994.
24. D. Avnir *et al*, "Organic fluorescent dyes trapped in silica and silica-titania thin films by the sol-gel method: photophysical, film and cage properties," *Journal of Non-crystalline Solids* 74, 395-406, 1985.
25. B.D. MacCraith *et al*, "Fibre optic oxygen sensor based on fluorescence quenching of evanescent-wave excited ruthenium complexes in sol–gel derived porous coatings," *Analyst* 118, 385-388, 1993.
26. R.C.W. Lau, "Alcohol sensing membrane based on immobilized ruthenium(II) complex in carboxylated PVC and surface covalently bonded alcohol oxidase," Talanta 48, 321-331, 1999.
27. I. Klimant, "Oxygen-sensitive luminescent materials based on silicone-soluble ruthenium diimine complexes," Analytical Chemistry 67, 3160–3166, 1995.
28. O.S. Wolfbeis, "Materials for fluorescence-based optical chemical sensors," Journal of Materials Chemistry 15, 2657–2669, 2005.
29. P. Jorge et al, "Optical fiber sensing using quantum dots," Sensors 7, 3489-3534, 2007.
30. P.A.S. Jorge *et al*, "Quantum dots as self-referenced optical fibre temperature probes for luminescent chemical sensors," *Measurement Science and Technology* 17, 1032-1038, 2006.

CHAPTER 4

METABOLIC AND MASS TRANSPORT MODEL

As described in Chapter 3, the main motivation for direct oxygen measurements was to more fully characterize the method presented in Chapter 2, and quantify more precisely how the oxygen microgradients correspond to other measurements such as cell viability, pH and differentiation. In other words, it was necessary to relate all of the measured quantities via a metabolic and mass transport model to ensure that these parameters correspond to each other as expected and to also identify any inconsistencies and unexpected results that may arise.

Thus, a model has been developed which integrates two components: a cellular metabolic model and a finite element diffusion based mass-transport model.

4.1 Introduction

Mass transfer modeling for cell culture microenvironment applications is currently still in its early stages and, while basic models do exist, there are no standard models that are universally accepted. In particular, because of the relatively recent advent of microfluidic and lab-on-a-chip technologies, macro- and meso- scale mass transfer models do not necessarily apply for micro-scale applications.

In general, a model is useful in providing a "frame-of-reference" for the main factors driving mass transfer in microfluidic channels. Once such a "frame-of-reference" is established, an experimenter can identify the most important factors driving the mass

transfer process so that they could be built into the model. Then the experimental and theoretical results can be compared. If model predictions do not match experimental data, the experimenter can then set up alternative experiments to isolate and identify other contributing factors. If these factors are indeed important, they can also be included in the model.

At this point, it is important to establish the main phenomenon that the model is to represent. This is illustrated in Figure 4.1 below.

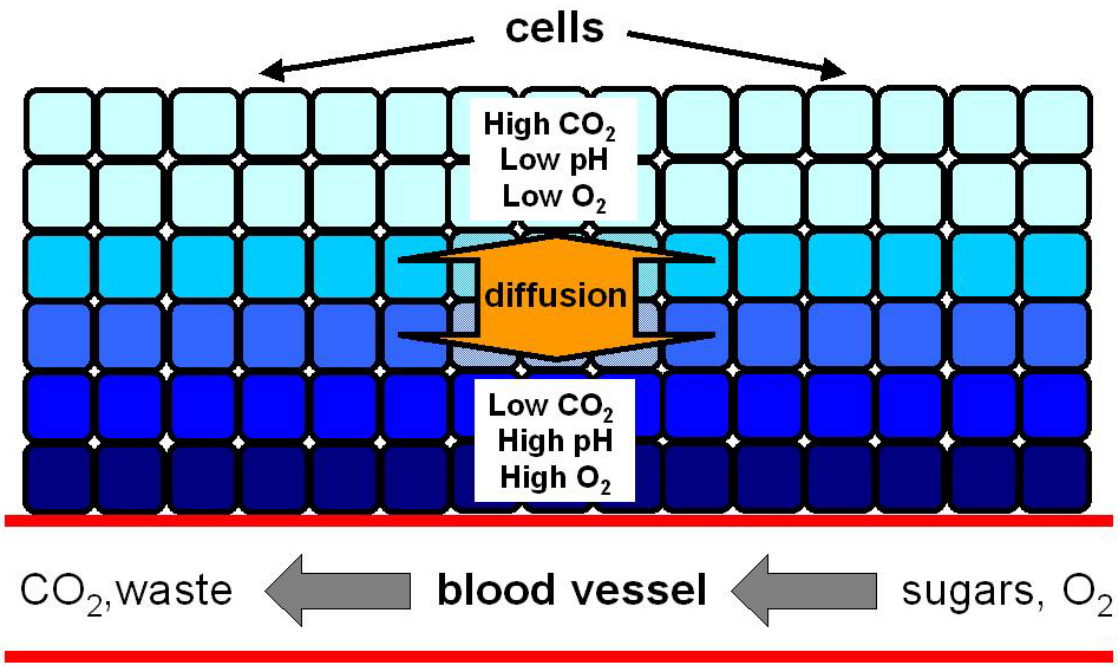

Figure 4.1: Oxygen mass transfer in multicellular tissues. In vertebrates, blood is composed of blood cells suspended in a liquid called blood plasma. Plasma comprises approximately 55% of blood fluid, is mostly water (90% by volume), and contains dissolved proteins, glucose, mineral ions, hormones, carbon dioxide and platelets. In particular, oxygen and sugars, such as glucose, are brought into close proximity to adjacent cells by a blood vessel; from there oxygen and glucose diffuse into adjacent cells where they are consumed to produce carbon dioxide, lactic acid and waste products. Because of the acidity produced by carbon dioxide and lactic acid, pH is lower (more acidic) away from the blood vessels than near it.

While Figure 4.1 describes oxygen mass transfer *in vivo*, Figure 4.2 below describes how these processes occur *in vitro* within the device described in Chapters 2 and 3.

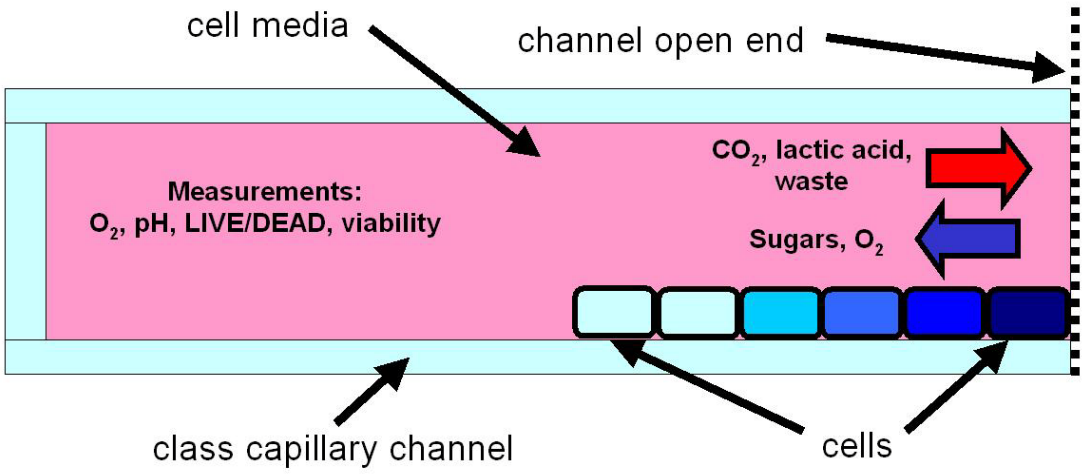

Figure 4.2: Oxygen mass transfer in glass capillary channels used in this method. Oxygen and sugars diffuse into the channels and are consumed to produce carbon dioxide, lactic acid and waste products. Because of the acidity produced by carbon dioxide and lactic acid, pH is lower (more acidic) as one goes further into the channel.

Specifically in the context of this work, it is useful to compare experimental data such as measured oxygen levels with model predictions to ensure that the model is consistent with the basic principles of cell respiration and mass transfer processes as reported in previously published results and literature. If such a correlation can be confirmed, the model can be further refined to identify and study secondary affects.

4.2 Existing Models of the Cellular Microenvironment

To construct the model for phenomena described in the previous section, it is initially important to review the kinds of models have already been built as well as what kinds of variables and parameters were included in these models, including metabolic rates of oxygen and related reagents. As described in the previous section, the model needs to include two main components: first, the structure of mathematical model itself and,

second, the physical and metabolic parameters with which to populate the mathematical model. The following review is structured around these two categories.

First, one must examine the various mathematical models that have previously been developed for oxygen mass transfer in tissues and cell culture applications. The main reagents involved in these processes are described under the blood-tissue exchange in Table 4.1. Finite element modeling (FEM) is usually used to describe diffusion of nutrients and wastes in cell tissue and *in vitro* culture [2, 3, 9, 10, 11, 16, 17, 19]. For example, Kirkpatrick *et al* describe a comprehensive model of mass transfer of oxygen and glucose with a special focus on hypoxia in tumors [3]; however, their results and numeral solutions are only limited to Krogh cylinder type geometries which are not appropriate in this case. A Krogh cylinder is a structure that includes two concentric circular tubes with the inner supplying media and the outer to culture cells – thus, this type of geometry is not appropriate in this case because diffusion profiles are radially symmetric from the center of this inner tube; this does not match the geometry and diffusion profiles of the channels described in Figure 4.2. Lai *et al* provide a review of oxygen mass transport and metabolism as well as affects on hyperoxia in muscle cells; they develop a comprehensive list of metabolic factors and model parameters [10]; however, their model also applies only to Krogh cylinder type geometries. Saito *et al* present a relatively simple oxygen consumption model in the context of their experimental results with *E.coli* bacteria [11]; their model solution is built upon previous work and is limited to radially symmetric geometries. Mehta *et al* demonstrated experiments to extract cellular metabolic rates, such as oxygen consumption, from a flow through microfluidic system; their mathematical model includes mass transfer and

diffusion considerations but is limited radially symmetric geometries [16]. Zhao *et al* studied oxygen transport effects on mesenchymal stem cell metabolic activity and developed a corresponding mathematical model [17]; however, their model and numerical solutions was based on a "sandwich" geometry which also did not match this case. Radisic *et al* developed a comprehensive model of mass transfer of oxygen in cardiac tissue and used a perfusion based fluidic system to verify their model predictions [19]. Tam *et al* introduced multiple quasi steady states into their metabolic model; that is, "plateaus" of cellular metabolic processes [2]; this is an interesting concept and birth-death "plateaus" are explored further in Section 4.6 below. In summary, previously constructed mathematical models were limited to very specific Krogh cylinder and other radially symmetric geometries. Furthermore, nearly all of the previously developed models were solved numerically and, even in the simplest cases, explicit solutions could not be obtained. Thus, for asymmetric capillary channel geometries in this case, a completely new mathematical model had to be developed.

Second, one must examine previously reported intracellular metabolic reagents and their values as reported in literature; a summary of such reagents is provided in Table 4.1 below.

Glycolysis	Krebs Cycle	Blood-Tissue Exchange	Lipolysis	Energy Transfer Processes
Glycogen	Acetyl-CoA	**Glucose**	Triglycerides	NAD+
G6P	Citrate	Pyruvate	Palmitoyl CoA	NADH
GAP	α-Ketoglutarate	**Lactate**		ATP
1,3 BPG	Succinyl-CoA	Palmitate		ADP
	Succinate	Glycerol		Phosphocreatine
	Malate	Alanine		Creatine
	Oxaloacetate	**Oxygen**		
		Carbon Dioxide		

Table 4.1: Chemical reagents and their functional roles in cellular metabolism. These reagents are organized by the processes in which they participate; and the processes themselves can be organized into two categories: intracellular (i.e., taking place inside the membranes of cells) and extracellular (i.e., taking place outside of the cells). Glycolysis, Krebs Cycle, Lipolysis and energy transfer are intracellular processes. Blood-tissue exchange is a set of extracellular processes driven by diffusion. Glycolysis is the metabolic pathway that converts glucose into pyruvate. In aerobic organisms, the Krebs cycle is part of a metabolic pathway that chemically converts sugars into carbon dioxide and water to generate a form of usable energy. Lipolysis is a process that breaks down triglycerides into free fatty acids within cells [9]. Reagents that are included in the developed model are highlighted in red.

As presented in Table 4.1 above, there are lots of participating reagents in the cellular metabolic process. However, only a few of them (highlighted in red in Figure 4.1) are the net products in the overall respiration pathway. These net respiration pathways are further described below and are summarized in Figure 4.3. Additionally, since the model was to be used as a comparison tool for measured data, it is generally sufficient to focus on quantities that can be measured (e.g., lactate and carbon dioxide for pH and oxygen); in other words, the model should include only the inputs and outputs of the overall metabolic pathways.

Specifically for C2C12 cells (the cells that were used in the experiments described in Chapters 2 and 3), Arthur *et al* provide established values for C2C12 cell oxygen consumption and lactate production rates. They also provide an informative discussion on

the dependence of oxygen uptake on oxygen concentration [1]. McMahon *et al* provide a review of C2C12 cell and myotube properties and metabolic rates [4]; this paper is not as useful as Arthur *et al*, but it does provide the doubling time for C2C12 cells (~12 hours). Jafri *et al* describe cellular metabolism in detail including glycolysis, TCA and oxidative phosphorylation and corresponding reagents [5]; this is a good review of cellular metabolic processes but does not specifically provide any relevant parameters for C2C12 cell metabolism.

It is also useful to examine previous literature where various oxygen effects were explored and certain metabolic rates and parameters were established. These results are not directly relevant to C2C12 cell metabolism, but introduce concepts that could be included in the model. The following is a summary of such previous work. Kim *et al* discussed how glucose and oxygen deprivation affects HeLa cancer cells; in their experiments, dissolved oxygen is varied from 0% to 21% [6]; their experiments showed that even at high temperatures (40-42C) glucose-deprived cells survived in low oxygen environments (less than 10%). In other words, oxygen, and not glucose, seems to be the limiting factor for the ability of cells to survive. Orczyk *et al* studied HeLa oxygen consumption rates using dissolved oxygen measurement techniques via Clark type electrodes [7]; their study explored oscillatory patterns of oxygen consumption in HeLa cells. This is an interesting concept to consider for the model; however, Orczyk *et al* reported oscillation periods of ~30 minutes and the effect may not be significant for timescales of 24-164 hours as presented in Chapters 2 and 3. Allen *et al* discussed limitations of oxygen diffusion in culture dishes and flasks; hyperoxia and hypoxia affects, as well as corresponding variables and parameters, were also investigated and

discussed [8]; this work is important to consider because, as the authors report, it may take ~3 hours for the media solution in a Petri dish or, similarly, a microfluidic channel to reach equilibrium to the surrounding medium. In this case, however, oxygen concentration was maintained at the same level (21%) within and outside of the cell culture incubator. Schunck *et al* studied oxygen consumption of cells grown on microbeads [12]; in this context, the authors reported a study on photodynamic therapy (PDT), which is a form of cancer therapy based on the accumulation of a photosensitizing drug in malignant tissues. While this work does not directly apply to first-generation model, this sort of scheme is good to keep in mind for modeling more complex oxygen metabolism as described in Chapter 5. Rotem *et al* studied how oxygen affects tissue formation and assembly as well as how oxygen affects cell attachment and spreading [13]; this work was important to consider because C2C12 cells need to attach in order to proliferate. Rotem *et al* showed that even at very low oxygen concentrations (less than 0.1%) more than 50% of cells still were able to attach to the Petri dish surface. This finding indicates that, C2C12 cells should be able to attach at the start of the experiments described in Chapters 2 and 3. Ma *et al* studied how oxygen gradients affect cellular proliferation and differentiation; they also discussed oxygen tension effects for tissue engineering applications [14]; their experiments showed that, in moderate hypoxia (2% dissolved oxygen), placental trophoblast-like cells secrete a hormone called estradiol at about one half the rate of normoxic conditions at 21% oxygen. This finding, that cell metabolic rates drop by about 50% in hypoxic conditions, matches the reported other reported data from Arthur *et al* [1]. Gray *et al* discussed and studied oxygen sensing with *C. elegans* as well as avoidance of hyperoxia in cells [15]; this work presents an

interesting concept of social "feeding", which can be used as a behavioural strategy for responding to hyperoxic environments. This concept can be incorporated in later versions of the model. Rivera *et al* experimented to study effects of thermal stress on oxygen metabolism in two-cell bovine embryos [18]; their finding showed that the reduction in the proportion of embryos that became blastocysts caused by heat shock was not exacerbated when embryos were cultured in air (21% O_2) as compared with 5% O_2. These results seem to suggest that, even for the more sensitive embryonic stem cells, reduced oxygen supply is secondary to heat shock treatment. This means that temperature effects may need to be taken into account in the model.

Based on this model literature review, the main problem with previously developed approaches is that they do not match the device geometry for this case. Thus, a more flexible model and simulation approach had to be developed – one that meets the requirements of device geometry in this case and also be flexible enough to be adapted for other device geometries in the future. The next section describes the scope of the model whose output was used as a comparison to the data collected in experiments described in Chapters 2 and 3.

4.3 Scope and Description of the Model

Based on the literature review in the previous section, there are many factors that have been identified and studied in the past to construct various cellular metabolic models as summarized in Table 4.1. However, while there are many secondary and tertiary factors that are used in metabolic modeling, the primary phenomena that the model needs to include are summarized in Figure 4.3 below. The primary factors include

the main reagents participating the only two possible net respiration pathways – glucose, oxygen, carbon dioxide and lactic acid. Thus, the scope of the model is limited by how much oxygen is consumed and how much carbon dioxide and lactic acid are produced. Also, other parameters such as how much oxygen is required to keep the cells alive are included as well. A complete list of model parameters are listed in Section 4.5. Furthermore, as described in Section 4.2, previously developed models were not a match for this case because they either focused on different device geometries or were too biologically detailed to be relevant to measured data that can be obtained with this method. In summary, the scope of the model is limited to the overall net metabolic pathways, not the sub-components of these pathways such as glycolysis, Krebs Cycle and lipolysis.

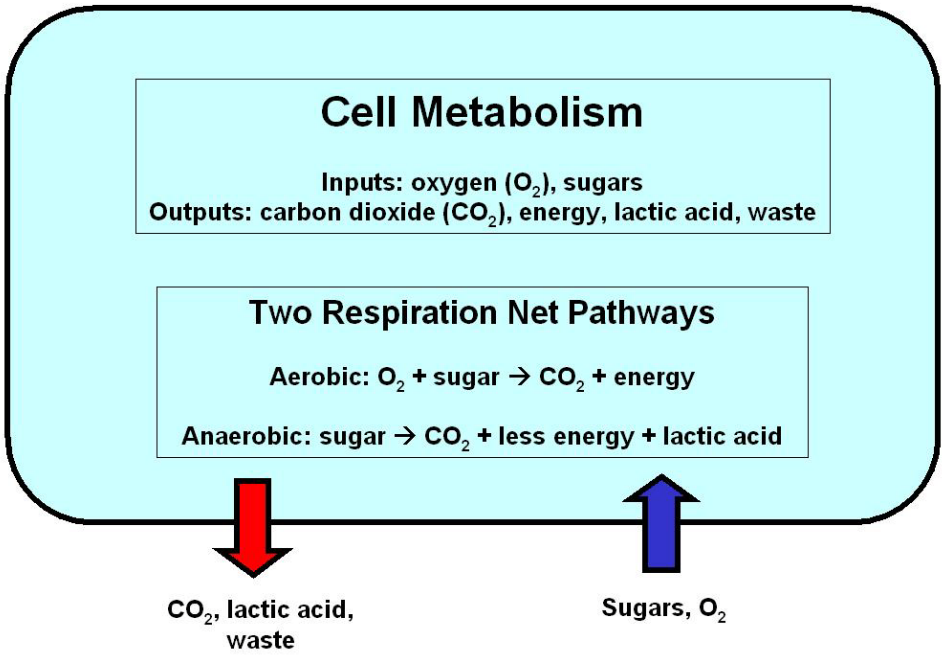

Figure 4.3: Scope of the model. For intracellular processes, oxygen and sugars are consumed by the cells while carbon dioxide, lactic acid and wastes are produced. Outside of the cells, mass transport of these inputs and outputs of the intracellular processes is driven by diffusion.

As such, the following metabolic reagents are included within the scope of the model:

- oxygen (diffuses into the channels through the open end as was shown in Figure 4.2 above)
- carbon dioxide (produced by the respiration process of the cells)
- lactic acid (also produced by the respiration process of the cells; lactic acid production is driven by anaerobic respiration and its rate of production increases as the extracellular environment becomes more hypoxic)

Thus, the model uses the above three reagents for metabolic processes occurring intracellularly, or within the cells. These processes are driven by the following reaction for aerobic respiration:

$$\mathbf{C_6H_{12}O_6 + 6\ O_2 \rightarrow 6\ CO_2 + 6\ H_2O + ATP\ (energy)}$$

In this reaction, one molecule of glucose, $C_6H_{12}O_6$, combines with 6 molecules of oxygen to produce 6 molecules of carbon dioxide and water; this process generates energy for the cells. This relationship of oxygen to carbon dioxide, in a **one-to-one ratio**, is reflected in the code of the model as described in Appendix C. Also, in aerobic respiration, 38 molecules of ATP molecules are produced from one glucose molecule while in anaerobic respiration, described below, only two ATP molecules are produced from one glucose molecule. Thus, the aerobic respiration processes in much more efficient in producing ATP molecules that cells use as a form of energy to run various intracellular processes.

Next, one needs to consider anaerobic respiration; it is driven by the following equation:

$$\mathbf{C_6H_{12}O_6 \rightarrow 2C_3H_6O_3 + ATP\ (energy)}$$

In anaerobic respiration, one molecule of glucose is consumed to produce 2 molecules of lactic acid, which, in solution, can lose a proton from the acidic group to produce the lactate ion mentioned in Table 4.1 above. As can be seen, no oxygen is consumed in the anaerobic respiration process. However, it is important to know how much lactic acid is produced at various concentrations of oxygen, since its production is oxygen dependent. Lactic acid production also depends on the type of cells – some cells use anaerobic respiration pathways more than others. For C2C12 cells that were used in Chapter 2 and Chapter 3 experiments, Arthur *et al* provide good discussion and values for lactic acid production in this type of cells; specifically, for C2C12 cells, it was previously shown that lactate production was 6 nmol/min/10^6 cells during normoxic conditions and it dropped by approximately 20% in hypoxic conditions; also, the same study of C2C12 cells showed that, during normoxic conditions, oxygen consumption was approximately 2 nmol/min/10^6 cells [1]. Thus, based on this previously reported work, one can assume a **three-to-one ratio** of lactic acid produced to oxygen consumed during both hypoxic and normoxic conditions. This is also reflected in the model code as described in Appendix C.

4.4 Diffusion and Finite Element Model (FEM)

Section 4.3 describes the mass transfer equations for the intracellular metabolic processes and reagents that are within the scope of the model. While the intracellular processes are modeled by the reactions described above, diffusion is modeled using a finite element model (FEM) where a 2-dimensional mesh is set up over the height and length of a channel and the values of dissolved oxygen, carbon dioxide, lactic acid and

cell density are iterated over a large number of time steps. To accelerate the computation time by an order of magnitude, as described in detail in Appendix B, the mesh was set up with rectangular (vs. square) elements. The details of the FEM and the corresponding code are described in Appendices B and C.

4.5 Model Inputs, Outputs and Parameters

Now that the scope of the model has been defined, it is important to review the parameters used in the model as well as the inputs and outputs that the model produces. **The model is a physical (vs. statistical regression) model [20] and, thus, most of the parameters cannot be varied because they are directly tied to physical phenomena such as diffusion.** In other words, most of the model parameters cannot be varied because they reflect known physical quantities that have been measured, not because the model cannot accept different parameter values.

The following is a comprehensive list of the model inputs including values that were used:

Name	Value	Unit	Description
c0	1	unitless	initial oxygen concentration inside of a channel and exterior oxygen concentration; this input is unitless in the model and the value of 1 corresponds to the concentration of oxygen in water at room temperature and pressure of 1 atm at full saturation; for example, c0=1 corresponds to ~9 part per million (ppm) of dissolved oxygen
n0	0.8	unitless	initial cell density; this input can be varied by changing the concentration of cells-media suspension before loading into the device as described in Chapter 2; n0=0.8 means that, at the start of an experiment, cells cover 80% of the surface at the bottom of the channel; n0 cannot exceed 1
tauObservation	24	hours	observation period, in hours. This input is used to

			control the simulated time of the model run. For example, tauObservation = 24 means that the model will, given the other input, predict the oxygen concentration and other outputs after a simulated 24 hour period; as is described in the list of outputs below, the model provides the number of iterative time steps necessary to simulate for the required number of hours
[t1,t2]			observation window, where t2 is the last time step within the window, and t1 is the last time step preceding the window; for example, if T=35000 time steps, t1=1000, and t2=4000, then, of the total 35000 time steps, the observation window is over the time steps 1001, 1002, ..., 4000. This is a useful input to see what happens over time increments rather than over an entire observation period
Delta y			vertical measurement of one mesh block, in mm; for example, if a channel is 300 μm in height, one can choose Delta y = 0.1mm; in this case the mesh will have 3 (horizontal) rows of blocks that are each 0.1 mm, or 100 μm
Delta x			horizontal measurement of one mesh block, in mm; for example, if a channel is 50 mm in length, one can choose Delta x = 1 mm; in this case the mesh will have 50 (vertical) columns of blocks that are each 1 mm
w			number of blocks in one (horizontal) row; w is an integer
h			number of blocks in one (vertical) column; h is an integer

The following is a comprehensive list of the model outputs:

Name	Value	Unit	Description
c		unitless	current concentration of oxygen relative to c0, so that $0 \leq c \leq 1$ and c*c0 is the concentration of oxygen, depending on the time and space coordinates
n		unitless	cell density, depending on the time and space coordinates; as described above, $0 \leq n \leq 1$
CO2		unitless	current concentration of CO2 relative to c0, so that CO2*c0 is the concentration of CO2, depending on the time and space coordinates
Lact		unitless	current concentration of lactic acid relative to c0, so that Lact*c0 is the concentration of lactic acid,

			depending on the time and space coordinates
T		unitless	number of time steps in the observation period; this output is determined by tauObservation (as described above) and the diffusion coefficients described below

The following is a comprehensive list of the model parameters including values that were used along with the corresponding references, where necessary:

Name	Value	Unit	Description	Source /Reference
Diff O_2	0.002	mm^2/sec	diffusion coefficient for oxygen in water	[16]
Diff CO_2	0.0015	mm^2/sec	diffusion coefficient for CO2 in water	[6]
Diff Lactic	0.0009	mm^2/sec	diffusion coefficient for lactic acid in water	[11]
cr	0.025	unitless	critical level of c (oxygen concentration): cells will be dying if c<cr and will be multiplying if c>cr; for C2C12 cells the previously reported value for this parameter is 0.025	[1]
nmax		unitless	maximum possible cell density, so that n cannot exceed nmax; in turn, the constant nmax cannot be greater than 1	
taud	2	hours	half-life time, in hours; that is, the amount of time for the live cells to halve their number when c=0; more about this parameter will be discussed below	
taub	12	hours	doubling time, in hours; that is, the amount of time for cells to double their number when c=1; the density of cells, n, is subject to the restriction that $n \leq$ nmax; more about this parameter will be discussed below	[4]
la	0.8	unitless	a coefficient for lactic production; according Arthur *et al* [1], lactate output may decrease by 10-20% as the oxygen concentration decreases from the normoxic levels (c>0.1); this coefficient accounts for such a decrease	[1]
B	3	unitless	parameter of the birth-death rate profile curve, the greater value of B, the	

			steeper is the curve at c=cr; more about this parameter will be discussed below	
rho	0.02	unitless	fraction of oxygen consumed of the total oxygen that reaches the cell surface during a given time step; rho decreases to 0.01 in hypoxic (c<0.05) conditions and follows a square root relationships from it's maximum of 0.02 to its minimum of 0.01 [1]; this is reflected in the code of the model as described in Appendix C	[1]

As the next step, it is important to review the main model parameters listed above and perform a sensitivity analysis to determine which parameters can and cannot be changed as well as to determine which parameters make the most impact on model predictions. This is the subject of the next section.

4.6 Model Sensitivity Analysis

From the list of parameters in the previous section, the following cannot be changed at all: Diff O_2, Diff CO_2, Diff Lactic and nmax – diffusion coefficients are well established and maximum cell density cannot exceed full confluence, or 100%. Furthermore, parameters la and rho are reported in previous literature [1], and are generally well accepted figures [4,6,12]; additionally, la only controls the production of lactic acid and pH; it does not affect the model prediction for oxygen concentration and cell density.

This leaves taud, taub, cr and B. As one will recall, B is the parameter that controls the "steepness" of the birth-death curve in the model – that is, the parameter B determines the "steepness", or rate, of cell death or growth for a given cr. As illustrated in Figure 4.4 below, a series of birth-death curves are shown for cr=0.025 with the B parameter varied

from 0.01 to 10. For low B's (such as B=0.01), the birth-death curve is very "steep" around c=cr=0.025; in other words, in this case cells begin do double almost immediately after oxygen concentration moves above c=cr=0.025. Conversely, for high B's (such as B=10); the birth-death curve is very "flat" around cr; in other words, even for concentrations much higher than cr=0.025 (such as c=0.6), the cells are still not even close to beginning to double and their numbers remain constant. As a reminder, c cannot be greater than 1. The functions driving these profiles were arbitrarily picked and are fully described in the code in Appendix C.

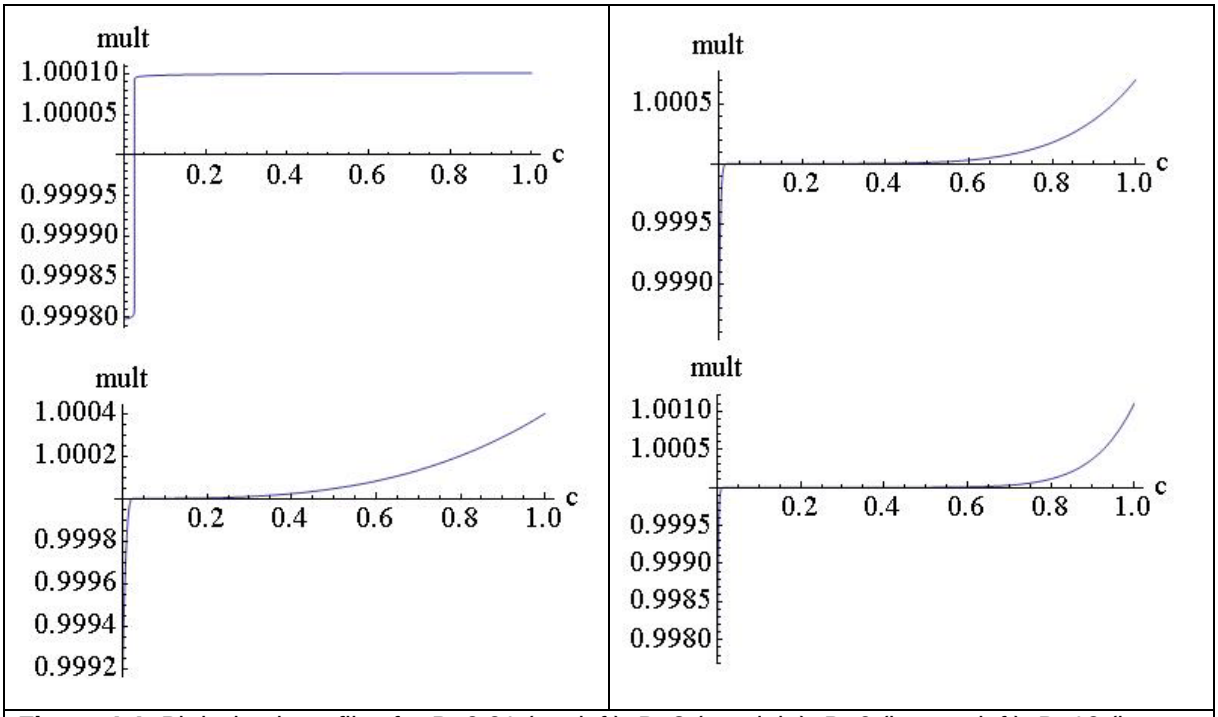

Figure 4.4: Birth-death profiles for B=0.01 (top left); B=3 (top right); B=6 (bottom left); B=10 (bottom right). The "steepness" of the birth-death curve decreases with B. All birth-death curves center around cr; for c>cr, cells multiply and for c<cr, cells die. The steepness determines the rate at which the birth-to-death or death-to-birth transition takes place. On the horizontal axis is c, the concentration of dissolved oxygen. And on the vertical axis is mult, the multiplier coefficient that is used to compute cell density (n) at each given time step of a simulation as specified in the code provided in Appendix C. As explained above, both c and mult are unitless quantities.

Because the above family of birth-death curves were arbitrarily generated (once again, around a previously reported value of cr [1]) it is important to determine how

various values of B affect the output of the model predictions. To do this, model simulations were conducted for various values of B and predicted values of oxygen in a channel were computed while all other parameters were kept the same. The results of this simulation are shown in Figure 4.5.

	Dissolved Oxygen (ppm) vs. Position (mm)										
Position	**0**	**1**	**2**	**3**	**4**	**5**	**6**	**7**	**8**	**9**	**10**
Dissolved Oxygen (B=0.01)	9	4.30803	2.172753	1.13337	0.613877	0.356854	0.245068	0.231719	0.218523	0.205414	0.192504
Dissolved Oxygen (B=3)	9	4.312584	2.185011	1.161018	0.641591	0.371363	0.237764	0.189167	0.172404	0.16191	0.152796
Dissolved Oxygen (B=6)	9	4.341915	2.265966	1.219437	0.67244	0.382019	0.229775	0.157635	0.132962	0.122972	0.116017
Dissolved Oxygen (B=10)	9	4.347783	2.282184	1.230408	0.678462	0.383253	0.225424	0.145246	0.113446	0.104081	0.09976

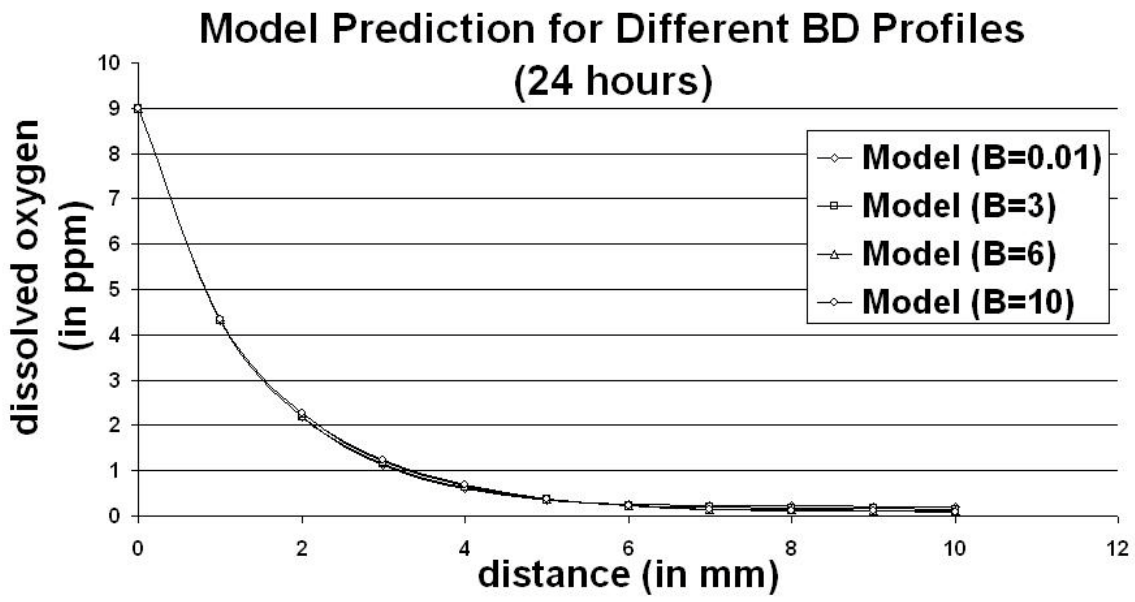

Figure 4.5: Model predictions for various B's and corresponding birth-death (BD) curve profiles. While the output changes slightly, there is no significant difference between the predicted dissolved oxygen levels even for very different values of B, such as B=0.01 and B=10. As a reminder, these birth-death profiles themselves are very different themselves as illustrated in Figure 4.4. While counterintuitive, these results make sense physically because birth-death curves only reflect the *rates* at which cells multiply or die; in other words, if the cell density is already high at the beginning of experiment (n=0.8) then oxygen will be consumed at roughly the same rate for different B's. Additionally, the plots in this figure are simulations for a 24 hour period after which the system has reached a relative equilibrium (i.e., the cells that have been deprived of oxygen have died, and the cells in oxygen-rich regions have multiplied to the maximum density of n=1).

Thus, as can be seen from the figure above, the model predictions for various birth-death curves profiles results in nearly identical dissolved oxygen prediction. Because of

this, one can make the determination that B, or "steepness" of the birth-death curve, does not have a significant effect on the model output for dissolved oxygen.

This leaves taud, taub and cr. However, taud and taub are actually linked with B – in other words, higher taud and taub correspond to lower B's; and, conversely, lower taud and taub correspond to higher B's. Thus, taud and taub will also not have a significant affect on the model output.

Now one is left only with cr – as a reminder, this parameter sets the concentration of dissolved oxygen above which the cells grow in numbers and below which they die. In retrospect, it makes sense that cr is really the main parameter that mainly controls the model outputs because consumption of oxygen by cells is largely established in literature [1,4,6,12,16] and diffusion coefficients are also well known entities [6, 11, 16]. On the other hand, even cells in the same line can be more or less susceptible to hypoxic, or low oxygen, conditions; that is, even for the line of C2C12 cells used in experiments described in Chapters 2 and 3, the ability of the cells to survive at lower oxygen concentrations could be significantly different than that of the cells reported in prior studies as reported in literature.

Thus, based on the analysis and reasoning presented in this section, the main parameter that can potentially be varied is cr.

The next step is to compare the actual measured levels of dissolved oxygen with model predictions. This is the subject of the next section.

4.7 Model Predictions vs. Actual Measurements of Dissolved Oxygen

To put the developed model to the test, this section will compare model predictions with the actual measured values of dissolved oxygen. Based on the literature review and sensitivity analysis presented in the section above, the model was run with the following set of inputs and model parameters.

Inputs

c0 =	initial concentration of oxygen in the channel	1	unitless
n0=	initial cell density	0.8	unitless
nmax=	maximum cell density	1	unitless
Dey=	vertical measurement of one block in the mesh	0.1	mm
Dex=	horizontal measurement of one block in the mesh	1	mm
h=	number of mesh blocks in one (vertical) column; h is an integer	3	unitless
w=	number of mesh blocks in one (horizontal) row; w is an integer	50	unitless
tauo=	observation period	~24	hours

As a reminder, all of these inputs are explained in more detail in the Section 4.4 and with corresponding references for parameter values.

Model Parameters

Diff=	diffusion coefficient for oxygen in water	0.002	mm2/sec
Diff CO2=	diffusion coefficient for carbon dioxide in water	0.002	mm2/sec
Diff Lactic =	diffusion coefficient for lactic acid in water	0.009	mm2/sec
cr=	critical oxygen concentration level: cells will be dying if c<cr*c0 and will be multiplying if c>cr*c0	0.025	unitless
taud=	time to halving the number of live cells at c=0	2	hours
taub=	time to doubling the number of live cells at c =1	12	hours
nmax=	maximum cell density	1	unitless
la=	a coefficient for lactic production	0.8	unitless
B=	parameter to control the “steepness” of the birth-death curve	3	unitless
rho=	fraction of oxygen consumed of the total oxygen that reaches the cell	0.02	unitless

As a reminder, all of these parameters are explained in more detail in the Section 4.4 and sensitivity analysis for these parameters is presented in Section 4.5. Based on these inputs

and parameters, the model provides the following outputs as described in Figure 4.6 below.

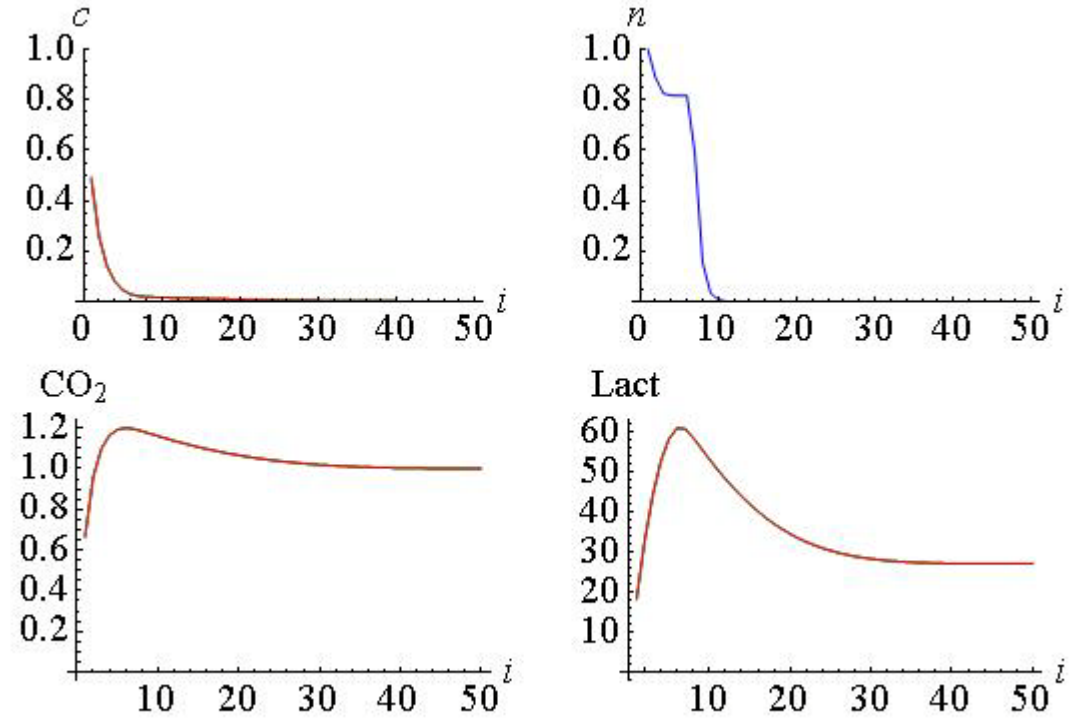

Figure 4.6: Model predictions for inputs and parameters described in this section. Outputs include normalized concentration of dissolved oxygen (top left), density of live cells (top right), concentration of dissolved carbon dioxide (bottom left) and concentration of lactic acid (bottom right). Concentrations of carbon dioxide and lactic acid are relative to the normalized concentration of dissolved oxygen. For all of the figures, the horizontal axis in position along the length of the channel and the units are in mm.

As can seen in Figure 4.6, the model predicts the behavior that was observed from data presented in Chapters 2 and 3. As observed, dissolved oxygen concentration and density of live cells decreased as one moved away from the open end of the channel (i.e., x=0 mm). Furthermore, the model predicts lower concentrations of carbon dioxide and lactic acid near the open end of the channel (i.e., x=0 mm). This trend was observed and reported in Figure 2.6 where carbon dioxide and lactic acid increased the acidity and, correspondingly, lowered pH further away from the open end of the channel.

In order to make more precise comparisons of model predictions versus the actual measured data, the Figure 4.7 compares model to measured values of dissolved oxygen in 5 independent channels.

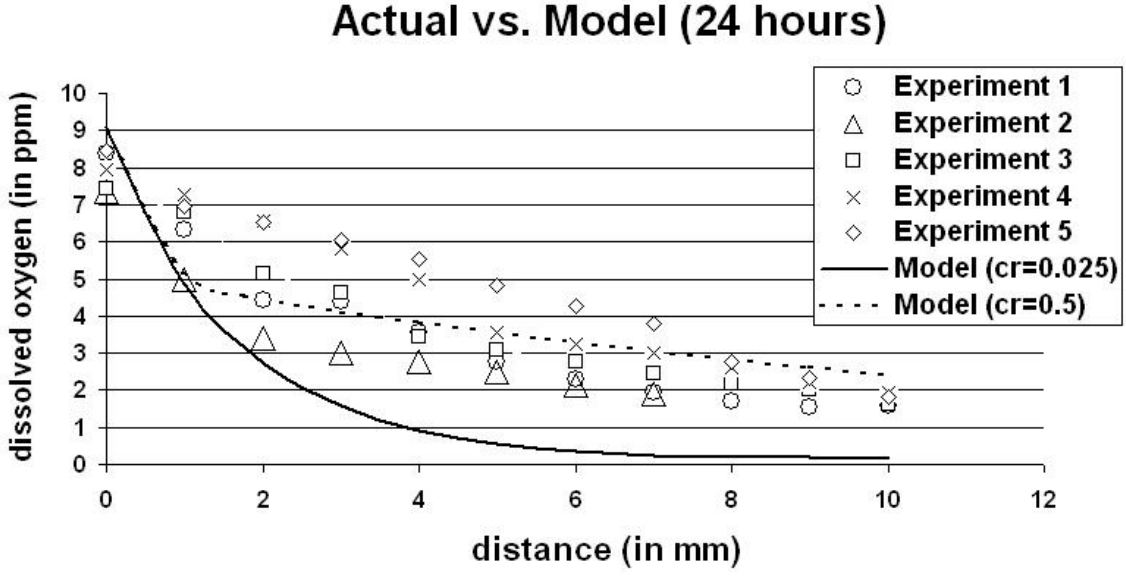

Figure 4.7: Measured values of dissolved oxygen and model predictions after a 24-hour period. Model predictions are computed for cr=0.025 and cr=0.5. The discrepancies at small distances from the capillary edge can be explained by the fact that full saturation of oxygen is temperature and salinity dependent and can vary by as much as 1-1.5 ppm; it was assumed to be 9 ppm but could have been as low as 8 ppm in the actual experiments.

As can be seen from Figure 4.7, while model predictions (for cr=0.025) match the general trend of the measured data, the predicted values are significantly lower from the measured data. However, as discussed in Section 4.5, value for cr can vary widely and depends on the ability of cells to survive in hypoxic conditions of the cells [1,4,16,18]. Also, as was determined in the model sensitivity analysis of Section 4.5, cr is the only parameter that indeed can be varied; all of the other parameters either (i) cannot be varied because they are closely tied to physical phenomena, such as diffusion coefficients, or (ii) their variation does not result in significant difference in model predictions, such as with

B (the parameter that determines the "steepness" of the birth-death curve) or half-life and doubling time parameters.

Thus, it is reasonable to conclude that cr must be different for the C2C12 cells used in these experiments. By using cr=0.5 and running model simulation, one can see that the data and model predictions match much better than for cr=0.025 [1] (Figure 4.7).

The above is a useful conclusion, but it must be tested by running the experiment again with a new set of capillary channels and, correspondingly, a new set of collected data, and then comparing measured values with model predictions at various times. This is subject of the next section.

4.8 Time Course Experiments

To test the ability of the model to predict measured data, a separate experiment was constructed. In this separate experiment, time course oxygen measurements were taken at 2-hour intervals after seeding the channels with cells in 6 separate capillary channels over an 8-hour period. For the model parameters, the most optimal set was used as was established in Sections 4.6 and 4.7. Before looking at the dissolved oxygen data, it is worth to consider live cell profiles as predicted by the model as shown in Figure 4.8 below.

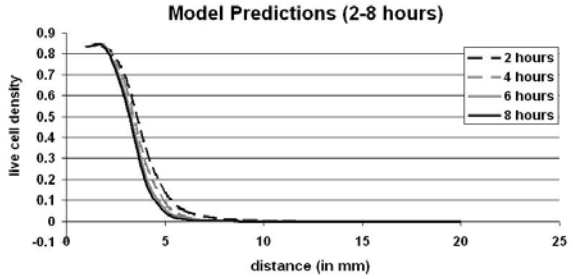

Figure 4.8: Model predictions (cr=0.5) for live cell density at 2-8 hours after the start of the experiment. The profiles gradually become "steeper" as cells further away from the capillary edge die. As the cells die, more oxygen should be available for cells closer to the open end. This is indeed what is observed as shown in Figure 4.9.

Next, the following data compares model predictions and actual average measured data for dissolved oxygen in 6 separate capillary channels. Figure 4.9 shows model predictions and average measured data for dissolved oxygen 0, 2, 4, 6 and 8 hours after the start of the experiment.

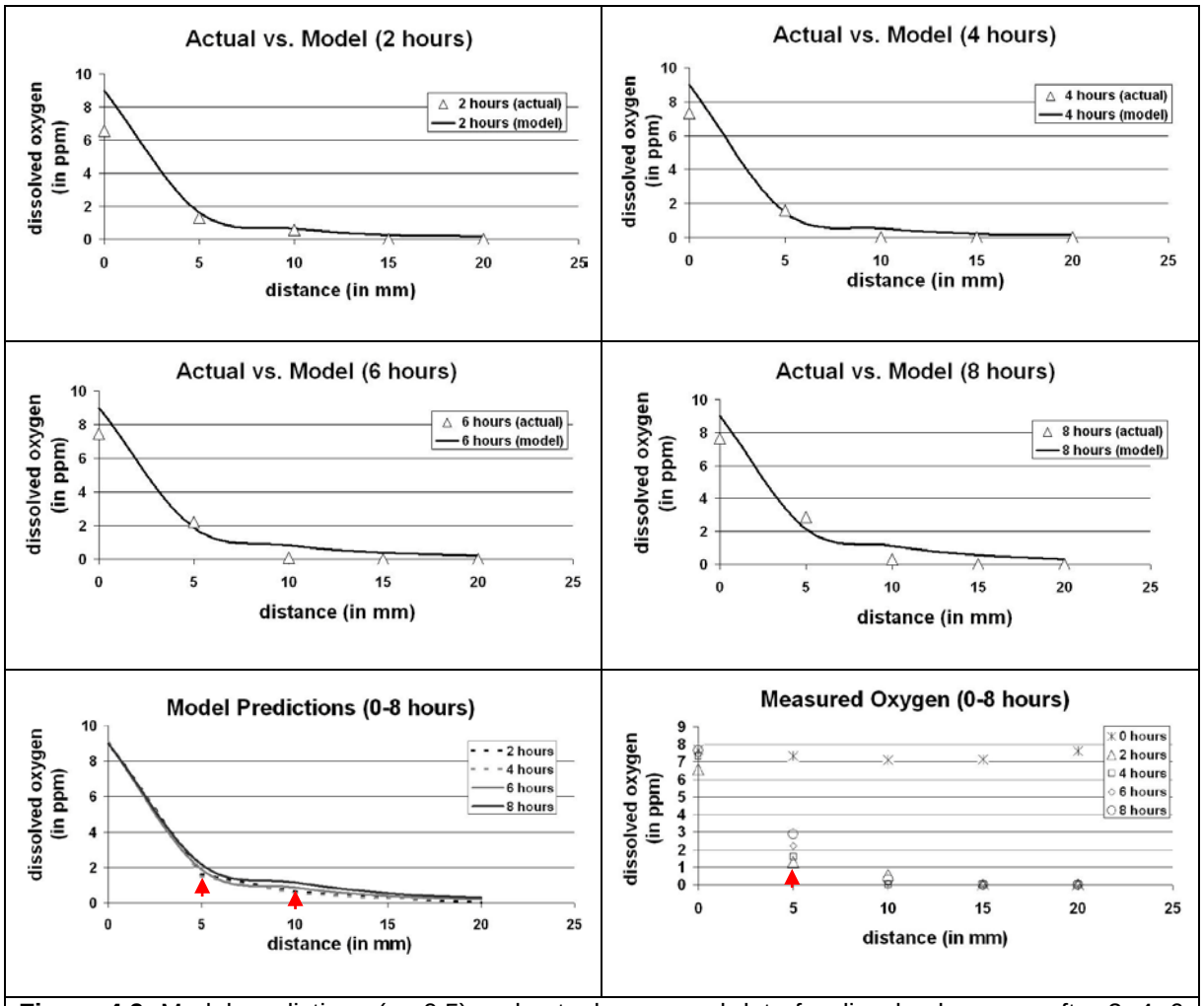

Figure 4.9: Model predictions (cr=0.5) and actual measured data for dissolved oxygen after 2, 4, 6 and 8 hours after start of the experiment. Measured data is an average of 6 independent channels. Combined model predictions for dissolved oxygen for 2, 4, 6 and 8 hours after start of the experiment (bottom left). Combined measured data for dissolved oxygen for 0, 2, 4, 6 and 8 hours after start of the experiment (bottom right). Notably, measured data for first data point, at the channel inlet (i.e., x=0), is consistently and significantly lower than the model predicted values; this is due to the fact that, in actual experiments, there were living cells immediately outside of the capillary channel and they consumed some of the oxygen before it entered into the channel.

As can be seen in Figure 4.9, model predictions are close to measured oxygen data. Especially encouraging is the correlation of measured and predicted values at x=5mm and x=10mm. After 4 hours after the start of the experiment, model predictions continue to match measured data well. Notably, measured values at x=5mm slightly increased while at x=10mm it slightly decreased. This is likely due to the fact that as cells further away from the open end of the channel (at x=10mm) begin to die, they leave more available oxygen to be consumed by cells closer to the open end of the channel, such as at x=5mm. The trend continues 6 and 8 hours after the start of the experiment – dissolved oxygen concentration increases slightly again at x=5mm and stays nearly the same at x=10mm; the concentration of dissolved oxygen increases further at x=5mm while it stays the at nearly the same level at x=10mm. Additionally, over the course of this experiment, measured value of dissolved oxygen at x=0mm also increases gradually. Also, the model predicted for dissolved oxygen at x=5mm also gradually increases.

Another way to look at the data is to see all time course data for measured oxygen and model predictions on separate plots to see how the values change overtime. This is shown in the two graphs at the bottom of Figure 4.9.

For measured oxygen data (Figure 4.9, bottom right), the notable change is at x=5mm. The increase in dissolved oxygen is likely due to the fact that cells further into the channel capillary are dying, and therefore consuming less oxygen; this leaves more oxygen available at points closer to the open end of the capillary such as at x=5mm.

Model predictions in Figure 4.9 (bottom left) match the trends of measured data at x=5mm as the amount of dissolved oxygen at that point is predicted to increase. However, the predicted increase is approximately 1 parts per million lower than that of

measured data. Also, the model predicts an increase in dissolved oxygen at x=10mm, whereas measured data stays approximately the same at that point. Thus, based on the reasoning presented earlier in this section, it appears that the actual cells are less resistant to surviving in hypoxic conditions than the model predicts.

4.9 Model Comparisons to LIVE/DEAD Data

Another useful comparison to make is to see how well the data and model predictions match up for the number, or density, of live cells. This can be done by comparing the LIVE/DEAD HeLa cell data presented in Chapter 2 (Figure 2.6) with model predictions. This comparison is presented in Figure 4.10 below.

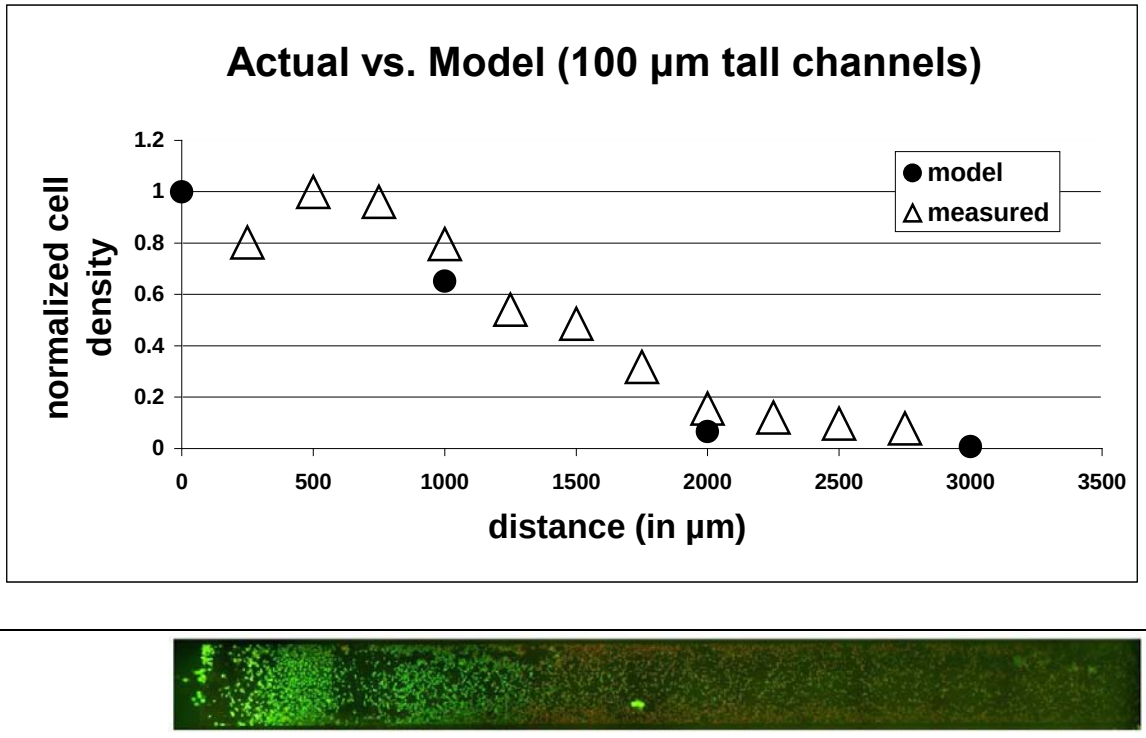

Figure 4.10: Model predictions and actual measured data for normalized HeLa cell density after a 24 hour period; capillary channel height of 100 µm (top) and a LIVE/DEAD image of a sample capillary channel (bottom). For model simulation, cr was kept at 0.5 as in results reported in Figures 4.7 and 4.8. These results show that, x=1mm, cells begin to die; from results reported in Figure 4.7, this corresponds to oxygen level of ~4.5ppm.

Data obtained from an independent set of experiments presented in Chapter 2 (Section 2.6) matches well with model predicted results using the same set of parameters established in Sections 4.4 and 4.5. In particular, there is sharp reduction in the normalized HeLa cell density between x=1mm and x=2mm and the model confirms this behavior.

Figure 4.10 showed comparisons to LIVE/DEAD data for capillaries with height of 100 μm. Another set of data was for capillary height of 50 μm and this data is compared in Figure 4.11.

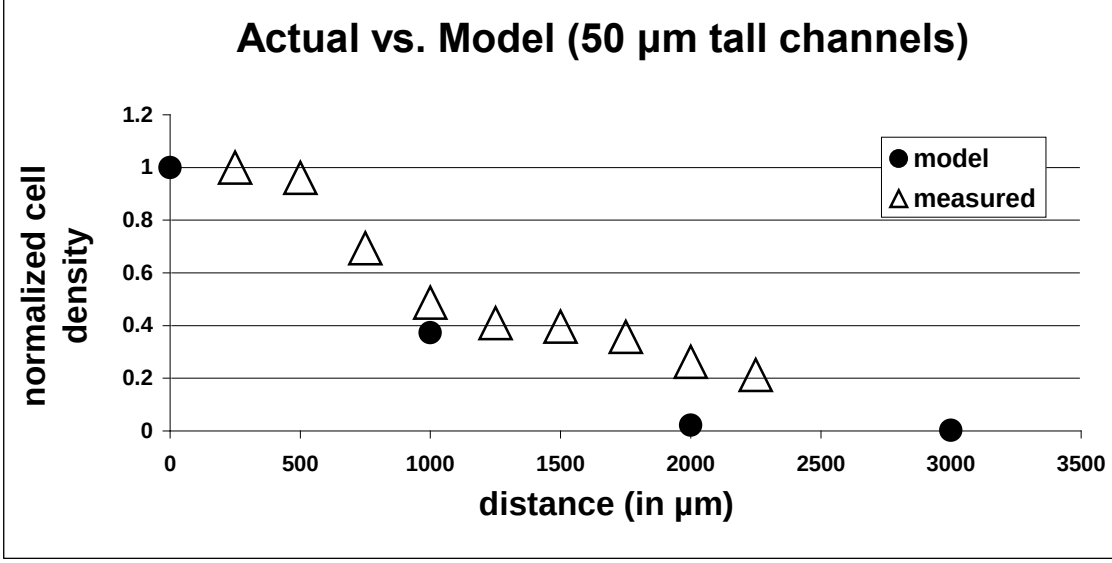

Figure 4.11: Model predictions and actual measured data for normalized HeLa cell density after a 24 hour period; capillary channel height of 50 μm. LIVE/DEAD data is shifted to along the x-axis to match the highest measured normalized cell density with the highest predicted density at x=0 mm. For model simulation, cr was kept at 0.5 as in results reported in Figures 4.7, 4.8 and 4.9.

As can be seen from Figure 4.11, data for the 50 μm tall channels also matches the model predictions well. Notably, at x=1000 μm, the model predicts a much lower value for cell density for 100 μm and 50 μm capillary channels – 0.65 and 0.37, respectively.

However, the measured LIVE/DEAD data matches both of these values well as can be seen in Figures 4.10 and 4.11.

4.10 Overview and Conclusions

This chapter outlined the parameters that needed to be included in the model based on a comprehensive literature review and model sensitivity analysis. Based on the established list of parameters, the model was constructed and verified against:

- An independent set of dissolved oxygen data as presented in Sections 4.7 and 4.8
- An independent set of LIVE/DEAD data as presented in Chapter 2 (Figure 2.6) and discussed further in Section 4.9

Thus, the above evidence and the fact that model predictions closely track measured dissolved oxygen and cell density data, allows one to conclude that the model, along with the established parameters, indeed closely predicts physical reality. Furthermore, through the experiments summarized in this section, it has been shown that the model can be used as predictive tool for future oxygen microgradient experiments.

Chapter 4 References

1. P.G. Arthur, J.J. Giles & C.M. Wakeford, "Protein synthesis during oxygen conformance and severe hypoxia in the mouse muscle cell line C2C12," Biochimica et Biophysica Acta 1475, 83-89, 2000.
2. J.Tam, D.Fukumura & R.K. Jain, "A Mathematical Model of Murine Metabolic Regulation by Leptin: Energy Balance and Defense of a Stable Body Weight," Cell Metabolism 9, 52–63, 2009.
3. J.P. Kirkpatrick, D.M. Brizel & Mark W. Dewhirst, "A Mathematical Model of Tumor Oxygen and Glucose Mass Transport and Metabolism with Complex Reaction Kinetics," Radiation Research 159, 336-344, 2003.
4. D.K. McMahon et al, "C2C12 cells: biophysical, biochemical, and immunocytochemical properties," Americal Journal of Physiology 266, C1795-C1802, 1994.
5. M.S. Jafri, S.J. Dudycha & B. O'Rourke3, "Cardiac Energy Metabolism: Models of Cellular Respiration," Annual Review of Biomedical Engineering 3, 57–81, 2001.
6. S.H. Kim, J.H. Kim, E.W. Hahn & N.A. Ensign, "Selective Killing of Glucose and Oxygen-deprived HeLa Cells by Hyperthermia," Cancer Research 40, 3459-3462, 1980.
7. J. Orczyk, D. M. Morre & D. J. Morre, "Periodic fluctuations in oxygen consumption comparing HeLa (cancer) and CHO (non-cancer) cells and response to external NAD(P)+/NAD(P)H," Molecular and Cellular Biochemistry 273, 161–167, 2005.
8. C.B. Allen, B.K. Sschneider & C.W. White, "Limitations to oxygen diffusion and equilibration in in vitro cell exposure systems in hyperoxia and hypoxia," American Journal of Physiology 281, L1021–L1027, 2001.
9. G.M. Saidel, J.A. DiBella & M.E. Cabrera, "Metabolic system dynamics: lumped and distributed models," Simulations in Biomedicine V. Eds. Z.M. Arnez et al., WIT Press, 100-110, 2003.
10. N. Lai, G.M. Saidel, B. Grassi, L.B. Gladden and M.E. Cabrera, "Model of oxygen transport and metabolism predicts effect of hyperoxia on canine muscle oxygen uptake dynamics," Journal of Applied Physiology 103, 1366–1378, 2007.
11. T. Saito et al, "Oxygen consumption of cell suspension in a poly(dimethylsiloxane) (PDMS) microchannel estimated by scanning electrochemical microscopy," Analyst 131, 1006–1011, 2006.
12. T. Schunck and P. Poulet, "Oxygen consumption through metabolism and photodynamic reactions in cells cultured on microbeads," Physics in Medicine and Biology 45, 103–119, 2000.
13. A. Rotem et al, "Oxygen Is a Factor Determining In Vitro Tissue Assembly: Effects on Attachment and Spreading of Hepatocytes," Biotechnology and Bioengineering 43, 654-660, 1994.
14. T. Ma, S. Yang & D.A. Kniss, "Oxygen Tension Influences Proliferation and Differentiation in a Tissue-Engineered Model of Placental Trophoblast-Like Cells," Tissue Engineering 7, 495-506, 2001.
15. J.M. Gray et al, "Oxygen sensation and social feeding mediated by a C. elegans guanylate cyclase homologue," Nature 430, 317-322, 2004.

16. K. Mehta, G. Mehta, S. Takayama & J. Linderman, "Quantitative Inference of Cellular Parameters From Microfluidic Cell Culture Systems," Biotechnology and Bioengineering 103, 966-974, 2009.
17. F. Zhao, P. Pathi, W. Grayson, Q. Xing, B.R. Locke & T. Ma, "Effects of Oxygen Transport on 3-D Human Mesenchymal Stem Cell Metabolic Activity in Perfusion and Static Cultures: Experiments and Mathematical Model," Biotechnology Progress 21, 1269 - 1280, 2005.
18. R.M. Rivera, G.M. Dahlgren, L. Augusto de Castro e Paula, R.T. Kennedy & Peter J Hansen, "Actions of thermal stress in two-cell bovine embryos: oxygen metabolism, glutathione and ATP content, and the time-course of development," Reproduction 128, 33-42, 2004.
19. M. Radisic, W. Deen, R. Langer & G. Vunjak-Novakovic, "Mathematical model of oxygen distribution in engineered cardiac tissue with parallel channel array perfused with culture medium containing oxygen carriers," American Journal of Physiology Heart and Circulatory Physiology 288, H1278-H1289, 2005.
20. M.R. Antoniewicz et al, "Evaluation of regression models in metabolic physiology: predicting fluxes from isotopic data without knowledge of the pathway," Metabolomics 2, 41-52, 2006.

CHAPTER 5

CONCLUSIONS AND FUTURE WORK

This thesis presents a high-throughput method for *in vitro* generation and studies of oxygen microgradients. This chapter provides a summary of work that has been completed; it also outlines future potential extensions of this work.

5.1 Conclusions and Summary of Contributions

Contributions from completed work include:

- Development of the proposed method and procedural protocols
- Development and demonstration of the structures used for the proposed method along with their fabrication processes
- Characterization of the method with cell viability, pH, differentiation and oxygen measurements
- Development of a metabolic and mass transfer model that correlates the obtained data

These contributions provide the research community with the framework for generating oxygen microgradients *in vitro* while overcoming many limitations with existing methods.

The developed method accelerates the throughput of oxygen microgradient experiments by a factor of 15 to 30 and, furthermore, enables experiments that until now were not possible at all such as those described in this chapter.

In addition, this work also lays the foundation for a second generation of this method and associated devices – that is, integrated microsystems that will result in the production of components such as reservoirs, pumps, valves and channels within a single batch-fabricated process. This next level of integration will further increase fabrication yield, dimensional accuracy and experimental consistency.

The method is likely to accelerate the speed with which the scientific community studies the effects of oxygen microgradients on cell culture and, therefore, will enhance the understanding of oxygen's effects on disease and cell development. This will, in turn, lead to new developments in emerging areas such as tissue engineering, adult stem cell therapies and cancer research. Specific areas of further study are provided in Section 5.3 below.

5.2 Method Limitations and Potential Improvements

While the new method was successfully demonstrated to overcome the limitations of other techniques for oxygen microgradient generation, the procedures and protocols are still mostly manual procedures and can be further improved by improving and automating the following:

- Optimize bonding technique used during fabrication to maximize device yield from the current 25%; most of the present device failures occur due to leaking and poor bond between the glass and SU-8 in the process described in Section 3.6
- Improve the cell loading technique to control the seeding densities in the different channels; the current design only accommodates a single initial density for all channels, such as 80%

- Improve the cell culture technique to accommodate periodic perfusions to allow longer experiments and easier introduction of reagents into the channels; the longest experiment conducted with the developed method was approximately 7 days
- Allow for continual and automated measurements of oxygen to be able to easily perform time-lapse studies; currently oxygen measurements are taken manually and one at a time and this is the main remaining bottleneck that needs to be removed to accelerate the data collection process by a factor for 10-20. Additionally, for multiple day experiments, the experimenter will not need to continually come back to the lab to record data
- Improve the sensitivity of the oxygen fiber optic probe to reduce channel sizes and enhance spatial resolution of the method from the current 1mm to less than 50μm; this could be accomplished by embedding oxygen sensing probes in the channels directly

As demonstrated with the integrated device structures described in Chapter 3, this method can be further integrated with batch fabricated microfluidic components. The advantages of such integration will further enhance this method by improving experimental yield and throughput, and by allowing for a wider range of experiments by precisely controlling the microfluidic flows.

To design the microfluidics of the second-generation chip, simulations can be used to predict the flow of cell-media suspension during initial loading and subsequent cell culture. A few examples of potential designs are shown in Figure 5.1 below.

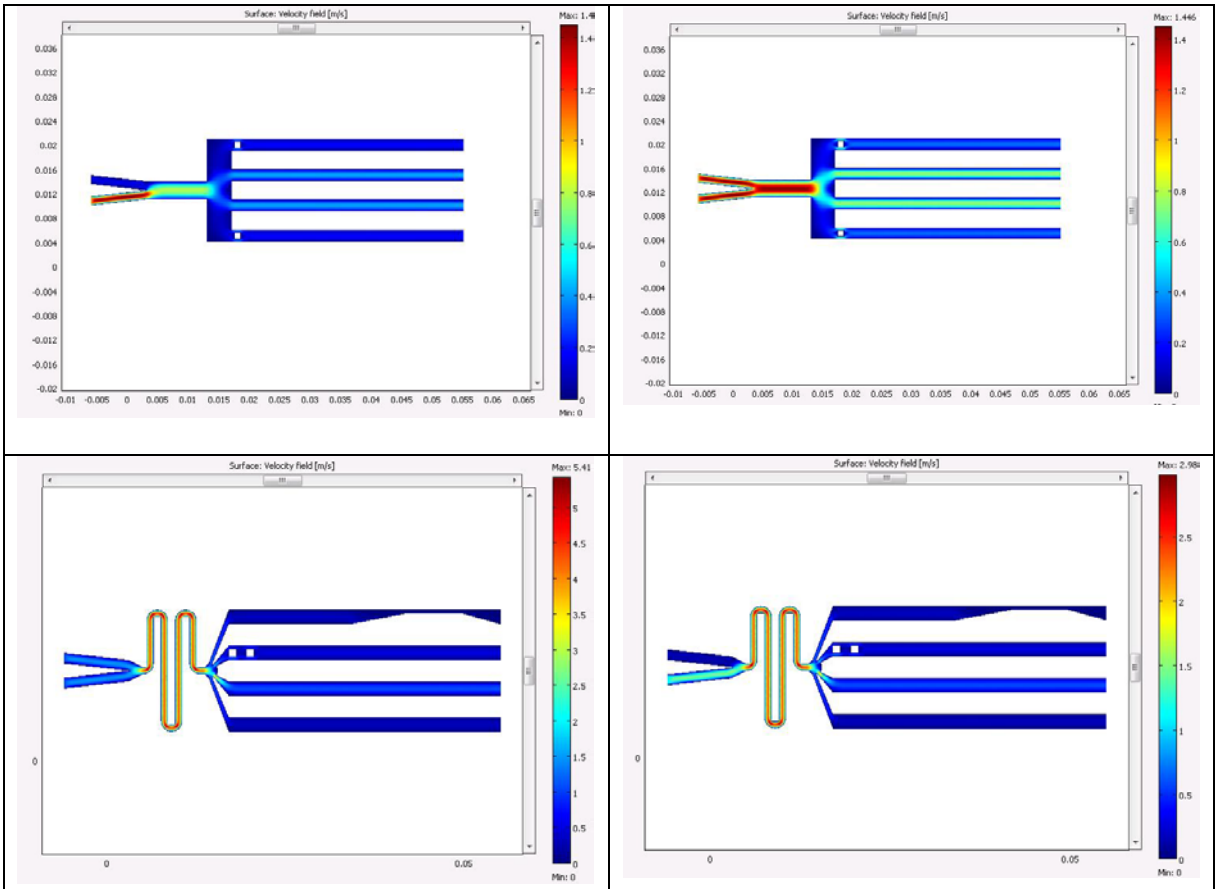

Figure 5.1: Examples of microfluidic chip designs and simulations performed in COMSOL simulation software (Burlington, Massachusetts) for a second-generation batch fabricated integrated device. These designs and simulations show how the initial cell-media suspension can be loaded into the channels and then perfused during culture, if necessary. Simulations can also enable allow one to produce density-graded loading of cells into channels. In these sample simulations, one can test the flows during asymmetric two-port loading (top left), symmetric two-port loading (top right) as well as symmetric (bottom left) and asymmetric (bottom right) loading with channels that are designed to produce graded flows and correspondingly, varying initial cell density distributions.

As part of potential improvements and future work, second generation integrated devices should be implemented to produce the full MEMS-style integration. For example, prior to entering the capillaries, the flow can be controlled with valves, pumps and mixers. In addition, mixers can expand the scope of experiments that can be performed since other chemical gradients could be generated orthogonally to the oxygen gradients described below. Specifically, the following list of second-generation device features is proposed:

- built-in oxygen sensors: to measure dissolved oxygen continually
- differential seeding of cells: to vary cell density in capillary channels during the same experiment
- orthogonal gradients: to flow various ECM and surface attachment proteins prior to seeding the capillary channels with the cells
- shear stress variation: to study effects of shear stress on cells and compare how exposure to shear stress affects cells during hypoxic and normoxic conditions
- cell co-culture: to monitor the interaction of normal and cancer cells during normoxic and hypoxic conditions
- thermal gradients: to better understand how temperature affects cells during hypoxia
- 3D pits: to conduct oxygen microgradient experiments within a 3D cell culture

5.3 Other Future Work

In addition to expanding the general set of features of the integrated microgradient devices, a specific set of experiments with implications for cancer research is proposed and described below. Specifically, previously reported work from as early as 1909 has shown that tumor cells are resistant to radiation treatment [1]. Such radiation resistance of tumor cells in hypoxic regions of tissue was confirmed with a number of studies and a principle known as the O_2 enhancement effect was established [2]. Here, the increased presence of O_2 was thought to damage the DNA through the formation of free radicals; in hypoxic regions, there was less O_2 and, therefore, fewer free radicals, and that resulted in less damage to the cells. There was a significant amount of evidence in the 1950s and

1960s to suggest that hyperbaric oxygen treatments and red blood cell transfusions could improve the effectiveness of cancer radiation treatments by increasing oxygen concentrations in tumor regions. While initial clinical trials resulted in conflicting outcomes, these approaches are now being revisited again [3].

A desirable set of experiments could utilize the method presented in this thesis to investigate the hypoxic radiation resistance of various types of cancer cells subjected to varying amounts of radiation in a high-throughput manner as described in this thesis; such high-throughput studies could yield conclusions about the optimal amounts of oxygen and radiation to destroy tumor cells. These conclusions, in turn, will have therapeutic implications that can be used in clinical trials to establish optimal protocols for treatment of various cancers with specific doses of radiation and oxygen. In these experiments, chemotherapeutic agents can be introduced as well.

Another important area of future experiments should be with hypoxia-activated drugs. An example of such a drug is Tirapazamine, which was described over 20 years ago [4]. Tirapazamine is only activated in a hypoxic environment and releases agents that kill the nearby cells [5]. Recent clinical trials with Tirapazamine have demonstrated benefits with patients with head and neck [6] and lung cancer [7]. An organized study that utilizes the high-throughput properties of the developed method could identify optimal amount of hypoxia-activated drugs such as Tirapazamine for various types of cancers.

Taken together, these two comprehensive studies could yield results to establish optimal amounts of radiation, chemotherapy, oxygen and hypoxia-activated drugs to treat various human cancers.

Chapter 5 References

1. G. Schwarz, "Ueber Desensibilisierung gegen rontgenund radiumstrahlen," *Munchener Medizinische Wochenschrift* 24, 1–2, 1909 (in German)
2. L. H. Gray et al, "The concentration of oxygen dissolved in tissues at the time of irradiation as a factor in radiotherapy," *The British Journal of Radiology* 26, 638–648, 1953.
3. J. Overgaard et al, "Hypoxic radiosensitization: adored and ignored," *Journal of Clinical Oncology* 25, 4066–4074, 2007.
4. E. M. Zeman et al, "SR-4233: a new bioreductive agent with high selective toxicity for hypoxic mammalian cells," *International Journal of Radiation Oncology Physics* 12, 1239–1242, 1986.
5. J. M., Brown et al, "Exploiting tumour hypoxia in cancer treatment," *Nature Reviews Cancer* 4, 437–447, 2004.
6. D. Rischin et al, "Tirapazamine, cisplatin, and radiation versus fluorouracil, cisplatin, and radiation in patients with locally advanced head and neck cancer: a randomized phase II trial of the Trans-Tasman Radiation Oncology Group (TROG 98.02)," *Journal of Clinical Oncology* 23, 79–87, 2005.
7. von Pawel, J. et al, "Tirapazamine plus cisplatin versus cisplatin in advanced non-small-cell lung cancer: A report of the international CATAPULT I study group. Cisplatin and Tirapazamine in Subjects with Advanced Previously Untreated Non-Small-Cell Lung Tumors," *Journal of Clinical Oncology* 18, 1351–1359, 2000.

Appendix A

Cell Culture and Microfluidics Background

1.1: Glossary

Aerotaxis: An organism's movement toward or away from oxygen as a reaction to its presence. The term is most often used when discussing aerobes (oxygen-using) versus anaerobes (which don't use oxygen).

Chemotaxis: a kind of taxis, is the phenomenon in which bodily cells, bacteria, and other single-cell or multicellular organisms direct their movements according to certain chemicals in their environment. This is important for bacteria to find food (for example, glucose) by swimming towards the highest concentration of food molecules, or to flee from poisons (for example, phenol). In multicellular organisms, chemotaxis is critical to early (e.g. movement of sperm towards the egg during fertilization) and subsequent phases of development (e.g. migration of neurons or lymphocytes) as well as in normal function. In addition, it has been recognized that mechanisms that allow chemotaxis in animals can be subverted during cancer metastasis.

Electrochemical gradient: a spatial variation of both electrical potential and chemical concentration across a membrane. Both components are often due to ion gradients, particularly proton gradients, and the result can be a type of potential energy available for work in a cell. This can be calculated as a thermodynamic measure termed electrochemical potential that combines the concepts of energy stored in the form of chemical potential, which accounts for an ion's concentration gradient across a cellular membrane, and electrostatics, which accounts for an ion's tendency to move relative to the membrane potential.

HeLa cell line: an immortal cell line used in medical research. The cell line was derived from cervical cancer cells taken from Henrietta Lacks, who died from her cancer on October 4, 1951.

Laminar flow: sometimes known as streamline flow, occurs when a fluid flows in parallel layers, with no disruption between the layers. In fluid dynamics, laminar flow is a flow regime characterized by high momentum diffusion, low momentum convection, pressure and velocity independent from time. It is the opposite of turbulent flow. In nonscientific terms laminar flow is "smooth," while turbulent flow is "rough."

Mass transfer: phrase commonly used in engineering for physical processes that involve molecular and convective transport of atoms and molecules within physical systems. Mass transfer includes both fluid flow and separation unit operations.

Molecular diffusion: often called simply diffusion, is a net transport of molecules from a region of higher concentration to one of lower concentration by random molecular motion. The result of diffusion is a gradual mixing of material. In a phase with uniform temperature, absent external net forces acting on the particles, the diffusion process will eventually result in complete mixing or a state of equilibrium. Molecular diffusion is typically described mathematically using two Fick's laws.

Transport phenomena: in physics, chemistry, biology and engineering, any of various mechanisms by which particles or quantities move from one place to another. The laws which govern transport connect a flux with a "motive force". Three common examples of transport phenomena are diffusion, convection, and radiation. The science of transport phenomena is a great complement to rheological study of Newtonian fluids.

Reynolds number / Re: in fluid mechanics and heat transfer, a dimensionless number that gives a measure of the ratio of inertial forces to viscous forces and, consequently, it quantifies the relative importance of these two types of forces for given flow conditions. Laminar conditions apply up to Re = 10, fully turbulent from 2000.

Sources for definitions: online and print publications.

1.2: Microfluidics Background

MEMS, or micro electro mechanical systems, have been in development since 1970s and are now blossoming with a variety of mass market applications. The scope and variety of MEMS and microfabrication techniques are continually expanding and improving. In particular, MEMS fabrication technologies have led to the emergence of microfluidic applications – in other words, applications where microliters and even nanoliters of fluids, which can be liquid or gas, are manipulated in channels, interconnections and integrated control devices such as valves and pumps.

A natural question to ask is – why miniaturize fluidic devices? Here are some of the main advantages:

- Reduced amounts of reagents
- Domination of diffusion (vs. convection) in mass transfer
- Laminar (vs. turbulent) flow regime
- High throughput capabilities
- Miniaturized diagnostics and drug delivery

- Scales that are relevant for investigation of individual cells or small numbers of cells

Overall, microfluidics can be thought of as a set of technologies to make devices which address scientific and commercial applications where fluidic miniaturization is necessary.

The focus of the work presented in my thesis mainly takes advantage of the last of the above points – in other words, my goals and presented results have been oriented towards re-creating biological microgradients on the relevant scales *in vitro*.

1.2.1: Basic Microfluidic Theory

As introduced in the previous section, the advantages of microfluidics mainly stem from physical phenomena scaling with size – for example, the laminar flow regime allows for controlled and predictable mixing of fluids because diffusion dominates and convection is negligible. In this section, rather than repeat the microfluidic theory readily available from a number of canonical sources, only concepts that are most relevant to my results and contributions are presented.

1.2.2: Reynolds Number

The dimensionless Reynolds number is a relative ratio of inertial forces to viscous forces. A low Reynolds number corresponds to laminar flows where viscous forces dominate whereas a high Reynolds number corresponds to turbulent flows where the dominant contribution comes from inertial forces. Most *in vivo* biological flows are in

the laminar regime and even the blood flow in the aorta has a Reynolds number of ~10^3 which is still not enough to develop turbulence which occurs at ~10^4 in pipe flows.

1.2.3: Diffusion

Since diffusion, and not convection, usually dominates mass transfer in microfluidics, it is useful to provide some basic diffusion background and relevant examples. For steady state diffusion, Fick's first law given by the following expression is usually used:

$$J = -D \nabla C$$

Here, J is diffusion flux, D is the diffusivity, C is the concentration of diffusing substance and ∇C is the gradient, or the vector field whose components are the partial derivatives of C. In other words, the flux of diffusing substance is directly proportional to its diffusivity and the differences in concentration of that substance in space.

A useful expression to estimate the time necessary for a substance to diffuse is:

$$x^2 = 4 D t$$

where x is how far the substance has propagated in one dimension, D is the diffusivity and t is the time.

Diffusivity is proportional to the velocity of the particles of the diffusing substance. Velocity, in turn, depends on temperature, size of the particles and fluid viscosity. For example, diffusivities of ions in aqueous solutions are on the order of ~10^{-9} m^2/s; for biological molecules, such as proteins, diffusivities are usually in the range of ~10^{-11} to ~10^{-10} m^2/s.

1.2.4: Sizes of Relevant Objects

It is useful to list approximate sizes of cells and other objects described in the results of this work:

- Small molecule (such as O_2): ~10^{-9} m
- DNA: ~10^{-8} m
- Viruses: ~10^{-8} to10^{-7} m
- Bacteria: ~10^{-6} m
- Mammalian Cell: ~10^{-5} m
- Hair: ~ 10^{-4} m

My results report on experiments with *Escherichia coli* (~1-2 μm) and *Bacillus subtilis* (~5 μm) bacteria as well as HeLa cancer cells (~20 μm) and C2C12 muscle precursor cells (~20 μm).

1.2.5: Surface Properties

Although a variety of surface properties are relevant for microfluidic applications, one of the most important ones is the hydrophobicity of the surface. Simply put, hydrophobicity of the surface determines whether or not aqueous solutions are repelled or attracted by a particular surface. Since water is a polar molecule, surfaces that are made up of polar molecular groups are called hydrophilic; surfaces that have non-polar groups are called hydrophobic. Polydimethylsiloxane, or PDMS, is probably the most ubiquitous material for making microfluidic devices and is naturally non-polar and, therefore, hydrophobic. Glass, another popular material, is usually hydrophilic. This is important because small channels made from PDMS may not be able to carry aqueous

solutions unless PDMS is temporarily rendered hydrophilic with the oxygen plasma or relevant surfactants.

1.3: State-of-the-art Technologies for *In Vitro* Microgradient Generation

Basic microgradient generation techniques such micropipettes were already available in late 19th century. A few more relatively primitive techniques such as the Boyden and Dunn chambers were introduced in the 1960s and over the next few decades. However, the ongoing revolution catalyzed by the emerging microfabrication technologies introduced a variety of much more powerful set of devices. In this section, I briefly review state-of-the art techniques beginning with the micropipettes and through a much more varied set of modern technologies.

1.3.1: Micropipettes

The earliest applications of micropipettes date back to the late 19th century. To generate the gradient, liquid is pumped through the micropipette via backpressure and the substance is pumped out into the general media through the pipette tip.

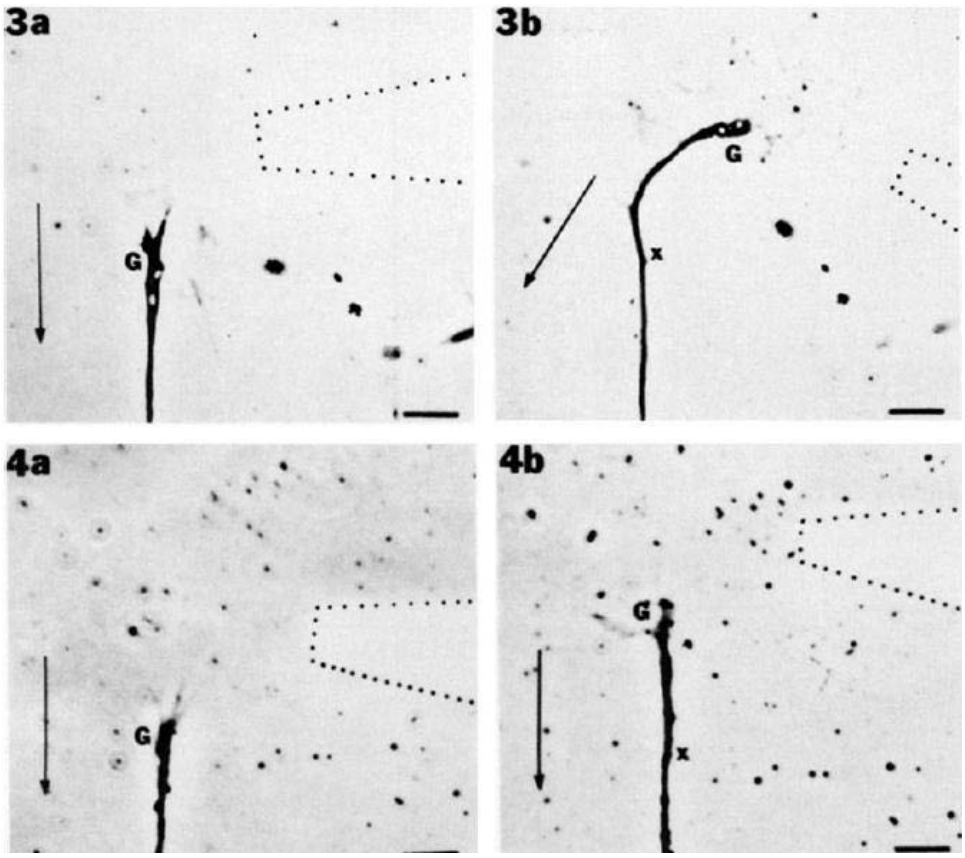

Appendix Figure 1: An example of an early micropipette application where a micropipette (dotted line) is used to guide the growth of a neurite (G) [1]

Applications have included neural cell guidance where cells followed the chemoattractants ejected from the pipette tip as it was moved around the culture dish [1]. Not surprisingly, the crude set up of the micropipettes suffered from lack of control of ejected material as well as the instability of produced gradients – as material was ejected from the pipette, the gradient profile changed and the pipette had to be manually moved to keep an approximately similar gradient profile.

1.3.2: Boyden Chamber

In this setup, one smaller chamber is placed into a larger chamber and the two chambers are separated by a semipermeable membrane through which cells can migrate in response to the differences in concentrations of a chemoattractive substance in the upper and lower chambers [2]. One of the advantages of the Boyden chamber is that it can distinguish between chemotactic and chemokinetic effects – that is, one can determine the direction and *speed* of cell movement.

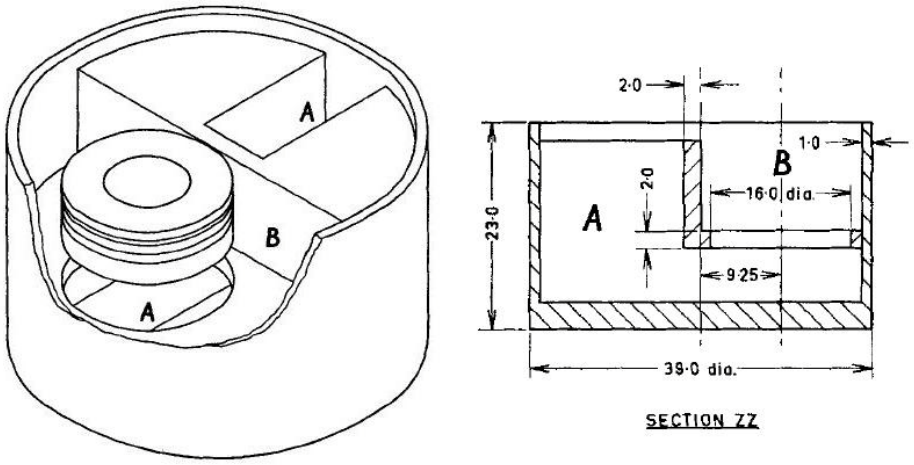

Appendix Figure 2: The original design of Boyden's chamber; reservoirs A and B are separated by a semipermeable membrane through which cells can migrate [2].

One of the limitations of the Boyden chamber is that is requires that the cells of interest be able to attach to the membrane surface. In addition, cells must be biocompatible and be of an appropriate size to migrate through the semipermeable membrane. Another important limitation of the Boyden chamber is that the established gradient is not on the micro scale. Also, cells cannot be observed during their migration through the membrane.

1.3.3: Zigmund-Dunn Chamber

In this scheme, two or more chambers with different substances are connected via a shallow bridge and a relatively stable gradient is established due to the diffusion of substances from the chambers into the bridge. Cells can be seeded on the bridge's surface and can migrate and be observed via a microscope positioned right above or below the bridge. Another variation of the Zigmund chamber, where reservoirs are simply connected side-by-side horizontally, is the Dunn chamber where interconnected concentric rings are used.

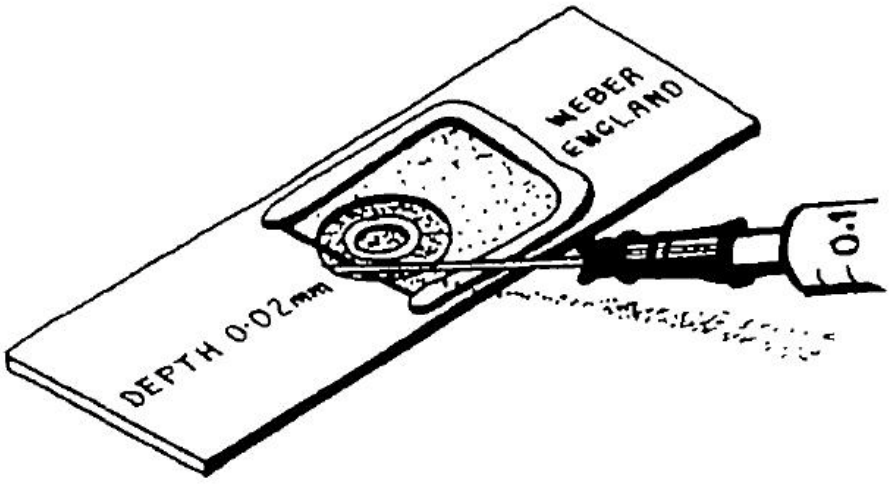

Appendix Figure 3: The original Dunn chamber [3].

In some cases, the connecting bridge is filled with agar or other three-dimensional bio-derived and synthetic materials through which cells can migrate.

1.3.4: Microfluidic and MEMS Techniques

While most of the MEMS and microfluidic gradient generation techniques are based on the traditional methods mentioned above, they bring the much-needed miniaturization. A number of comprehensive reviews published in the past few years provide excellent

overviews and perspectives on the state-of-the-art technologies. In particular these reviews discuss important aspects such as:

- Microscale technologies for tissue engineering [5]
- Chemical reactions in microfluidic systems [6]
- Systems biology applications in microfluidics [7]
- Microfluidic and lab-on-a-chip applications for single cell analysis [8,9,12]
- Interactions between cells, substrates and interfaces [10,11]
- Microfluidic applications in neurobiology [13]

In all of these reviews, microgradient generation is an important part of the modern technology tool set and many of the latest techniques are described. In the following sections, the currently available techniques are organized into categories by device type and provide a few examples of applications and results obtained with these devices.

1.3.4.1: Microfluidic Multistep Mixers

Whitesides *et al* introduced and demonstrated the microfluidic multistep mixer-gradient concept with their seminal paper in 1999 [14]. In this set of devices, two or more miscible liquids are injected into the inlet ports and then are diffusively mixed while being pumped through a network of channels resembling a Christmas tree. Since the flows are in the laminar regime, and therefore cannot mix convectively, the "serpentine" branching network is necessary to provide enough time for the flows to mix diffusively. After the flows are mixed, they are recombined and a linear gradient is formed. As a consequence of this initial work by the Whitesides group, the concept has

been used in at least 100 similarly structured devices, many with their own set of published results.

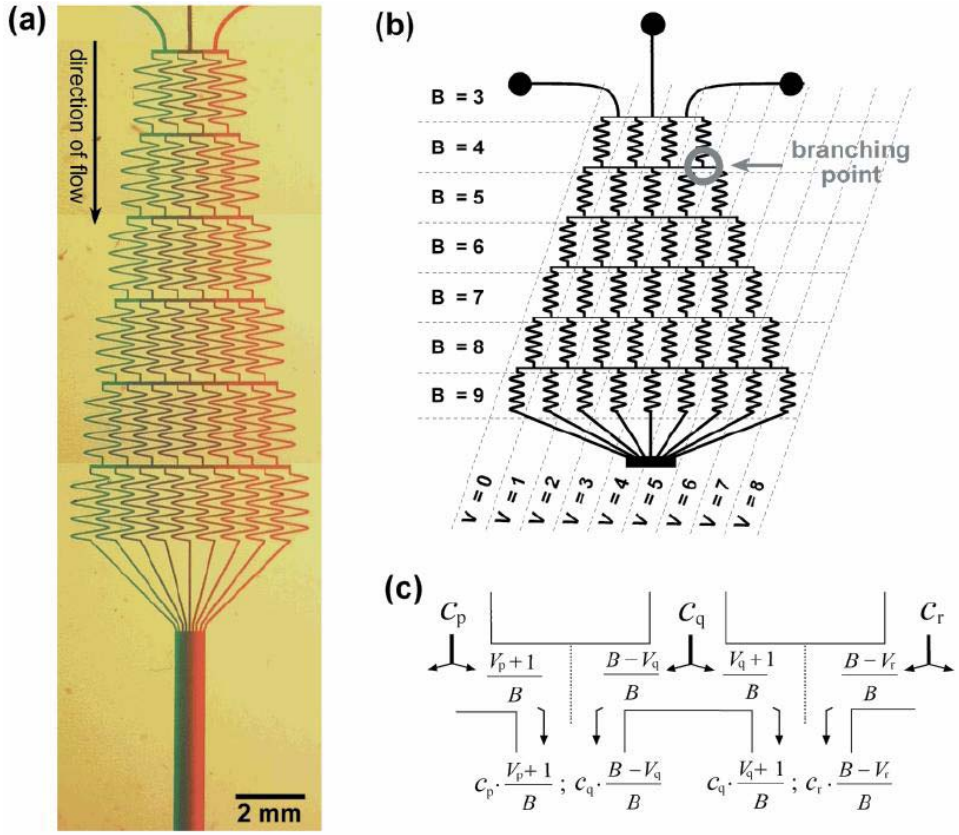

Appendix Figure 4: The original demonstration of flow-based multichannel gradient generator shown here with color dye (A); the multistage branching allows for diffusive mixing (B,C) [14].

The main limitation of these types of devices is the necessity of flow. Thus, only attachable cells can be studied and shear stress will always be a factor in the experiments. Also, it turns out that the amount of flow affects the stability of the gradient. In other words, too much or too little flow can affect the shape of the gradient. Additionally, setup is more complicated since the necessary flow requires the inclusion of syringe pumps and other equipment to maintain the gradient. This can make experiments

especially cumbersome for cell culture applications where cells of interest must be in an environmentally controlled incubator during the course of the experiment. Yet another limitation of this device is that the gradient cannot be switched or controlled rapidly.

Still, there have been a number of notable results using this setup and also a number of interesting improvements have recently been introduced.

Some of the examples of recent results and studies with these types of devices include:

- Jeon *et al* followed up the original work in the Whitesides group by conducting experiments with neutrophil migration in 2002 [15]. This work itself became a seminal paper and generated more than 100 citations to date.
- Irimia *et al* have recently presented a method which, unlike earlier works, utilized pressure controlled valves to rapidly switch the orientation and steepness of the gradient profile to show response of neutrophils to a known chemoattractant interleukin-8 (IL-8) [16]. As a result of this work, it is now possible to measure responses of cells to temporal changes in the gradient profile.
- Saadi *et al* presented experiments which explored human cancer cells in response to epidermal growth factor, or EGF [17]. The study has implications for better understanding of cancer metastasis where growth factors may induce cells to migrate from the tumor area to other sites in an organism.
- Campbell *et al* presented an alternative architecture for the traditional Whitesides device with two advantages: it can generate monotonically increasing profiles of *any shape* and it reduces the number of mixing serpentine channels by an order of magnitude which, in turn, reduces the device size [18].

- Gunawan *et al* explored the effects of extra cellular matrix, or ECM, proteins on the migration of rat intestinal cells [19]. Their findings revealed that while cells migrated against the gradient independent of steepness, the cells' directedness decreased at high attractant levels.
- Rhee *et al* used gravitational and centrifugal forces to align cells in the same starting position within microfluidic channels and then applied the gradient in a Whitesides-type device so that they would be exposed to the same starting concentration of chemoattractants [20]. One of the notable accomplishments of this work is that it resolved one of the limitations of the original devices where cells were randomly seeded throughout the width of the channel and were exposed to different concentrations and gradients.
- Khademhosseini *et al* demonstrated a scheme where fibroblast and embryonic stem cells were deposited in micromachined microwells and then reagents were introduced in orthogonally oriented channels [21]. The authors suggested that the resulting grid of the various types of cells could then be exposed to gradients formed by a Whitesides-type device to study these multiphenotype cell arrays.
- Herzmark *et al* was one of the first results to explore chemotactic prowess while keeping the fractional difference in concentration constant [22]. The authors accomplished this with exponential gradients generated in a Whitesides-type device. The study confirmed that as long as chemoattractact concentration is near the constant of its dissociation cells migrate more effectively across the gradient.
- Song *et al* presented experiments that tested chemotactic response of *Dictyostelium discoideum* cells to linear gradients of cAMP [23]. Interestingly,

chemotactic speed was optimal at a specific gradient range; if the gradient was too shallow or too steep, cells did not show directional response. In the optimal gradient regime, the difference in receptor occupancy between front and back of a cell was estimated to be only around 100 molecules.

- Wei *et al* demonstrated a co-culture of stimulated and unstimulated microphages in the upstream portion of the device and then set up a linear gradient of inflammatory cytokines downstream, where osteoblasts were shown to have a corresponding variation in their protein expression [26].

A number of relevant modeling papers for this device architecture have also been recently published. For example:

- Sager *et al* presented their results in a modeling paper on passive microfluidic mixing networks such as the Whitesides scheme [24]. Their model shows that gradients formed by these types of microfluidic networks can be described by polynomials of the order that is one less than the number of input ports. For example, with three input ports one can obtain linear and parabolic gradient profiles.
- Wang *et al* presented a lumped element model for the flow-based gradient generation networks and proposed to combine some of the existing devices with their geometries to form more complex gradient profiles [25].

1.3.4.2: Other Flow Based Gradient Generation Devices

Although the scheme presented by Whitesides *et al* has been the most popular flow based gradient generation device, other interesting flow based approaches have been presented and successfully demonstrated. Here are some of the notable examples:

- Li *et al* generated linear, concave and convex chemical gradients by offsetting the pressure difference in two main channels of an interconnected ladder structure by a constant amount and also varying the length of the connecting microtunnels [37]. This architecture can also be applied for high-throughput cell density arrays.

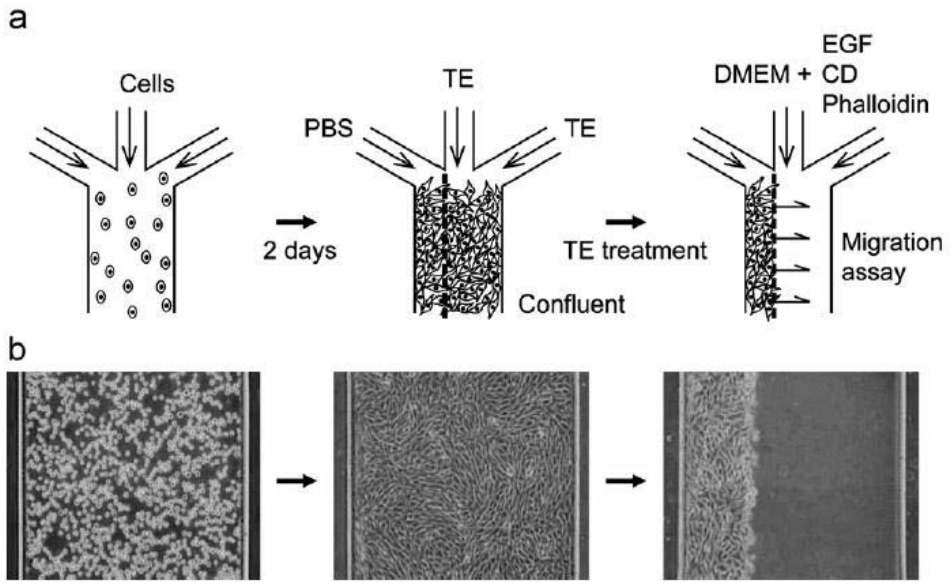

Appendix Figure 5: An example of a flow-based microfluidic scheme to create simulated wound edges with trypsin. A schematic showing the principle of operation (a) and actual results showing initial seeding (b, left), attachment (b, center) and after patterning with trypsin (b, right) [40].

- Yamada *et al* demonstrated how a set of T-junctions connected in parallel can generate a linear gradient [38]. In contrast to the Whitesides-type devices, the authors showed that this scheme can generate linear gradients of miscible liquids *independent* of flow rates. The device was also demonstrated with yeast cells

where growth rate was proportional to the amount of viable media in solution across the linear gradient.

- Hsu *et al* presented a way to generate complex gradient profiles that do not require a large number of mixing channels [39]. This device can also form gradients that can be smoothly varied in time without significantly altering the flow rate.
- Nie *et al* demonstrated a clever method for setting up migration assays with trypsin laminar flows of three virtually separated streams [40]. This assay used flow based approach to mimic biological wounding that occurs *in vivo*. The system was demonstrated with chemoattractants in the same channels.
- Irimia *et al* presented a systematic approach for generating stable gradients of any profile [41]. The authors also presented a mathematical proof for their claim and examples were demonstrated.
- Lin *et al* demonstrated a simple, and less cumbersome technique than Whitesides', flow based gradient generation method based on a Y-shaped junction [42]. The device was used to generate linear gradients of CCL19 and CXCL12 chemokines to study T cells' response to the established gradients. Notably, the simple geometry also allowed for rapid switching of gradient profiles.

1.3.4.3: Micro Dunn Chambers

The Dunn and Zigmung chambers were especially good candidates for miniaturization because diffusion dominates on the micro scale and gradient profiles can be predicted with relatively simple models. The basic principles of this approach are to

have two or more reservoirs connected by a channel in which diffusively formed gradients are generated and studied with cells of interest. In particular, Beebe's group (Univ. of Wisconsin) has done much interesting work in this area – their recent work, along with a few notable others, are summarized below:

- Abhyankar and Beebe successfully combined micro Dunn chambers and cell patterning techniques to explore spatiotemporal positioning of cells and beads into diffusion limited microwells [27]. This is a useful method for studying co-culture scenarios with different cells and diffusible reagents.

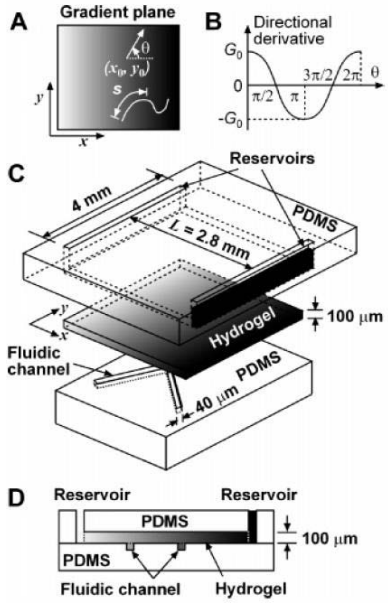

Appendix Figure 6: An example of micro Dunn-type chamber. Here, a hydrogel layer is used for diffusion of chemoattractants and cells are seeded in the channels underneath the hydrogel [28].

- Wu *et al* demonstrated a variation of the standard micro Dunn chamber with hydrogel serving as the medium for diffusion [28]. In their scheme, gradients were formed diffusively in the hydrogel and then cells were observed in channels

of various shapes that were right below the hydrogel layer. The hydrogel offers a number of advantages: it prevents convective flows and forms a physical barrier between cells in the channel and media in the reservoirs.

- Yu *et al* presented diffusion dominant PDMS microchambers to explore the relationship between chamber geometry and cell proliferation [29]. Not surprisingly, the chamber height had the most significant effect on cell proliferation with shallower channels yielding lower rates of cell proliferation. Based on this work, it is clear that the accumulation of cell waste products and other factors can be quite rapid (~5-10 hours) in microchambers and this should be an important consideration in designing experiments.
- Paliwal *et al* studied MAPK adaptive gradient sensing in yeast using a series of Dunn-type microbridges which were connected to two main feeding channels [30]. By varying the length of the microbridges, the authors were able to explore a series of gradient profiles in a parallel and high-throughput manner.
- Chueh *et al* presented a clever way of embedding semiporous polyester and polycarbonate membranes between two layers of PDMS [56].
- Chaw *et al* experimented with micron-sized gaps to study tumor cell migration in response to diffusive gradients of chemoattractants that formed in the gaps connecting three parallel-flow channels [31]. Results of this work seem to suggest that cells have limited flexibility and prefer not move through gaps that are smaller than a specific size, 3μm in this case. Also, the authors were able to extract parameters such as cell migration rates which, in this case, were measured

to be 5-15 μm/hour. Fetal bovine serum, or FBS, was added to standard DMEM media to serve as the chemoattractive agent in this case.

- Nam *et al* explored chemotactic response of freshwater ciliates in a Dunn-type microchamber with pneumatically controlled microvalves [32].
- Saadi *et al* demonstrated stable concentration gradients in two and three dimensions using a microfluidic ladder structure [33]. For the three dimensional scenario, biocompatible gels were used. The authors used their device to show neutrophil chemotaxis in gradients of soluble chemoattractant IL-8.
- Keenan *et al* presented a slightly modified micro Dunn chamber where the reservoirs were pressurized and chemoattractive solutions were forcibly ejected from the reservoirs when the pressure became sufficiently high [34].
- Abhyankar *et al* presented a method to incorporate a semiporous membrane to control the rate of diffusion from the reservoirs [35]. The authors include results which include neutrophil migration across diffusion based gradients.
- Kim *et al* introduced peptide hydrogel for three-dimensional toxicity gradient assays based on diffusion across three virtually separated microfluidic channels [36]. The middle channel had the cells embedded in the three-dimensional hydrogel matrix and the two adjacent channels supplied two different kinds of media which then diffused across the middle channel. The paper argued that peptide hydrogel can serve as a viable material to make biocompatible microenvironments for cell experiments and compared it OPLA, a collagen composite, as well as Puramatrix scaffolds.

1.3.4.4: Microinjectors

The concept behind microinjectors is quite simple – they are basically microfabricated "descendants" of the traditional pipettes. Microinjectors can be controlled by microvalves and inject reagents in a controlled manner into the area of interest which can be pre-seeded with cells. Despite their relatively simple principle of operation, only recently have the available microfabrication technologies reached enough critical mass to produce the first microinjector devices. Here are some of the recent and notable examples:

- Chung *et al* presented a microfluidic adaptation of the traditional pipette [43]. Advantages over traditional pipettes include more precise timing of chemical release and better spatial resolution. The authors demonstrated multiple gradients formed by multi-injectors. As the authors suggested, this technique can be useful with chemotaxis and axon guidance studies.

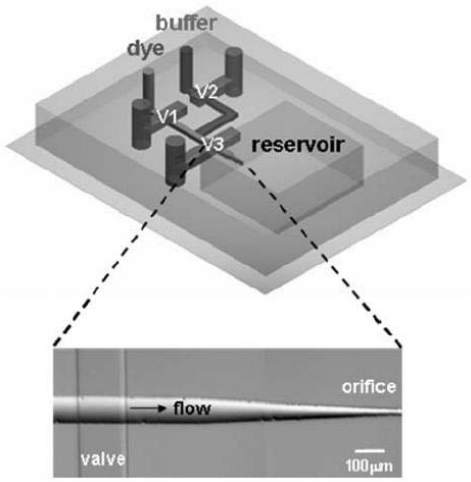

Appendix Figure 7: An example of a microinjector. Valves are actuated by pressurizing the control channel and also act as pumps to generate pulsatile release of solution into the reservoir [43].

- Frevert *et al* presented a device that performs microinjection through a pore which is controlled via a pneumatically operated valve [44]. Neutrophil migration studies were performed with the device.
- Nielson *et al* presented an elegant method where a pulsed laser beam is used to puncture holes in the micron-thick membrane to allow reagents to be injected and thereby form specific gradient profiles [45]. Notably, reagent streams can be blocked by photo-crosslinking a protein plug over selected punctured pores. Thus, this method allows microinjection of chemicals in parallel and onto subcellular targets.

1.3.4.5: Surface Patterning for Gradient Generation

Yet another set of techniques relies on surface patterning to generate the desired gradients. Here, the surface is pre-patterned with the desired reagents and the cells are then seeded onto the surface. In most of these schemes, the pre-patterned surface then eludes the reagents and chemical gradients are formed. Here are some of the recent and notable examples:

- Geissler *et al* presented a method to pattern surfaces using silica beads and PDMS stamps to form chemical gradients with submicron resolution [46]. The gradients formed as reagents diffused via the surface of the beads from the PDMS stamp onto gold surface. The gradient profile can be tuned by time of contact with the stamp, concentrations and bead diameter.
- Hsu *et al* demonstrated a technique to pattern proteins onto surfaces [47]. With their technique they performed endothelial cell migration experiments and studied

haptotaxis with collagen, an ECM protein. They also were able to distinguish between haptotaxis and shear stress, or mechanotaxis, by measurements via immunostaining for focal adhesions and lamellipodial adhesions. Haptotaxis, a directional motility or outgrowth of cells, plays a critical role in vascular remodeling during angiogenesis, embryonic vasculogenesis and wound healing. The authors noted that a Whitesides-type device can be applied to generate gradients of ECM proteins.

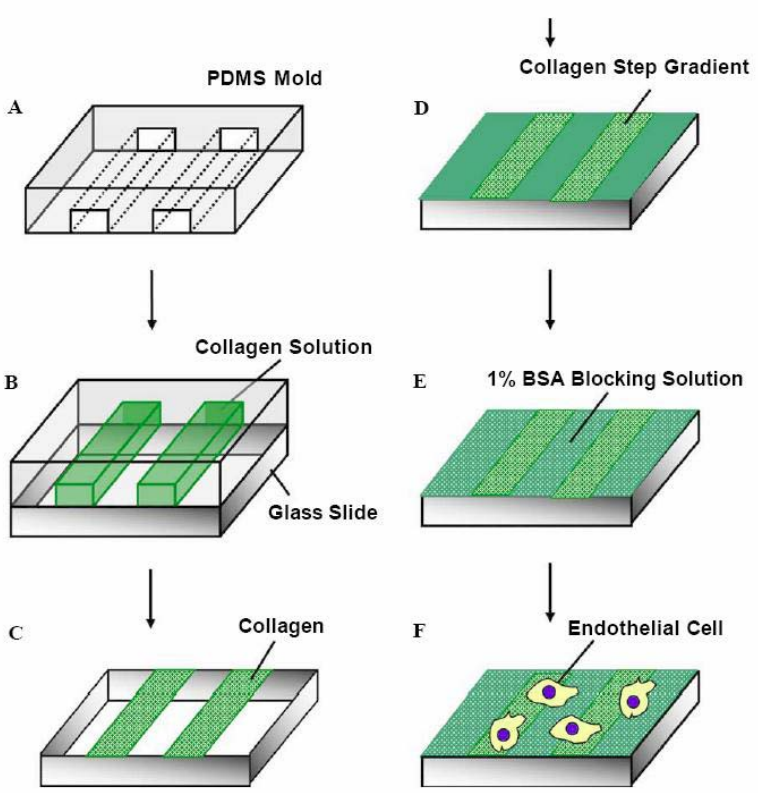

Appendix Figure 8: An example of a process to surface-pattern a micro gradient of a chemoattractant; in this case collagen and endothelial cells were used [47].

- Lee *et al* patterned collagen fibers in alignment using microfluidic flows [48]. Their experiments showed that alignment efficiency depended on channel width

which, in turn, affected the shear stress on the attached cells. For channels of smaller width, collagen aligned more efficiently along one axis. Initial pressure-driven flow also significantly improved alignment efficiency. The experiments also showed that bovine aortic endothelial cells attached and stretched in the direction of the collagen fibers.

- Nakanishi *et al* demonstrated a method to change substrates from non-cell-adhesive to cell-adhesive using UV exposure [49]. This work explored spatiotemporal control of gradients around single cells.
- Mai *et al* proposed a device and technique to study mechanotaxis using surface grid patterning [50]. Unlike other works which presented one-dimensional gradients, this approach allowed the establishment of patterned gradients in two dimensions. The work demonstrated the importance of actomyosin and regulation of local intracellular responses.
- Crozatier *et al* micropatterned surfaces using PDMS stamps on which gradients were formed using flow-through techniques [51].

1.3.4.6: Chemotaxis Modeling

It is useful to mention a few of the recent papers on modeling of chemotaxis. Here are some of the recent works:

- Levine *et al* presented a model for chemotaxis in eukaryotic cells [52]. The paper also summarized state-of-the-art modeling in this area and proposed a mathematical model for how eukaryotic cells, such as neutrophils, can detect a 1% difference in concentration between front and back of a cell.

- Nishimura *et al* presented a model which introduced "inertia-like" chemotactic response where cells could move in the same direction that they have been initially induced to move, even when the gradient is subsequently removed or reversed [53]. This phenomenon was also observed by Jeon and colleagues in their experiments with neutrophil chemotaxis [15].
- Wang *et al* proposed a model that correlates accuracy of transduction and number of receptors [54]. In other words, they provided numerical simulations and proposed a model that relates the number of receptors to measurement accuracy and response time.

1.3.4.7: Electrolytic Gradient Generation

Another notable method to generate gradients is by immersing metal electrodes in an electrolytic solution and then passing current through the electrodes. Depending on the electrolytic solution, various molecular species can be produced at the electrodes. For example, if water is used, then molecular oxygen and hydrogen are produced. The amount of these species can be controlled by the amount of electric current passed through the electrodes and gradients of arbitrary profiles can be established by electrodes of certain geometries. This method was miniaturized and developed by our group [55] and some of the relevant results are presented in later chapters. This method is especially useful for generating gradients of small molecules such as oxygen and hydrogen which can easily diffuse through most microfluidic devices that are usually made from PDMS.

Appendix References

1. R. W. Gundersen, and J. N. Barrett, "Characterization of the Turning Response of Dorsal Root Neurites Toward Nerve Growth-Factor," *Journal of Cell Biology,* vol. 87, no. 3, pp. 546-554, 1980.
2. S. Boyden, "Chemotactic Effect of Mixtures of Antibody and Antigen on Polymorphonuclear Leucocytes," *Journal of Experimental Medicine,* vol. 115, no. 3, pp. 453-&, 1962.
3. D. Zicha, G. A. Dunn, and A. F. Brown, "A New Direct-Viewing Chemotaxis Chamber," *Journal of Cell Science,* vol. 99, pp. 769-775, Aug, 1991.
4. S. H. Zigmond, "Orientation Chamber in Chemotaxis," *Methods in Enzymology,* vol. 162, pp. 65-72, 1988.
5. A. Khademhosseini, R. Langer, J. Borenstein *et al.*, "Microscale technologies for tissue engineering and biology," *Proceedings of the National Academy of Sciences of the United States of America,* vol. 103, no. 8, pp. 2480-2487, Feb, 2006.
6. A. J. deMello, "Control and detection of chemical reactions in microfluidic systems," *Nature,* vol. 442, no. 7101, pp. 394-402, Jul, 2006.
7. D. N. Breslauer, P. J. Lee, and L. P. Lee, "Microfluidics-based systems biology," *Molecular Biosystems,* vol. 2, no. 2, pp. 97-112, Feb, 2006.
8. C. E. Sims, and N. L. Allbritton, "Analysis of single mammalian cells on-chip," *Lab on a Chip,* vol. 7, no. 4, pp. 423-440, 2007.
9. J. El-Ali, P. K. Sorger, and K. F. Jensen, "Cells on chips," *Nature,* vol. 442, no. 7101, pp. 403-411, Jul, 2006.
10. N. Sniadecki, R. A. Desai, S. A. Ruiz *et al.*, "Nanotechnology for cell-substrate interactions," *Annals of Biomedical Engineering,* vol. 34, no. 1, pp. 59-74, Jan, 2006.
11. J. Atencia, and D. J. Beebe, "Controlled microfluidic interfaces," *Nature,* vol. 437, no. 7059, pp. 648-655, Sep, 2005.
12. P. R. LeDuc, and R. M. Bellin, "Nanoscale intracellular organization and functional architecture mediating cellular behavior," *Annals of Biomedical Engineering,* vol. 34, no. 1, pp. 102-113, Jan, 2006.
13. D. B. Weibel, P. Garstecki, and G. M. Whitesides, "Combining microscience and neurobiology," *Current Opinion in Neurobiology,* vol. 15, no. 5, pp. 560-567, Oct, 2005.
14. S. K. W. Dertinger, D. T. Chiu, N. L. Jeon *et al.*, "Generation of gradients having complex shapes using microfluidic networks," *Analytical Chemistry,* vol. 73, no. 6, pp. 1240-1246, Mar, 2001.
15. N. L. Jeon, H. Baskaran, S. K. W. Dertinger *et al.*, "Neutrophil chemotaxis in linear and complex gradients of interleukin-8 formed in a microfabricated device," *Nature Biotechnology,* vol. 20, no. 8, pp. 826-830, Aug, 2002.
16. D. Irimia, S. Y. Liu, W. G. Tharp *et al.*, "Microfluidic system for measuring neutrophil migratory responses to fast switches of chemical gradients," *Lab on a Chip,* vol. 6, no. 2, pp. 191-198, Feb, 2006.
17. W. Saadi, S. J. Wang, F. Lin *et al.*, "A parallel-gradient microfluidic chamber for quantitative analysis of breast cancer cell chemotaxis," *Biomedical Microdevices,* vol. 8, no. 2, pp. 109-118, Jun, 2006.
18. K. Campbell, and A. Groisman, "Generation of complex concentration profiles in

microchannels in a logarithmically small number of steps," *Lab on a Chip,* vol. 7, no. 2, pp. 264-272, 2007.
19. R. C. Gunawan, J. Silvestre, H. R. Gaskins *et al.,* "Cell migration and polarity on microfabricated gradients of extracellular matrix proteins," *Langmuir,* vol. 22, no. 9, pp. 4250-4258, Apr, 2006.
20. S. W. Rhee, A. M. Taylor, D. H. Cribbs *et al.,* "External force-assisted cell positioning inside microfluidic devices," *Biomedical Microdevices,* vol. 9, no. 1, pp. 15-23, Feb, 2007.
21. A. Khademhosseini, J. Yeh, G. Eng *et al.,* "Cell docking inside microwells within reversibly sealed microfluidic channels for fabricating multiphenotype cell arrays," *Lab on a Chip,* vol. 5, no. 12, pp. 1380-1386, 2005.
22. P. Herzmark, K. Campbell, F. Wang *et al.,* "Bound attractant at the leading vs. the trailing edge determines chemotactic prowess," *Proceedings of the National Academy of Sciences of the United States of America,* vol. 104, no. 33, pp. 13349-13354, Aug, 2007.
23. L. L. Song, S. M. Nadkarni, H. U. Bodeker *et al.,* "Dicyostelium discoideum chemotaxis: Threshold for directed motion," *European Journal of Cell Biology,* vol. 85, no. 9-10, pp. 981-989, Sep, 2006.
24. J. Sager, M. Young, and D. Stefanovic, "Characterization of transverse channel concentration profiles obtainable with a class of microfluidic networks," *Langmuir,* vol. 22, no. 9, pp. 4452-4455, Apr, 2006.
25. Y. Wang, T. Mukherjee, and Q. Lin, "Systematic modeling of microfluidic concentration gradient generators," *Journal of Micromechanics and Microengineering,* vol. 16, no. 10, pp. 2128-2137, Oct, 2006.
26. C. W. Wei, J. Y. Cheng, and T. H. Young, "Elucidating in vitro cell-cell interaction using a microfluidic coculture system," *Biomedical Microdevices,* vol. 8, no. 1, pp. 65-71, Mar, 2006.
27. V. V. Abhyankar, and D. J. Beebe, "Spatiotemporal micropatterning of cells on arbitrary substrates," *Analytical Chemistry,* vol. 79, no. 11, pp. 4066-4073, Jun, 2007.
28. H. K. Wu, B. Huang, and R. N. Zare, "Generation of complex, static solution gradients in microfluidic channels," *Journal of the American Chemical Society,* vol. 128, no. 13, pp. 4194-4195, Apr, 2006.
29. H. M. Yu, I. Meyvantsson, I. A. Shkel *et al.,* "Diffusion dependent cell behavior in microenvironments," *Lab on a Chip,* vol. 5, no. 10, pp. 1089-1095, 2005.
30. S. Paliwal, P. A. Iglesias, K. Campbell *et al.,* "MAPK-mediated bimodal gene expression and adaptive gradient sensing in yeast," *Nature,* vol. 446, no. 7131, pp. 46-51, Mar, 2007.
31. K. C. Chaw, M. Manimaran, F. E. H. Tay *et al.,* "A quantitative observation and imaging of single tumor cell migration and deformation using a multi-gap microfluidic device representing the blood vessel," *Microvascular Research,* vol. 72, no. 3, pp. 153-160, Nov, 2006.
32. S. W. Nam, D. Van Noort, Y. Yang *et al.,* "A biological sensor platform using a pneumatic-valve controlled microfluidic device containing Tetrahymena pyriformis," *Lab on a Chip,* vol. 7, no. 5, pp. 638-640, 2007.
33. W. Saadi, S. W. Rhee, F. Lin *et al.,* "Generation of stable concentration gradients in 2D and 3D environments using a microfluidic ladder chamber," *Biomedical*

Microdevices, vol. 9, no. 5, pp. 627-635, Oct, 2007.
34. T. M. Keenan, C. H. Hsu, and A. Folch, "Microfluidic "jets" for generating steady-state gradients of soluble molecules on open surfaces," *Applied Physics Letters,* vol. 89, no. 11, pp. 3, Sep, 2006.
35. V. V. Abhyankar, M. A. Lokuta, A. Huttenlocher *et al.*, "Characterization of a membrane-based gradient generator for use in cell-signaling studies," *Lab on a Chip,* vol. 6, no. 3, pp. 389-393, Mar, 2006.
36. M. S. Kim, J. H. Yeon, and J. K. Park, "A microfluidic platform for 3-dimensional cell culture and cell-based assays," *Biomedical Microdevices,* vol. 9, no. 1, pp. 25-34, Feb, 2007.
37. C. W. Li, R. S. Chen, and M. S. Yang, "Generation of linear and non-linear concentration gradients along microfluidic channel by microtunnel controlled stepwise addition of sample solution," *Lab on a Chip,* vol. 7, no. 10, pp. 1371-1373, 2007.
38. M. Yamada, T. Hirano, M. Yasuda *et al.*, "A microfluidic flow distributor generating stepwise concentrations for high-throughput biochemical processing," *Lab on a Chip,* vol. 6, no. 2, pp. 179-184, Feb, 2006.
39. C. H. Hsu, and A. Folch, "Spatio-temporally-complex concentration profiles using a tunable chaotic micromixer," *Applied Physics Letters,* vol. 89, no. 14, pp. 3, Oct, 2006.
40. F. Q. Nie, M. Yamada, J. Kobayashi *et al.*, "On-chip cell migration assay using microfluidic channels," *Biomaterials,* vol. 28, no. 27, pp. 4017-4022, Sep, 2007.
41. D. Irimia, D. A. Geba, and M. Toner, "Universal microfluidic gradient generator," *Analytical Chemistry,* vol. 78, no. 10, pp. 3472-3477, May, 2006.
42. F. Lin, and E. C. Butcher, "T cell chemotaxis in a simple microfluidic device," *Lab on a Chip,* vol. 6, no. 11, pp. 1462-1469, 2006.
43. B. G. Chung, F. Lin, and N. L. Jeon, "A microfluidic multi-injector for gradient generation," *Lab on a Chip,* vol. 6, no. 6, pp. 764-768, Jun, 2006.
44. C. W. Frevert, G. Boggy, T. M. Keenan *et al.*, "Measurement of cell migration in response to an evolving radial chemokine gradient triggered by a microvalve," *Lab on a Chip,* vol. 6, no. 7, pp. 849-856, 2006.
45. R. Nielson, and J. B. Shear, "Parallel chemical dosing of subcellular targets," *Analytical Chemistry,* vol. 78, no. 17, pp. 5987-5993, Sep, 2006.
46. M. Geissler, P. Chalsani, N. S. Cameron *et al.*, "Patterning of chemical gradients with submicrometer resolution using edge-spreading lithography," *Small,* vol. 2, no. 6, pp. 760-765, Jun, 2006.
47. S. Hsu, R. Thakar, D. Liepmann *et al.*, "Effects of shear stress on endothelial cell haptotaxis on micropatterned surfaces," *Biochemical and Biophysical Research Communications,* vol. 337, no. 1, pp. 401-409, Nov, 2005.
48. P. Lee, R. Lin, J. Moon *et al.*, "Microfluidic alignment of collagen fibers for in vitro cell culture," *Biomedical Microdevices,* vol. 8, no. 1, pp. 35-41, Mar, 2006.
49. J. Nakanishi, Y. Kikuchi, S. Inoue *et al.*, "Spatiotemporal control of migration of single cells on a photoactivatable cell microarray," *Journal of the American Chemical Society,* vol. 129, no. 21, pp. 6694-+, May, 2007.
50. J. Y. Mai, C. Sun, S. Li *et al.*, "A microfabricated platform probing cytoskeleton dynamics using multidirectional topographical cues," *Biomedical Microdevices,* vol.

9, no. 4, pp. 523-531, Aug, 2007.
51. C. Crozatier, M. Le Berre, and Y. Chen, "Multi-colour micro-contact printing based on microfluidic network inking," *Microelectronic Engineering*, vol. 83, no. 4-9, pp. 910-913, Apr-Sep, 2006.
52. H. Levine, D. A. Kessler, and W. J. Rappel, "Directional sensing in eukaryotic chemotaxis: A balanced inactivation model," *Proceedings of the National Academy of Sciences of the United States of America*, vol. 103, no. 26, pp. 9761-9766, Jun, 2006.
53. S. I. Nishimura, and M. Sasai, "Modulation of the reaction rate of regulating protein induces large morphological and motional change of amoebic cell," *Journal of Theoretical Biology*, vol. 245, no. 2, pp. 230-237, Mar, 2007.
54. K. Wang, W. J. Rappel, R. Kerr *et al.*, "Quantifying noise levels of intercellular signals," *Physical Review E*, vol. 75, no. 6, pp. 5, Jun, 2007.
55. J. Park, T. Bansal, M. Pinelis *et al.*, "A microsystem for sensing and patterning oxidative microgradients during cell culture," *Lab on a Chip*, vol. 6, no. 5, pp. 611-622, 2006.
56. B. H. Chueh, D. Huh, C. R. Kyrtsos *et al.*, "Leakage-free bonding of porous membranes into layered microfluidic array systems," *Analytical Chemistry*, vol. 79, no. 9, pp. 3504-3508, May, 2007.

Appendix B

Finite Element Model (FEM) Theory and Derivations

Set up a mesh with rectangular blocks over the channel geometry. Set initial conditions and iterate over a specified number of time steps.

A.1 Preliminary Remarks on Taylor Expansion

If F and G are two smooth functions then, by the Taylor expansion,

$$\begin{cases} F(t+\delta)-F(t) & = F'(t)\delta + O(\delta^2), \\ G(x+\varepsilon)+G(x-\varepsilon)-2G(x) & = [G(x+\varepsilon)-G(x)]+[G(x-\varepsilon)-G(x)] \\ & = [G'(x)\varepsilon + \frac{1}{2!}G''(x)\varepsilon^2 + \frac{1}{3!}G'''(x)\varepsilon^3 + O(\varepsilon^4)] \\ & +[-G'(x)\varepsilon + \frac{1}{2!}G''(x)\varepsilon^2 - \frac{1}{3!}G'''(x)\varepsilon^3 + O(\varepsilon^4)] \\ & = G''(x)\varepsilon^2 + O(\varepsilon^4) \end{cases} \quad (*)$$

for small δ, ε.

A.2 Mesh with Square Blocks

This initial case explains how the mesh is set up for the case where mesh elements are square blocks.

Consider $C(\tau,x,y)$, where $\tau := (t-\frac{1}{2})\Delta\tau$, $x := (i-\frac{1}{2})\Delta x$, $y := (j-\frac{1}{2})\Delta y$, and $t = 1,\dots,T$, $i = 1,\dots,w$, $j = 1,\dots,h$, so that τ, x, y are half-integer multiples of t, i, j, respectively.

Consider the case when $\Delta x = \Delta y = \varepsilon > 0$. Also, write δ for $\Delta\tau$.

Then in the interior of the $h \times w$ rectangular channel, that is, for $1 < i < w$ and $1 < j < h$, one has:

$$\begin{aligned} & C(\tau,x,y) = (1-4f)C(\tau-\delta,x,y) \\ & +f\cdot[C(\tau-\delta,x-\varepsilon,y)+C(\tau-\delta,x+\varepsilon,y)+C(\tau-\delta,x,y-\varepsilon)+C(\tau-\delta,x,y+\varepsilon)] \\ & = C(\tau-\delta,x,y)+f\cdot[C(\tau-\delta,x-\varepsilon,y)+C(\tau-\delta,x+\varepsilon,y)-2C(\tau-\delta,x,y)] \\ & \qquad +f\cdot[C(\tau-\delta,x,y-\varepsilon)+C(\tau-\delta,x,y+\varepsilon)-2C(\tau-\delta,x,y)]. \end{aligned} \quad (1)$$

Assuming that the function C has a smooth extension, using (*), and neglecting terms $O(\delta^2)$ and $O(\varepsilon^4)$, arrive to the diffusion equation

$$\frac{\partial C}{\partial \tau} = D \cdot \left(\frac{\partial^2 C}{\partial x^2} + \frac{\partial^2 C}{\partial y^2}\right), \tag{2}$$

with the diffusion coefficient

$$D = \frac{f\varepsilon^2}{\delta} = \frac{f\Delta y^2}{\Delta \tau}. \tag{3}$$

A.3 Mesh with Rectangular Blocks

Interior Blocks

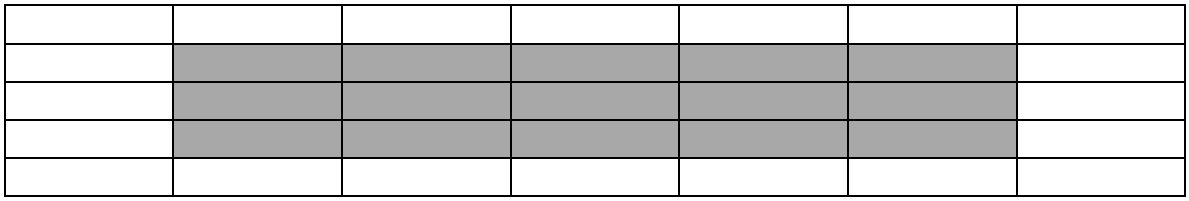

Now, to set up rectangular (vs. square) blocks, discretize the diffusion equation back, but with

$$\Delta x = \kappa \Delta y,$$

for some natural number κ. Then get the approximate equation

$$\frac{C(\tau,x,y)-C(\tau-\Delta\tau,x,y)}{\tau} = D\frac{C(\tau-\Delta\tau,x-\Delta x,y)+C(\tau-\Delta\tau,x+\Delta,y)-2C(\tau-\Delta\tau,x,y)}{\Delta x^2} + D\frac{C(\tau-\Delta\tau,x,y-\Delta y)+C(\tau-\Delta\tau,x,y+\Delta y)-2C(\tau-\Delta\tau,x,y)}{\Delta y^2},$$

which, for interior blocks, on recalling (3) and (4), can be rewritten similarly to (1):

$$\begin{aligned} C(\tau,x,y) &= [1-(\tfrac{2}{\kappa^2}+2)f]C(\tau-\Delta\tau,x,y) \\ &+\tfrac{f}{\kappa^2}\cdot[C(\tau-\Delta\tau,x-\Delta x,y)+C(\tau-\Delta\tau,x+\Delta x,y)] \\ &+f\cdot[C(\tau-\Delta\tau,x,y-\Delta y)+C(\tau-\Delta\tau,x,y+\Delta y)]; \end{aligned}$$

in fact, (1) is a special case of Eq. (interior), corresponding to $\kappa = 1$.

So, to sum up, what was done above may be referred to as the blocking – that is is, switching from the case of 1×1 mesh squares to $\kappa \times 1$ mesh blocks of such squares in the (i,j) domain, which corresponds to going from $\varepsilon \times \varepsilon = \Delta y \times \Delta y$ squares to $\Delta x \times \Delta y = (\kappa \Delta y) \times \Delta y$ blocks of such squares in the (x,y) domain. An advantage of the blocking is that it reduces the computer processing time about k times, even if using the same f. Another advantage is that the processing time can be reduced further almost twice for large κ (more exactly, $\frac{2}{1+1/\kappa^2}$ times, by increasing f this number of times); indeed, before the blocking, the restriction on f was $1 - 4f \geq 0$, and after the blocking it

gets relaxed to $1-(\frac{2}{\kappa^2}+2)f \geq 0$. Also, at least qualitatively, the effect of the blocking on the accuracy of the approximation is insignificant, even for κ as large as 10.

Top Blocks

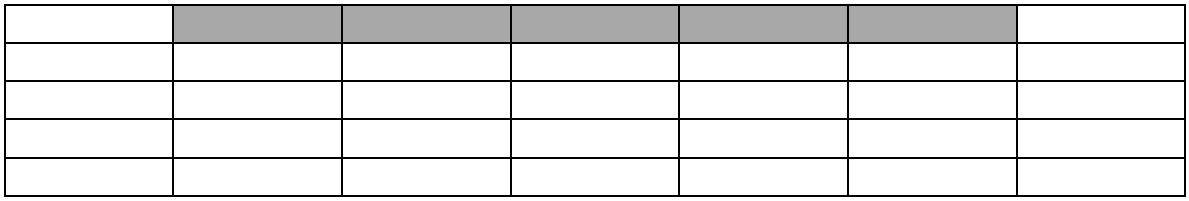

So, now consider the top boundary (except for the two upper corners), where

$$C(\tau,x,y) = (1-3f)C(\tau-\delta,x,y) \\ +f\cdot[C(\tau-\delta,x-\varepsilon,y)+C(\tau-\delta,x+\varepsilon,y)+C(\tau-\delta,x,y-\varepsilon)].$$

Neglecting terms of smaller orders of magnitude, one has

$$\frac{\partial C}{\partial \tau} = D\cdot(\frac{\partial^2 C}{\partial x^2}-\frac{1}{\varepsilon}\frac{\partial C}{\partial y}),$$

which is discretized as

$$\frac{C(\tau,x,y)-C(\tau-\Delta\tau,x,y)}{\tau} = D\frac{C(\tau-\Delta\tau,x-\Delta x,y)+C(\tau-\Delta\tau,x+\Delta x,y)-2C(\tau-\Delta\tau,x,y)}{\Delta x^2} \\ +\frac{D}{\Delta y}\frac{C(\tau-\Delta\tau,x,y-\Delta y)-C(\tau-\Delta\tau,x,y)}{\Delta y},$$

which can in be rewritten as

$$C(\tau,x,y) = [1-(\frac{2}{\kappa^2}+1)f]C(\tau-\Delta\tau,x,y) \\ +\frac{f}{\kappa^2}\cdot[C(\tau-\Delta\tau,x-\Delta x,y)+C(\tau-\Delta\tau,x+\Delta x,y)] \\ +f\cdot C(\tau-\Delta\tau,x,y-\Delta y).$$

Far End Blocks

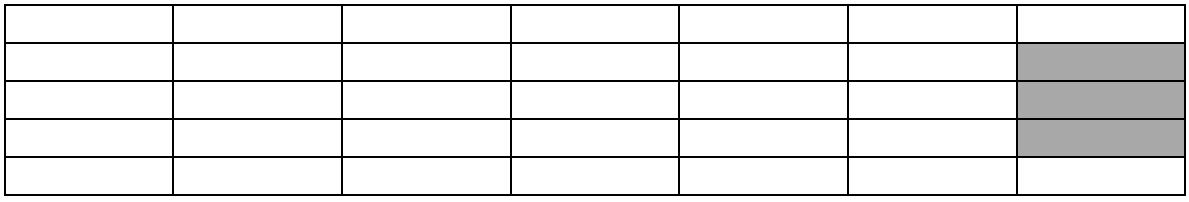

The “far end” case equations (except for the two “far end” corners) are similar to the “top” case ones:

$$C(\tau,x,y) = (1-3f)C(\tau-\delta,x,y) \\ +f\cdot[C(\tau-\delta,x-\varepsilon,y)+C(\tau-\delta,x,y-\varepsilon)+C(\tau-\delta,x,y+\varepsilon)],$$

$$\frac{\partial C}{\partial \tau} = D \cdot \left(\frac{\partial^2 C}{\partial y^2} - \frac{1}{\varepsilon}\frac{\partial C}{\partial x}\right),$$

$$\frac{C(\tau,x,y)-C(\tau-\Delta\tau,x,y)}{\tau} = D\,\frac{C(\tau-\Delta\tau,x,y-\Delta y)+C(\tau-\Delta\tau,x,y+\Delta y)-2C(\tau-\Delta\tau,x,y)}{\Delta y^2} + \frac{D}{\Delta y}\,\frac{C(\tau-\Delta\tau,x-\Delta x,y)-C(\tau-\Delta\tau,x,y)}{\Delta x},$$

$$\begin{aligned} C(\tau,x,y) &= [1-(\tfrac{1}{\kappa}+2)f]C(\tau-\Delta\tau,x,y) \\ &+\tfrac{f}{\kappa}\cdot C(\tau-\Delta\tau,x-\Delta x,y) \\ &+f\cdot[C(\tau-\Delta\tau,x,y-\Delta y)+C(\tau-\Delta\tau,x,y+\Delta y)]. \end{aligned}$$

Bottom Blocks

Similar considerations produce the equations for the bottom boundary (except for the two corners at the bottom), where $a \wedge b := \min(a,b)$:

$$\begin{aligned} C(\tau,x,y) = (1-3f)C(\tau-\delta,x,y) - f\cdot[(ac_0)\wedge C(\tau-\delta,x,y)]\cdot n(\tau,x) \\ +f\cdot[C(\tau-\delta,x-\varepsilon,y)+C(\tau-\delta,x+\varepsilon,y)+C(\tau-\delta,x,y+\varepsilon)], \end{aligned}$$

$$\frac{\partial C}{\partial \tau} = D\cdot\left(\frac{\partial^2 C}{\partial x^2}+\frac{1}{\varepsilon}\frac{\partial C}{\partial y}-\frac{1}{\varepsilon^2}[(ac_0)\wedge C]\cdot n\right),$$

$$\frac{C(\tau,x,y)-C(\tau-\Delta\tau,x,y)}{\tau} = D\,\frac{C(\tau-\Delta\tau,x-\Delta x,y)+C(\tau-\Delta\tau,x+\Delta x,y)-2C(\tau-\Delta\tau,x,y)}{\Delta x^2} + \frac{D}{\Delta y}\,\frac{C(\tau-\Delta\tau,x,y+\Delta y)-C(\tau-\Delta\tau,x,y)}{\Delta y} - \frac{D}{\Delta y^2}\,[(ac_0)\wedge C(\tau-\Delta\tau,x,y)]\cdot n(\tau,x),$$

$$\begin{aligned} C(\tau,x,y) &= [1-(\tfrac{2}{\kappa^2}+1)f]C(\tau-\Delta\tau,x,y) \\ &+\tfrac{f}{\kappa^2}\cdot[C(\tau-\Delta\tau,x-\Delta x,y)+C(\tau-\Delta\tau,x+\Delta x,y)] \\ &+f\cdot C(\tau-\Delta\tau,x,y+\Delta y)-f\cdot[(ac_0)\wedge C(\tau-\Delta\tau,x,y)]\cdot n(\tau,x). \end{aligned}$$

Top Far Corner

$$C(\tau,x,y) = (1-2f)C(\tau-\delta,x,y) + f\cdot[C(\tau-\delta,x-\varepsilon,y) + C(\tau-\delta,x,y-\varepsilon)],$$

$$\frac{\partial C}{\partial \tau} = -\frac{D}{\varepsilon}\cdot\left(\frac{\partial C}{\partial x} + \frac{\partial C}{\partial y}\right),$$

$$\frac{C(\tau,x,y)-C(\tau-\Delta\tau,x,y)}{\tau} = \frac{D}{\Delta y}\frac{C(\tau-\Delta\tau,x-\Delta x,y)-C(\tau-\Delta\tau,x,y)}{\Delta x} + \frac{D}{\Delta y}\frac{C(\tau-\Delta\tau,x,y-\Delta y)-C(\tau-\Delta\tau,x,y)}{\Delta y},$$

$$C(\tau,x,y) = [1-(\tfrac{1}{\kappa}+1)f]C(\tau-\Delta\tau,x,y) + \frac{f}{\kappa}\cdot C(\tau-\Delta\tau,x-\Delta x,y) + f\cdot C(\tau-\Delta\tau,x,y-\Delta y);$$

Bottom Far Corner

$$C(\tau,x,y) = (1-2f)C(\tau-\delta,x,y) + f\cdot[C(\tau-\delta,x-\varepsilon,y) + C(\tau-\delta,x,y+\varepsilon)] - f\cdot[(ac_0)\wedge C(\tau-\Delta\tau,x,y)]\cdot n(\tau,x),$$

$$\frac{\partial C}{\partial \tau} = \frac{D}{\varepsilon}\cdot\left(\frac{\partial C}{\partial y} - \frac{\partial C}{\partial x}\right) - \frac{D}{\varepsilon^2}\cdot[(ac_0)\wedge C]\cdot n,$$

$$\frac{C(\tau,x,y)-C(\tau-\Delta\tau,x,y)}{\tau} = \frac{D}{\Delta y}\frac{C(\tau-\Delta\tau,x-\Delta x,y)-C(\tau-\Delta\tau,x,y)}{\Delta x} + \frac{D}{\Delta y}\frac{C(\tau-\Delta\tau,x,y+\Delta y)-C(\tau-\Delta\tau,x,y)}{\Delta y} - \frac{D}{\Delta y^2}[(ac_0)\wedge C(\tau-\Delta\tau,x,y)]\cdot n(\tau,x),$$

$$
\begin{aligned}
C(\tau, x, y) \quad &= [1 - (\tfrac{1}{\kappa} + 1)f]C(\tau - \Delta\tau, x, y) \\
&+ \tfrac{f}{\kappa} \cdot C(\tau - \Delta\tau, x - \Delta x, y) + f \cdot C(\tau - \Delta\tau, x, y + \Delta y) \\
&- f \cdot [(ac_0) \wedge C(\tau - \Delta\tau, x, y)] \cdot n(\tau, x).
\end{aligned}
$$

Appendix C

Finite Element Model (FEM)
Mathematica Code and Sample Outputs

Input and output variables, in a logical order :

Diff = diffusion coefficient for oxygen in water, in mm^2/sec;

DiffCO2 = diffusion coefficient for CO_2 in water, in mm^2/sec;

Diff = diffusion coefficient for lactic acid in water, in mm^2/sec;

c0 = exterior, and initial interior, concentration of oxygen, assumed below to be 1, in appropriate units;

c = current concentration of oxygen relative to c0, so that $0 \le c \le 1$ and c*c0 is the absolute concentration of oxygen, depending on the time and space coordinates;

cr = critical level of c: cells will be dying if c<cr and will be multiplying if c>cr;

n = cell density, depending on the time and space coordinates;

nmax = maximum possible cell density, so that n cannot exceed nmax; in turn, the constant nmax cannot be greater than 1;

n0 = initial cell density;

taud = (abbreviation of tau_d, where d stands for death) = half-life=time, in hours, to halving the number of cells when c=0;

taub=(abbreviation of tau_b, where b stands for birth) = doubling-time=time, in hours, to doubling the number of cells when c=1 -- subject to the restriction that $n \le nmax$;

Dey = (abbreviation of Delta y, that is, Δy) = vertical measurement of one block, in mm;

Dex = (abbreviation of Delta x, that is, Δx) = horizontal measurement of one block, in mm;

h = number of blocks in one (vertical) column; h is an integer;

w = number of blocks in one (horizontal) row; w is an integer;

B is the parameter of the birth-death rate profile curve, described in file bd_profile.nb; the greater value of B, the steeper is the curve at c=cr;

tauObservation = observation period, in hours;

T = number of time steps in the observation period;

[t1,t2] = observation window, where t2 is the last time step within the window, and t1 is the last time step preceding the window; for example, if T=35000, t1=1000, and t2=4000, then, of the total 35000 time steps, the observation window is over the time steps 1001, 1002, ..., 2000;

CO2 = current concentration of CO_2 relative to c0, so that CO2*c0 is the absolute concentration of CO_2, depending on the time and space coordinates;

Lact = current concentration of lactic acid relative to c0, so that Lact*c0 is the absolute concentration of lactic acid, depending on the time and space coordinates;

la = a coefficient for lactic production, assumed to be 0.8 in the example below; according to the legend to Fig. 1 in Arthur et al (2000), lactate output may decrease by 10--20% as the oxygen concentration falls down from the normoxic one; the coefficient la accounts for such a decrease;

Input variables, in the order in which they go in the input: c0, Diff, Dey, Dex, h, w, nmax, n0, tauObservation, taud, taub, cr, B, DiffCO2, DiffLac

Output variables: c, n, CO2, Lact; other output variables are described explicitly in the output: "observation period", "number of time steps in the observation period", "time step", "height of capillary", "length of capilla

$$\text{mult}[c\_] = \text{If}\left[0 \le c \le cr,\ 1 - (B+1)\, d \left(1 - \frac{c}{cr}\right)^B,\ 1 + (B+1)\, b \left(\frac{c - cr}{1 - cr}\right)^B\right];$$

here mult is the new, flat multiplier, that is, the birth - death rate profile function, described in file flat_bdProfile.nb

```
SciForm[x_] := If[x ≥ .01, x, ScientificForm[x, 3]];
SetAttributes[SciForm, Listable];
```

```
In[1]:= SciForm[{9, .98, .098, .0098, .00098}]
```

Out[1]= $\{9, 0.98, 0.098, 9.8 \times 10^{-3}, 9.8 \times 10^{-4}\}$

```
In[2]:= ClearAll[c, n, CO2, Lact, ka, f, Dex, Dey, Detau, Td, Tb, b, d, be, ga, fCO2, fLact, T, c0, Diff,
  Dey, Dex, h, w, nmax, n0, tauObservation, taud, taub, cr, B, DiffCO2, DiffLact, t1, t2]

In[3]:= consts := (ka = Dex / Dey

  (* number of squares in one horizontal block of squares of dimensions 1*ka *);

  f = 1 / (2/ka^2 + 2); (* f=flux rate,between 0 and 0.5;

  the oxygen outflow through each of the two horizontal sides of any block
   in the grid is f*c unless the block is at the boundary of the grid,
  in which latter case a modification of this rule applies *)
  Detau = f Dey^2 / Diff (* time step, Δt, in seconds, by formula (3) in the write-up *);

  rho0f = 0.00041050903119868647 Detau / Dey

  (* this is the product rho0*f, according to file rho.nb *);
  Td = 3600 taud / Detau (* number of time steps to halving the number of cells when c<
   cr*c0; the factor 3600 here is the number of seconds in one hour *);
  Tb = 3600 taub / Detau (* number of time steps to doubling
    the number of cells when c≥cr*c0 *);
  b = 2^(1/Tb) - 1; d = 2^(1/Td) - 1;
  p = B cr/d; q = B (1 - cr)/b;
  fCO2 = DiffCO2 Detau / Dey^2;
  fLact = DiffLact Detau / Dey^2;

  T = tauObservation 3600 / Detau // Floor;)

In[4]:= window := (

  Do[
```

```
Do[ {cc[i, j], CO2[i, j], LLact[i, j]} =

  Which[ (* interior *)
   0 < i < w && 1 < j < h,
   {(*(1- (2/ka^2+2)f)c[i,j]+*)
    f ((c[i - 1, j] + c[i + 1, j])/ka^2 + c[i, j - 1] + c[i, j + 1]),
    (1 - (2/ka^2 + 2) fCO2) CO2[i, j] +
     fCO2 ((CO2[i - 1, j] + CO2[i + 1, j])/ka^2 + CO2[i, j - 1] + CO2[i, j + 1]),
    (1 - (2/ka^2 + 2) fLact) Lact[i, j] +
     fLact ((Lact[i - 1, j] + Lact[i + 1, j])/ka^2 + Lact[i, j - 1] + Lact[i, j + 1])
   },
   (* left end *)
   (* i==0&&1<=j<=h,{c0,0,0}, *)
   (* right end *)
   i == w && 1 < j < h,
   {(1 - (1/ka + 2) f) c[i, j] + f (1/ka c[i - 1, j] + c[i, j - 1] + c[i, j + 1]),
    (1 - (1/ka + 2) fCO2) CO2[i, j] + fCO2 (1/ka CO2[i - 1, j] + CO2[i, j - 1] + CO2[i, j + 1]),
    (1 - (1/ka + 2) fLact) Lact[i, j] +
     fLact (1/ka Lact[i - 1, j] + Lact[i, j - 1] + Lact[i, j + 1])},
   (* right bottom corner *)
   i == w && j == 1,
   (rhof = rho0f (1 + Sqrt[c[i, j]])/2;
    n[i] = Min[nmax, mult[c[i, j]] n[i]];
```

$$\left\{\left(1-\left(\frac{1}{ka}+1\right) f\right) c[i, j]-\text{rhof } c[i, j] n[i]+f\left(\frac{1}{ka} c[i-1, j]+c[i, j+1]\right),\right.$$
$$\left(1-\left(\frac{1}{ka}+1\right) fCO2\right) CO2[i, j]+$$
$$\text{rhof } c[i, j] n[i]+fCO2\left(\frac{1}{ka} CO2[i-1, j]+CO2[i, j+1]\right),$$
$$\left(1-\left(\frac{1}{ka}+1\right) fLact\right) Lact[i, j]+3 \text{ la rho0f } c0 n[i]+$$
$$\left.fLact\left(\frac{1}{ka} Lact[i-1, j]+Lact[i, j+1]\right)\right\}$$
$$\Bigg),$$

```
(* right top corner *)
```

$$i==w \&\& j==h, \left\{\left(1-\left(\frac{1}{ka}+1\right) f\right) c[i, j]+f\left(\frac{1}{ka} c[i-1, j]+c[i, j-1]\right),\right.$$
$$\left(1-\left(\frac{1}{ka}+1\right) fCO2\right) CO2[i, j]+fCO2\left(\frac{1}{ka} CO2[i-1, j]+CO2[i, j-1]\right),$$
$$\left.\left(1-\left(\frac{1}{ka}+1\right) fLact\right) Lact[i, j]+fLact\left(\frac{1}{ka} Lact[i-1, j]+Lact[i, j-1]\right)\right\},$$

```
(* top *)
```

$$0<i<w \&\& j==h, \left\{\left(1-\left(\frac{2}{ka^2}+1\right) f\right) c[i, j]+f\left(\frac{c[i-1, j]+c[i+1, j]}{ka^2}+c[i, j-1]\right),\right.$$
$$\left(1-\left(\frac{2}{ka^2}+1\right) fCO2\right) CO2[i, j]+fCO2\left(\frac{CO2[i-1, j]+CO2[i+1, j]}{ka^2}+CO2[i, j-1]\right),$$
$$\left(1-\left(\frac{2}{ka^2}+1\right) fLact\right) Lact[i, j]+$$
$$\left.fLact\left(\frac{Lact[i-1, j]+Lact[i+1, j]}{ka^2}+Lact[i, j-1]\right)\right\},$$

```
(* bottom *)
```

$$0<i<w \&\& j==1,$$
$$\left(\text{rhof}=\text{rho0f}\ \frac{1+\sqrt{c[i, j]}}{2};\right.$$
$$\left.n[i]=\text{Min}[nmax, \text{mult}[c[i, j]] n[i]]\right);$$

$$\left\{\left(1-\left(\frac{2}{ka^2}+1\right)f\right)c[i,j]-rhof\ c[i,j]\,n[i]+f\left(c[i,j+1]+\frac{c[i-1,j]+c[i+1,j]}{ka^2}\right),\right.$$
$$\left(1-\left(\frac{2}{ka^2}+1\right)fCO2\right)CO2[i,j]+$$
$$rhof\ c[i,j]\,n[i]+fCO2\left(CO2[i,j+1]+\frac{CO2[i-1,j]+CO2[i+1,j]}{ka^2}\right),$$
$$\left(1-\left(\frac{2}{ka^2}+1\right)fLact\right)Lact[i,j]+3\,la\,rho0f\ c0\,n[i]+$$
$$\left.fLact\left(Lact[i,j+1]+\frac{Lact[i-1,j]+Lact[i+1,j]}{ka^2}\right)\right\}$$

```
    ] (* end of processing the (i,j) block *), {i, 1, w}, {j, 1, h}];
  Do[{c[i, j], CO2[i, j], Lact[i, j]} =
    {cc[i, j], CCO2[i, j], LLact[i, j]}, {i, 1, w}, {j, 1, h}];
 ),
 {t, t1 + 1, t2}];
cTableUpDown = Table[c[i, h + 1 - j], {i, 1, w}, {j, 1, h}];
nTable = Table[n[i], {i, 1, w}];
CO2TableUpDown = Table[CO2[i, h + 1 - j], {i, 1, w}, {j, 1, h}];
CO2Max = Max[CO2TableUpDown];
LactTableUpDown = Table[Lact[i, h + 1 - j], {i, 1, w}, {j, 1, h}];
cTable = cTableUpDown // Transpose;
CO2Table = CO2TableUpDown // Transpose;
LactTable = LactTableUpDown // Transpose;
)
```

```
graphs :=
 (cGraph = ListPlot[cTable, PlotStyle → {Blue, Green, Red}, Joined → True, AxesOrigin → {0, 0},
    PlotRange → {0, 1}, AxesLabel → {i, c}, ImageSize → {ff X, ff Y}];
  (* This gives the h graphs (here h=3) for c at time step tt,
  one graph for each of the h rows of the c-table;
  the bottom-row graph is colored red, the top-row one blue,
  and the middle-row one green; these three graphs are very close to one another *)
  nGraph = ListPlot[nTable, PlotStyle → {Blue}, Joined → True, AxesOrigin → {0, 0},
    PlotRange → {0, 1}, AxesLabel → {i, n}, ImageSize → {ff X, ff Y}];
  CO2Graph = ListPlot[CO2Table, PlotStyle → {Blue, Green, Red}, Joined → True,
    AxesOrigin → {0, 0}, PlotRange → All, AxesLabel → {i, CO2}, ImageSize -> {ff X, ff Y}];
  LactGraph = ListPlot[LactTable, PlotStyle → {Blue, Green, Red}, Joined → True,
    AxesOrigin → {0, 0}, PlotRange → All, AxesLabel → {i, Lact}, ImageSize → {ff X, ff Y}];
  {{cGraph, nGraph},
    {CO2Graph, LactGraph}} // TableForm // Print;
  Print["observation period = ", T Detau / 3600, " hours"];
  Print["number of time steps in the observation period = ", T];

  Print["time step = ", Detau, " sec"];
  Print["height of capillary = ", h Dey, "mm"];
  Print["length of capillary = ", w Dex, "mm"];
 )
```

```
In[111]:= tablesPrint := (Print[
            "-------------------------------------------------------------------------------"];
          Print["O2 concentration c[t2,i,j], 1≤i≤", w, ", 1≤j≤", h, ":"];
          k = Floor[w / 9]; r = w - 9 k;
          Do[TableForm[Take[cTableUpDown // SciForm, {9 (q - 1) + 1, 9 q}] // Transpose, TableHeadings →
              {Table[h + 1 - j, {j, 1, h}], Table[i, {i, 9 (q - 1) + 1, 9 q}]}] // Print, {q, 1, k}];
          If[9 k < w, TableForm[Take[cTableUpDown // SciForm, {9 k + 1, w}] // Transpose,
             TableHeadings → {Table[h + 1 - j, {j, 1, h}], Table[i, {i, 9 k + 1, w}]}] // Print];
          Print[
           "-------------------------------------------------------------------------------"];
          Print["cell density n[t2,i], 1≤i≤", w, ":"];
          kd = Floor[w / 8]; rd = w - 8 kd;
          Do[TableForm[{Take[nTable // SciForm, {8 (q - 1) + 1, 8 q}]},
             TableHeadings → {None, Table[i, {i, 8 (q - 1) + 1, 8 q}]}] // Print, {q, 1, kd}];
          If[8 kd < w, TableForm[{Take[nTable // SciForm, {8 kd + 1, w}]},
             TableHeadings → {None, Table[i, {i, 8 kd + 1, w}]}] // Print];
          Print[
           "-------------------------------------------------------------------------------"];
          Print["CO2 concentration CO2[t2,i,j], 1≤i≤", w, ", 1≤j≤", h, ":"];
          k = Floor[w / 10]; r = w - 10 k;
          Do[TableForm[Take[CO2TableUpDown, {10 (q - 1) + 1, 10 q}] // Transpose, TableHeadings →
              {Table[h + 1 - j, {j, 1, h}], Table[i, {i, 10 (q - 1) + 1, 10 q}]}] // Print, {q, 1, k}];
          If[10 k < w, TableForm[Take[CO2TableUpDown, {10 k + 1, w}] // Transpose,
             TableHeadings → {Table[h + 1 - j, {j, 1, h}], Table[i, {i, 10 k + 1, w}]}] // Print];
          Print[
           "-------------------------------------------------------------------------------"];
          Print["lactic acid concentration Lact[t2,i,j], 1≤i≤", w, ", 1≤j≤", h, ":"];
          k = Floor[w / 10]; r = w - 10 k;
          Do[TableForm[Take[LactTableUpDown, {10 (q - 1) + 1, 10 q}] // Transpose, TableHeadings →
              {Table[h + 1 - j, {j, 1, h}], Table[i, {i, 10 (q - 1) + 1, 10 q}]}] // Print, {q, 1, k}];
          If[10 k < w, TableForm[Take[LactTableUpDown, {10 k + 1, w}] // Transpose,
             TableHeadings → {Table[h + 1 - j, {j, 1, h}], Table[i, {i, 10 k + 1, w}]}] // Print];
          Print[
           "-------------------------------------------------------------------------------"];)

In[112]:=

In[113]:= X = 600; Y = 400; (* X and Y are the dimensions of the output panel *)
          ff = .45; (* ff is the fraction of the entire panel, horizontally and vertically,
          occupied by each one of the four graphs -- of c, n, CO2, and Lact *)
```

```
In[104]:= input := (
            c[i_, j_] = c0 = 1;
            Diff = 0.002;
            CO2[i_, j_] = 0;
            DiffCO2 = 0.0015;
            Lact[i_, j_] = 0;
            DiffLact = 0.0009;
            Dey = 0.1; Dex = 1;
            h = 3; w = 50;
            nmax = 1;
            n[i_] = n0 = .8;
            tauObservation = 8; taub = 1.92; taud = 1.92; cr = .1;
            cr = .5;
            B = 3;
            la = .8;)

In[106]:= ClearAll[c, n, CO2, Lact];
          input; consts;

In[107]:= T

Out[107]= 11635

In[108]:= t1 = 0; t2 = 1000;
          win = window; // Timing
          win
          graphs
          tablesPrint

Out[109]= {10.828, Null}
```

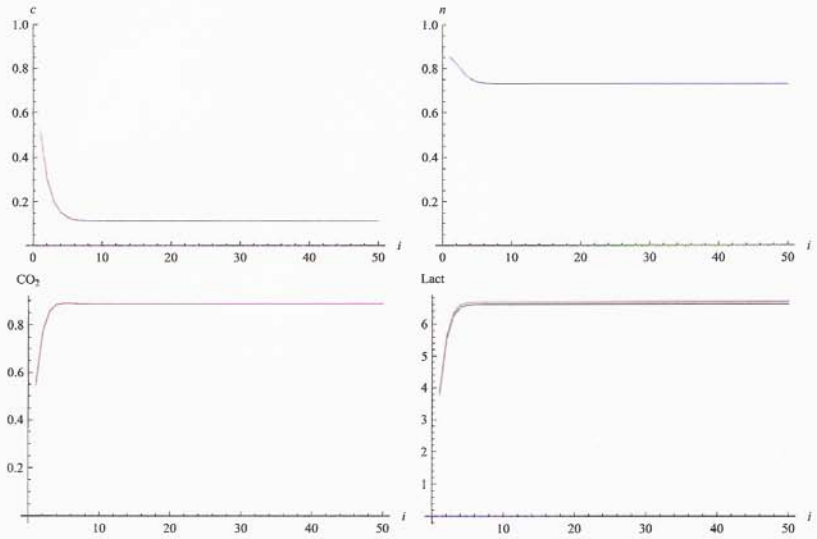

observation period = 7.99986 hours

number of time steps in the observation period = 11635

time step = 2.47525 sec

height of capillary = 0.3mm

length of capillary = 50mm

O_2 concentration c[t2,i,j], 1≤i≤50, 1≤j≤3:

	1	2	3	4	5	6	7	8	9
3	0.528473	0.306031	0.201467	0.152565	0.130249	0.120456	0.116357	0.114726	0.114111
2	0.525903	0.304698	0.200689	0.15202	0.129802	0.120051	0.115968	0.114344	0.113731
1	0.520726	0.302041	0.199138	0.150934	0.128911	0.119241	0.115192	0.113581	0.112973

	10	11	12	13	14	15	16	17	18
3	0.11389	0.113815	0.113791	0.113784	0.113782	0.113781	0.113781	0.113781	0.113781
2	0.113511	0.113437	0.113412	0.113405	0.113403	0.113402	0.113402	0.113402	0.113402
1	0.112755	0.112681	0.112657	0.11265	0.112648	0.112647	0.112647	0.112647	0.112647

	19	20	21	22	23	24	25	26	27
3	0.113781	0.113781	0.113781	0.113781	0.113781	0.113781	0.113781	0.113781	0.113781
2	0.113402	0.113402	0.113402	0.113402	0.113402	0.113402	0.113402	0.113402	0.113402
1	0.112647	0.112647	0.112647	0.112647	0.112647	0.112647	0.112647	0.112647	0.112647

	28	29	30	31	32	33	34	35	36
3	0.113781	0.113781	0.113781	0.113781	0.113781	0.113781	0.113781	0.113781	0.113781
2	0.113402	0.113402	0.113402	0.113402	0.113402	0.113402	0.113402	0.113402	0.113402
1	0.112647	0.112647	0.112647	0.112647	0.112647	0.112647	0.112647	0.112647	0.112647

	37	38	39	40	41	42	43	44	45
3	0.113781	0.113781	0.113781	0.113781	0.113781	0.113781	0.113781	0.113781	0.113781
2	0.113402	0.113402	0.113402	0.113402	0.113402	0.113402	0.113402	0.113402	0.113402
1	0.112647	0.112647	0.112647	0.112647	0.112647	0.112647	0.112647	0.112647	0.112647

	46	47	48	49	50
3	0.113781	0.113781	0.113781	0.113781	0.113781
2	0.113402	0.113402	0.113402	0.113402	0.113402
1	0.112647	0.112647	0.112647	0.112647	0.112647

---

cell density n[t2,i], 1≤i≤50:

1	2	3	4	5	6	7	8
0.854437	0.825816	0.783513	0.754677	0.740697	0.734835	0.73258	0.731766

9	10	11	12	13	14	15	16
0.731489	0.731399	0.731371	0.731363	0.731361	0.73136	0.73136	0.73136

17	18	19	20	21	22	23	24
0.73136	0.73136	0.73136	0.73136	0.73136	0.73136	0.73136	0.73136

25	26	27	28	29	30	31	32
0.73136	0.73136	0.73136	0.73136	0.73136	0.73136	0.73136	0.73136

33	34	35	36	37	38	39	40
0.73136	0.73136	0.73136	0.73136	0.73136	0.73136	0.73136	0.73136

41	42	43	44	45	46	47	48
0.73136	0.73136	0.73136	0.73136	0.73136	0.73136	0.73136	0.73136

49	50
0.73136	0.73136

CO_2 concentration CO2[t2,i,j], 1≤i≤50, 1≤j≤3:

	1	2	3	4	5	6	7	8	9	10
3	0.548252	0.773684	0.857365	0.88376	0.889414	0.889045	0.887759	0.886845	0.886373	0.886168
2	0.551679	0.775461	0.858403	0.884487	0.89001	0.889587	0.888278	0.887356	0.88688	0.886674
1	0.558582	0.779005	0.860472	0.885937	0.891199	0.890668	0.889314	0.888374	0.887892	0.887684

	11	12	13	14	15	16	17	18	19	20
3	0.886089	0.886062	0.886054	0.886051	0.88605	0.88605	0.88605	0.88605	0.88605	0.88605
2	0.886595	0.886568	0.886559	0.886557	0.886556	0.886556	0.886556	0.886556	0.886556	0.886556
1	0.887604	0.887577	0.887568	0.887565	0.887565	0.887565	0.887564	0.887564	0.887564	0.887564

	21	22	23	24	25	26	27	28	29	30
3	0.88605	0.88605	0.88605	0.88605	0.88605	0.88605	0.88605	0.88605	0.88605	0.88605
2	0.886556	0.886556	0.886556	0.886556	0.886556	0.886556	0.886556	0.886556	0.886556	0.886556
1	0.887564	0.887564	0.887564	0.887564	0.887564	0.887564	0.887564	0.887564	0.887564	0.887564

	31	32	33	34	35	36	37	38	39	40
3	0.88605	0.88605	0.88605	0.88605	0.88605	0.88605	0.88605	0.88605	0.88605	0.88605
2	0.886556	0.886556	0.886556	0.886556	0.886556	0.886556	0.886556	0.886556	0.886556	0.886556
1	0.887564	0.887564	0.887564	0.887564	0.887564	0.887564	0.887564	0.887564	0.887564	0.887564

	41	42	43	44	45	46	47	48	49	50
3	0.88605	0.88605	0.88605	0.88605	0.88605	0.88605	0.88605	0.88605	0.88605	0.88605
2	0.886556	0.886556	0.886556	0.886556	0.886556	0.886556	0.886556	0.886556	0.886556	0.886556
1	0.887564	0.887564	0.887564	0.887564	0.887564	0.887564	0.887564	0.887564	0.887564	0.887564

---

lactic acid concentration Lact[t2,i,j], 1≤i≤50, 1≤j≤3:

	1	2	3	4	5	6	7	8	9	10
3	3.75691	5.54849	6.26484	6.50821	6.57865	6.59558	6.59863	6.59886	6.59873	6.59865
2	3.78767	5.57862	6.29347	6.5358	6.60574	6.62245	6.62542	6.62562	6.62548	6.6254
1	3.8495	5.63889	6.35069	6.59094	6.65986	6.67614	6.67895	6.67909	6.67894	6.67885

	11	12	13	14	15	16	17	18	19	20
3	6.59862	6.59861	6.59861	6.59861	6.5986	6.5986	6.5986	6.5986	6.5986	6.5986
2	6.62537	6.62536	6.62535	6.62535	6.62535	6.62535	6.62535	6.62535	6.62535	6.62535
1	6.67881	6.6788	6.6788	6.67879	6.67879	6.67879	6.67879	6.67879	6.67879	6.67879

	21	22	23	24	25	26	27	28	29	30
3	6.5986	6.5986	6.5986	6.5986	6.5986	6.5986	6.5986	6.5986	6.5986	6.5986
2	6.62535	6.62535	6.62535	6.62535	6.62535	6.62535	6.62535	6.62535	6.62535	6.62535
1	6.67879	6.67879	6.67879	6.67879	6.67879	6.67879	6.67879	6.67879	6.67879	6.67879

	31	32	33	34	35	36	37	38	39	40
3	6.5986	6.5986	6.5986	6.5986	6.5986	6.5986	6.5986	6.5986	6.5986	6.5986
2	6.62535	6.62535	6.62535	6.62535	6.62535	6.62535	6.62535	6.62535	6.62535	6.62535
1	6.67879	6.67879	6.67879	6.67879	6.67879	6.67879	6.67879	6.67879	6.67879	6.67879

	41	42	43	44	45	46	47	48	49	50
3	6.5986	6.5986	6.5986	6.5986	6.5986	6.5986	6.5986	6.5986	6.5986	6.5986
2	6.62535	6.62535	6.62535	6.62535	6.62535	6.62535	6.62535	6.62535	6.62535	6.62535
1	6.67879	6.67879	6.67879	6.67879	6.67879	6.67879	6.67879	6.67879	6.67879	6.67879

In[113]:=
```
t1 = 100; t2 = T;
win = window; // Timing
win
graphs
tablesPrint
```

Out[114]= {127.485, Null}

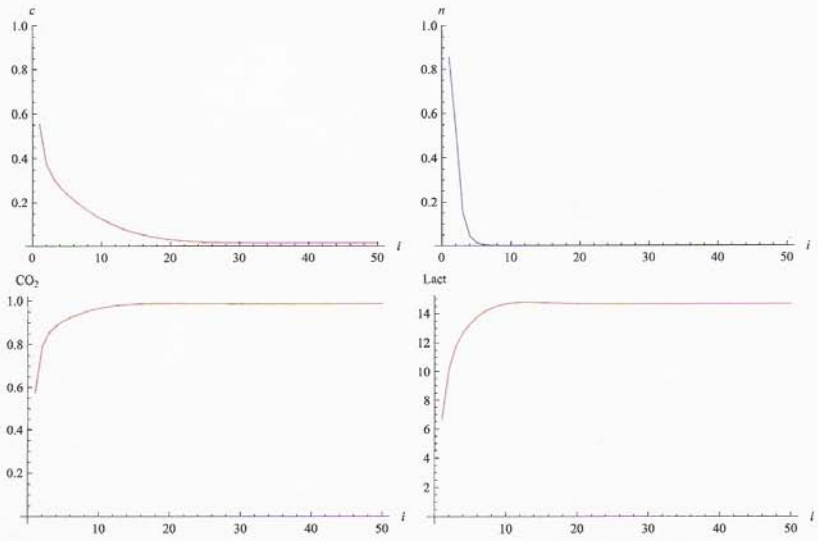

observation period = 7.99986 hours

number of time steps in the observation period = 11635

time step = 2.47525 sec

height of capillary = 0.3mm

length of capillary = 50mm

O_2 concentration c[t2,i,j], 1≤i≤50, 1≤j≤3:

	1	2	3	4	5	6	7	8	9
3	0.552539	0.376942	0.310049	0.270463	0.239138	0.211624	0.186746	0.164152	0.143709
2	0.549824	0.375863	0.30979	0.270397	0.239119	0.211617	0.186743	0.164151	0.143708
1	0.54435	0.373715	0.309277	0.270267	0.23908	0.211604	0.186738	0.164149	0.143707

	10	11	12	13	14	15	16	17	18
3	0.125333	0.108943	0.0944408	0.0817153	0.0706415	0.061085	0.0529065	0.0459653	0.0401228
2	0.125333	0.108943	0.0944407	0.0817153	0.0706415	0.061085	0.0529065	0.0459652	0.0401228
1	0.125333	0.108942	0.0944405	0.0817152	0.0706414	0.061085	0.0529065	0.0459652	0.0401228

	19	20	21	22	23	24	25	26	27
3	0.0352457	0.031208	0.0278925	0.0251923	0.0230112	0.0212635	0.0198746	0.0187796	0.0179233
2	0.0352457	0.031208	0.0278925	0.0251923	0.0230112	0.0212635	0.0198746	0.0187796	0.0179233
1	0.0352457	0.031208	0.0278925	0.0251923	0.0230112	0.0212635	0.0198746	0.0187796	0.0179233

	28	29	30	31	32	33	34	35	36
3	0.0172591	0.0167479	0.0163576	0.016062	0.0158399	0.0156743	0.0155519	0.015462	0.0153965
2	0.0172591	0.0167479	0.0163576	0.016062	0.0158399	0.0156743	0.0155519	0.015462	0.0153965
1	0.0172591	0.0167479	0.0163576	0.016062	0.0158399	0.0156743	0.0155519	0.015462	0.0153965

	37	38	39	40	41	42	43	44	45
3	0.0153493	0.0153154	0.0152912	0.0152742	0.0152623	0.015254	0.0152483	0.0152444	0.0152418
2	0.0153493	0.0153154	0.0152912	0.0152742	0.0152623	0.015254	0.0152483	0.0152444	0.0152418
1	0.0153492	0.0153154	0.0152912	0.0152742	0.0152623	0.015254	0.0152483	0.0152444	0.0152418

	46	47	48	49	50
3	0.01524	0.0152389	0.0152383	0.0152379	0.0152379
2	0.01524	0.0152389	0.0152383	0.0152379	0.0152379
1	0.01524	0.0152389	0.0152383	0.0152379	0.0152379

---

cell density n[t2,i], 1≤i≤50:

1	2	3	4	5	6	7	8
0.857131	0.518077	0.152538	0.0455524	0.0156771	6.16×10^{-3}	2.71×10^{-3}	1.32×10^{-3}

9	10	11	12	13	14	15	16
7.03×10^{-4}	4.06×10^{-4}	2.54×10^{-4}	1.7×10^{-4}	1.21×10^{-4}	9.15×10^{-5}	7.25×10^{-5}	5.99×10^{-5}

17	18	19	20	21	22	23	24
5.14×10^{-5}	4.54×10^{-5}	4.12×10^{-5}	3.81×10^{-5}	3.59×10^{-5}	3.43×10^{-5}	3.31×10^{-5}	3.22×10^{-5}

25	26	27	28	29	30	31	32
3.15×10^{-5}	3.1×10^{-5}	3.07×10^{-5}	3.04×10^{-5}	3.02×10^{-5}	3.01×10^{-5}	$3.\times10^{-5}$	2.99×10^{-5}

33	34	35	36	37	38	39	40
2.99×10^{-5}	2.98×10^{-5}	2.98×10^{-5}	2.98×10^{-5}	2.98×10^{-5}	2.98×10^{-5}	2.97×10^{-5}	2.97×10^{-5}

41	42	43	44	45	46	47	48
2.97×10^{-5}	2.97×10^{-5}	2.97×10^{-5}	2.97×10^{-5}	2.97×10^{-5}	2.97×10^{-5}	2.97×10^{-5}	2.97×10^{-5}

49	50
2.97×10^{-5}	2.97×10^{-5}

CO_2 concentration CO2[t2,i,j], 1≤i≤50, 1≤j≤3:

	1	2	3	4	5	6	7	8	9	10
3	0.575113	0.787867	0.855826	0.88756	0.908572	0.924938	0.938381	0.949524	0.95869	0.966117
2	0.578733	0.789305	0.856172	0.887648	0.908598	0.924947	0.938384	0.949525	0.958691	0.966117
1	0.586032	0.79217	0.856856	0.887822	0.90865	0.924964	0.938391	0.949528	0.958692	0.966118

	11	12	13	14	15	16	17	18	19	20
3	0.972018	0.976601	0.980066	0.982601	0.984382	0.985565	0.986288	0.986668	0.986803	0.986771
2	0.972018	0.976601	0.980066	0.982601	0.984382	0.985565	0.986288	0.986669	0.986803	0.986771
1	0.972019	0.976602	0.980066	0.982601	0.984382	0.985565	0.986288	0.986669	0.986803	0.986771

	21	22	23	24	25	26	27	28	29	30
3	0.986633	0.986436	0.986212	0.985986	0.985771	0.985578	0.98541	0.985268	0.985151	0.985057
2	0.986633	0.986436	0.986212	0.985986	0.985771	0.985578	0.98541	0.985268	0.985151	0.985057
1	0.986633	0.986436	0.986212	0.985986	0.985771	0.985578	0.98541	0.985268	0.985151	0.985057

	31	32	33	34	35	36	37	38	39	40
3	0.984983	0.984925	0.984881	0.984848	0.984823	0.984805	0.984793	0.984783	0.984777	0.984773
2	0.984983	0.984925	0.984881	0.984848	0.984823	0.984805	0.984793	0.984783	0.984777	0.984773
1	0.984983	0.984925	0.984881	0.984848	0.984823	0.984805	0.984793	0.984783	0.984777	0.984773

	41	42	43	44	45	46	47	48	49	50
3	0.98477	0.984767	0.984766	0.984765	0.984765	0.984764	0.984764	0.984764	0.984764	0.984764
2	0.98477	0.984767	0.984766	0.984765	0.984765	0.984764	0.984764	0.984764	0.984764	0.984764
1	0.98477	0.984767	0.984766	0.984765	0.984765	0.984764	0.984764	0.984764	0.984764	0.984764

lactic acid concentration Lact[t2,i,j], 1≤i≤50, 1≤j≤3:

	1	2	3	4	5	6	7	8	9	10
3	6.66899	10.2259	11.8117	12.7221	13.349	13.8083	14.1453	14.3862	14.551	14.6567
2	6.6997	10.2448	11.8174	12.7238	13.3496	13.8085	14.1454	14.3863	14.5511	14.6567
1	6.76153	10.2825	11.8287	12.7272	13.3508	13.809	14.1456	14.3864	14.5511	14.6567

	11	12	13	14	15	16	17	18	19	20
3	14.7178	14.7469	14.7543	14.7479	14.7339	14.7164	14.6984	14.6815	14.6668	14.6545
2	14.7178	14.747	14.7543	14.7479	14.7339	14.7164	14.6984	14.6815	14.6668	14.6545
1	14.7178	14.747	14.7543	14.7479	14.7339	14.7164	14.6984	14.6815	14.6668	14.6545

	21	22	23	24	25	26	27	28	29	30
3	14.6446	14.637	14.6312	14.6269	14.6238	14.6217	14.6202	14.6191	14.6185	14.618
2	14.6446	14.637	14.6312	14.6269	14.6238	14.6217	14.6202	14.6191	14.6185	14.618
1	14.6446	14.637	14.6312	14.6269	14.6238	14.6217	14.6202	14.6191	14.6185	14.618

	31	32	33	34	35	36	37	38	39	40
3	14.6177	14.6176	14.6174	14.6174	14.6173	14.6173	14.6173	14.6173	14.6173	14.6173
2	14.6177	14.6176	14.6174	14.6174	14.6173	14.6173	14.6173	14.6173	14.6173	14.6173
1	14.6177	14.6176	14.6174	14.6174	14.6173	14.6173	14.6173	14.6173	14.6173	14.6173

	41	42	43	44	45	46	47	48	49	50
3	14.6173	14.6173	14.6173	14.6173	14.6173	14.6173	14.6173	14.6173	14.6173	14.6173
2	14.6173	14.6173	14.6173	14.6173	14.6173	14.6173	14.6173	14.6173	14.6173	14.6173
1	14.6173	14.6173	14.6173	14.6173	14.6173	14.6173	14.6173	14.6173	14.6173	14.6173